

Study of the Intervening Thin Liquid Film between Deformable Oil Drop/Bubble and a Solid Surface in Oil Production

by

Tianzi Bai

A thesis submitted in partial fulfillment of the requirements for the degree of

Doctor of Philosophy
in
Chemical Engineering

Department of Chemical and Materials Engineering
University of Alberta

© Tianzi Bai, 2022

Abstract

Interactions involving deformable bubbles/oil droplets play a critical role in many industrial applications. Understanding the dynamic thin film drainage process and interaction forces involving deformable bubbles/oil droplets and solid surfaces in the oil sands extraction process is of great importance fundamentally and practically. However, due to the complexity of bitumen, dynamic interactions involving bitumen are not fully understood. In this study, the bubble probe atomic force apparatus (AFM) technique and the dynamic force apparatus (DFA) were applied to study the interaction forces and film drainage process respectively, including bubble-bitumen interaction and bitumen-solid interaction. A theoretical model was developed to describe the interaction forces and also the film drainage process under different water chemistries. In addition, the mechanism of chemicals modifying the bitumen/water interfaces was also investigated.

The effect of a novel secondary processing aid, sodium citrate (Na_3Cit), on bitumen aeration was investigated. The bubble probe AFM technique was applied for direct measurement of the interaction between an air bubble and a bitumen coated silica wafer. It has been found that the pure Na_3Cit solution could prevent bubble-bitumen attachment due to the strongly more negatively charged bitumen/water and air/water interfaces. However, in the presence of Ca^{2+} , the addition of Na_3Cit would not prevent bubble-bitumen attachment when the solution ionic strength is high enough. The Stokes-Reynolds-Young-Laplace model was successfully implemented, predicting the interaction forces under all conditions. It proved that the competition between the electrostatic double layer (EDL) repulsion and the hydrophobic (HB) attraction was the main

reason that controlled the bubble-bitumen attachment. A stability map was established to reveal the attachment between bubble and bitumen in different water chemistries to guide the industrial applications.

An investigation was conducted to reveal the mechanism of how Na_3Cit modifies the bitumen/water interface and affects the zeta potential. The results showed that the chemicals that could form complexes or precipitates with metal cations, including Na_3Cit , EDTA, and Na_2HPO_4 , could lead to a more negatively charged bitumen surface compared with NaCl at pH 8.5. Through analyzing the metal content in the aqueous phase, we proved that ligands promoted the release of metal ions from bitumen, which recovered the negative charges of natural surfactants. Meanwhile, the ligands were capable of adsorbing on bitumen surfaces through outer-sphere and inner-sphere complexation, thus making the bitumen/water interface more negatively charged.

The DFA was applied to study the effect of viscosity on the dynamic film drainage process of: (1) silicone oil interaction with a hydrophilic mica surface and (2) bitumen drop interaction with a hydrophobic silica surface. In system (1), we illustrated that the competition between the viscous normal stress and the Laplace pressure controlled the film drainage process between a very viscous oil drop and a mica surface. The initial height of dimple formation was well captured by a derived analytical formula, $h_d = 0.5R\sqrt{Ca_f/(1 + 2Ca_d)}$, which holds for a wide range of drop capillary numbers. It has been proved that the viscous effect needs to be taken into consideration when $Ca_d > 0.1$ (Ca_d , drop capillary number). By applying this formula in system (2), the effect of solvent addition, approach velocity, and temperature on the film drainage process between a bitumen with high viscosity and a hydrophobic silica surface were studied. The results proved that the solvent addition and temperature did not affect the initial stage of dimple formation, and the viscosity was the dominant controlling factor. The formula could also predict the initial height of

dimple formation in this complicated bitumen system with a hydrophobic surface. In addition, the attachment time of bitumen onto the hydrophobic surface was found to be affected by approaching velocity, interfacial tension, and bitumen viscosity.

By applying the two techniques, a systematic study on the dynamic interaction between various components involved in the oil sands extraction process was performed. The effect of the water chemistry, oil viscosity, approach velocity, and surface hydrophobicity on the drainage dynamics of thin liquid films and surface forces provided fundamental insights into the interaction mechanisms of air bubble/oil drops and solid surfaces. It also provided fundamental understanding for the industrial processes (such as oil sands extraction process, 3D-printing, wastewater treatment and so on) in which oil drops with high viscosity are involved.

Preface

This thesis is composed of several published and submitted papers, as well as an article in preparation. Below is the statement of contributions to these co-authored papers that are presented in this thesis.

1. Chapter 1 and 2 are original work from Tianzi
2. Chapter 3 presents a published work: Tianzi Bai, James S. Grundy, Rogerio Manica, Mingda Li and Qingxia Liu. “Controlling the Interaction Forces between an Air bubble and Oil with Divalent Cations and Sodium Citrate.” *The Journal of Physical Chemistry C*, 124, 17622-17631 (2020). Tianzi Bai performed all the experiments, data analysis and wrote the entire paper. James S. Grundy help with the manuscript editing. Rogerio Manica helped with the modeling section. Mingda Li were involved with the experimental design on the measurement of bubble zeta potential. Qingxia Liu supervised the work.
3. Chapter 4 presents a paper in submission: Tianzi Bai, Bailin Xiang, Mingda Li, Rogerio Manica and Qingxia Liu. “Role of Sodium Citrate on the Zeta Potential of Bitumen: Interactions between Bitumen Metal Content and Ligands.” Submitted to *Colloids and Surface A: Physicochemical and Engineering Aspects*. Tianzi Bai and Bailin Xiang contributed equally to this work. Tianzi Bai and Bailin Xiang performed the experiments, data analysis and wrote the paper together. Mingda Li and Rogerio Manica helped with the manuscript editing. Qingxia Liu supervised the work.
4. Chapter 5 presents a published work: Tianzi Bai, Rogerio Manica, Bo Liu, Evert Klaseboer, Zhenghe Xu and Qingxia Liu. “Water Film Drainage between a Very Viscous Oil Drop and a Mica Surface.” *Physical Review Letters*, 127, 124503 (2021). Tianzi Bai performed all the experiments, data analysis and wrote the entire paper. Rogerio Manica helped with

the modeling part and editing the manuscript. Bo Liu was involved in the concept development and experimental design. Evert Klaseboer helped with the manuscript edition. Zhenghe Xu helped with the experimental design and manuscript proofreading. Qingxia Liu supervised the work.

5. Chapter 6 presents published work: Tianzi Bai, Rogerio Manica and Qingxia Liu. “Effect of Viscosity on the Thin Film Drainage between Bitumen and a Hydrophobic Silica Wafer.” *Energy and Fuels*. Tianzi Bai performed all the experiments, data analysis and wrote the entire paper. Rogerio Manica helped with the modeling part and the manuscript edition. Qingxia Liu supervised this work.

Acknowledgements

- First and foremost, I would like to express my great appreciation to my supervisor, Professor Qingxia Liu, for his instruction, entire support, and continuous encouragement through each stage of my Ph.D study.
- I would like to thank Dr. Rogerio Manica, for the suggestions and guidance for all of my work.
- I express my thanks to Professor Zhenghe Xu for allowing me to use all the instruments in his lab.
- The comments from Dr. Evert Klaesboer are greatly appreciated.
- I thank Dr. James S. Grundy, Dr. Bailin Xiang, and Dr. Bo Liu for their valuable comments and advice for my entire study.
- I really appreciate Ms. Laurie Kachmaryk, Mr. James Skwarok, Ms. Jiu Ru, and Mr. Les Dean, for their technical assistance.
- Special thanks to my colleagues and friends: Zhiqing Zhang, Jingxiao Li, Zhixiang Chen, Chao Qi, Mingda Li, Wei Guo, Hanrui Zheng, and Xu Zhang. It is grateful to have them in my Ph.D program, for their company and encouragement.
- Financial support from Syncrude and NSERC are very much appreciated.
- Finally, thanks to my family and my boyfriend Mr. Jia Meng. When I was faced difficulties and challenges, become frustrated, they encouraged me and supported me, letting me continue on this journey without fear.

Table of Contents

Abstract.....	ii
Preface.....	v
Acknowledgements.....	vii
Table of Contents.....	viii
List of Tables	xiv
List of Figures.....	xv
Chapter 1 Introduction.....	1
1.1 Background and motivation	2
1.2 Objective and scope of this thesis	4
1.3 Structure of this thesis	5
Chapter 2 Literature Review.....	8
2.1 Oil sands extraction process.....	9
2.2 Experimental Methods	12
2.2.1 Atomic force microscope.....	12
2.2.2 Thin film interferometry method	15
2.3 Stokes-Reynolds-Young-Laplace model.....	18
2.3.1 Lubrication theory.....	19
2.3.2 Young-Laplace equation.....	21

2.3.3	Disjoining pressure	22
2.3.4	Initial and boundary conditions	24
2.4	Remaining questions	25
2.4.1	A novel secondary processing aid.....	26
2.4.2	Viscosity and interfacial elasticity of bitumen.....	27
2.4.3	Hydrophobic interaction	29
2.4.4	Pressure difference between deformable drop and surrounding solution.....	31
Chapter 3 Controlling the Interaction Forces between an Air Bubble and Oil with Divalent Cations and Sodium Citrate		
	Abstract	32
	Abstract	33
3.1	Introduction	34
3.2	Experimental section	35
3.2.1	Materials	35
3.2.2	Preparation of the bitumen surface	36
3.2.3	Zeta potential measurement	37
3.2.4	Force measurement	38
3.3	Result and discussion	40
3.3.1	Bitumen zeta potential	40
3.3.2	Bubble-bitumen interaction in pure electrolyte solutions at pH 8.5	43
3.3.3	Stability map	52

3.4	Conclusions	54
Chapter 4 Role of Sodium Citrate on the Zeta Potential of Bitumen: Interactions between		
Bitumen Metal Content and Ligands		
	Abstract	56
4.1	Introduction	57
4.2	Materials and methods	58
4.2.1	Materials	60
4.2.2	Zeta potential measurement and metal content released from bitumen.....	62
4.2.3	Adsorption measurements by QCM-D	63
4.2.4	ATR-FTIR analysis for chemicals adsorption	64
4.3	Results	65
4.3.1	Zeta potential of bitumen droplet in the presence of different sodium salts at pH 8.5	65
4.3.2	Metal content released from bitumen	66
4.3.3	QCM-D analysis of adsorption on bitumen surfaces	71
4.3.4	ATR-FTIR analysis for chemicals adsorption	74
4.4	Discussion	80
4.5	Conclusion.....	83
Chapter 5 Water Film Drainage between a Very Viscous Oil Drop and a Mica Surface		
	Abstract	84
	Abstract	85

5.1	Introduction	86
5.2	Experimental section	87
5.3	Results and discussion.....	89
5.4	Conclusion.....	97
Chapter 6 Effect of Viscosity on the Thin Film Drainage between Bitumen and a		
Hydrophobic Silica Wafer		
	Abstract	98
	Abstract	99
6.1	Introduction	100
6.2	Experimental section	102
6.2.1	Materials and Methods.....	102
6.2.2	Instrument setup.....	102
6.3	Results	104
6.3.1	Solvent diluted bitumen	105
6.3.2	Bitumen at different temperature	111
6.4	Discussion	114
6.4.1	The moment of dimple formation.....	114
6.4.2	Attachment time.....	116
6.5	Conclusion.....	119
Chapter 7 Conclusion and Future work.....		
7.1	Conclusion.....	121
		122

7.2 Future research	124
References	125
Appendix A.....	146
Comparison between constant potential and constant charge models	146
Charge at the Stern plane per unit area of bitumen droplet	146
Air/water interfacial tension and bitumen surface contact angle	147
Reproducibility of force curves	149
Comparison between theoretically-fitted Stern potential and measured zeta potential values of the air bubble in different electrolyte solutions	150
Contributions of different surface forces in NaCl solution.....	153
Contributions of different surface forces in CaCl ₂ solution.....	154
Adding citrate after adsorption of Ca ²⁺ to the bitumen surface	154
References	156
Appendix B.....	157
Concentration of metal ions released from bitumen.....	157
ATR-FTIR.....	158
Appendix C	161
The height of dimple formation	161
Drive function	164
Dimple height.....	164

Film drainage process of selected conditions	165
Properties of oils used in the manuscript	166
Derivation of the modified SRYL model.....	167
Stokes-Reynolds-Young-Laplace (SRYL) model	167
Model for high viscosity drop.....	169
Modified SRYL model	170
Characteristic scales.....	171
Scaling of hd	172
Comparison between theoretical and experimental film drainage process between high- viscosity oil and a mica surface	173
References.....	175
Appendix D.....	177
Film drainage process of bitumen at high temperature at $V=0.1$ mm/s.....	177

List of Tables

Table 4-1 Details of chemicals used in our experiments	61
Table 4-2 Solution pH of the extracted aqueous solution after making bitumen emulsion in different electrolyte solutions at pH 8.5 and 10.5.....	69
Table 4-3 Calculated mass deposition on bitumen surfaces pH 8.5.	74
Table 6-1 Physical properties of different solvent diluted bitumen.....	105
Table 6-2 Physical properties of bitumen at different temperature	112
Table A1 Measured and fitted zeta potentials of the bubble. Theoretical values within the specified range provided results that were in agreement with the experiment.....	152
Table A2 Concentration of metal ions released from bitumen	157
Table A3 Assignments of vibration bands of bitumen from ATR-FTIR	159
Table A4 Assignments of vibration bands of EDTA solution at pH 8.5 from ATR-FTIR	160
Table A5 Physical properties of different oils.	167

List of Figures

Figure 2-1 Schematic of water-based bitumen extraction process from oil sands (replotted from Masliyah et al.).³ 12

Figure 2-2 (a) Schematic figure of the experiment for measuring interaction forces between a silica particle and a surface air bubble.²⁴ (b) Optical microscopy image of a cantilever with an attached air bubble interacting with another surface air bubble.²⁸ (c) Schematic diagram of bubble probe AFM technique for measuring interaction forces between an air bubble and a bitumen surface.^{20,21} 15

Figure 2-3 (a) Schematic for the “Scheludko” cell.³⁷ (b) Schematic diagram for the dynamic force apparatus.⁴⁰ (c) A snapshot for the observed fringes. 18

Figure 2-4 (a) Schematic illustration for air bubble/oil drop interacting with a solid surface and definition of parameters. (b) Enlargement of gray circle and definition of coordinate. (c) Schematic illustration for immobile-immobile boundary conditions. 19

Figure 3-1 Schematic diagram of the AFM experimental setup. A bubble is anchored to an AFM tip that is driven toward the bitumen surface. θ is the water contact angle of the circular gold patch on the cantilever. The interaction force is extracted by the deflection of the cantilever as a function of displacement, which is the change of $X(t)$ over time. 40

Figure 3-2 Zeta potential of bitumen droplets at pH 8.5 in (A) pure electrolyte solution with different concentration and (B) 4 mM CaCl_2 with different concentrations of Na_3Cit . The solid lines between dots are a guide to the eye. 43

Figure 3-3 (A) Comparison of experimental interaction force and theoretical calculation between the air bubble and bitumen surface in 5 mM Na_3Cit . Blue circles represent experimental data while the red line represents the theoretical calculation. (B) Calculated disjoining pressure

contribution in 5 mM Na₃Cit. The force measurements were conducted at pH = 8.5, and the bubble approach velocity was $V = 1 \mu\text{m/s}$. The bubble radius was $R = 80 \mu\text{m}$ 45

Figure 3-4 Interaction force between air bubble and bitumen surface versus time in (A) 10 mM NaCl and (B) 15 mM NaCl. Blue circles represent experimental data while the red lines represent the theoretical calculation. (C) Calculated disjoining pressures in 10 mM NaCl and 15 mM NaCl. The force measurement was conducted at pH = 8.5, and the bubble approach velocity was $V = 1 \mu\text{m/s}$. Experimental values used for SRYL fitting were $\gamma = 72.8 \text{ mN/m}$ for air/water interfacial tension and bubble radii of $R = 84 \mu\text{m}$ for 10 mM NaCl and $R = 85 \mu\text{m}$ for 15 mM NaCl. 48

Figure 3-5 Comparison of experimental interaction force and theoretical calculation between the air bubble and bitumen surface in (A) 3 mM CaCl₂ and (B) 4 mM CaCl₂. Blue circles represent experimental data while the red lines represent the theoretical calculation. (C) Calculated disjoining pressure in 3 and 4 mM CaCl₂. The force measurements were conducted at pH = 8.5, and the bubble approach velocity was $V = 1 \mu\text{m/s}$. The bubble radii were $R = 81 \mu\text{m}$ for 3 mM CaCl₂ and $R = 84 \mu\text{m}$ for 4 mM CaCl₂. 48

Figure 3-6 Comparison of experimental interaction force and theoretical calculation between the air bubble and bitumen surface in (A) 4 mM CaCl₂ + 0.17 mM Na₃Cit, (B) 4 mM CaCl₂ + 2.3 mM Na₃Cit, and (C) 4 mM CaCl₂ + 4 mM Na₃Cit. Blue circles represent experimental data while the red lines represent the theoretical calculation. 51

Figure 3-7(A) Calculated EDL pressure contribution to the overall disjoining pressure of one pure solution and three mixtures: 4 mM CaCl₂ + 0 mM Na₃Cit, 4 mM CaCl₂ + 0.17 mM Na₃Cit, 4 mM CaCl₂ + 2.3 mM Na₃Cit, and 4 mM CaCl₂ + 4 mM Na₃Cit. Inset: Zoom in of the red square. The axis labels of the inset are the same as that of (A). (B) Calculated overall disjoining pressure of the one pure solution and three mixtures: 4 mM CaCl₂ + 0 mM Na₃Cit, 4 mM CaCl₂

+ 0.17 mM Na₃Cit, 4 mM CaCl₂ + 2.3 mM Na₃Cit, and 4 mM CaCl₂ + 4 mM Na₃Cit. The legend in (A) is the same as that in (B). The bubble radii of the pure solution and the three mixtures were R = 84 μm for 0 mM Na₃Cit, R = 85 μm for 0.17 mM Na₃Cit, R = 78 μm for 2.3 mM Na₃Cit, and R = 81 μm for 4 mM Na₃Cit. 52

Figure 3-8 Stability map of the interaction between the air bubble and bitumen surface. All the experiments were conducted at pH 8.5. The shaded area separating the attachment and nonattachment regions was calculated using the SRYL model within experimental error. 54

Figure 4-1 Illustration of experimental procedures: (a) zeta potential of bitumen droplets, (b) metal content released from the bitumen. 63

Figure 4-2 Bitumen zeta potential as a function of different salts concentration at pH 8.5. 66

Figure 4-3 Concentration of metal ions released from bitumen to the aqueous solution in the presence of different salts at pH 8.5: (a) Ca, (b) Mg, (c) Al, (d) Mn, (e) Cu, (f) V. 70

Figure 4-4 Concentration of metal ions released from bitumen to the aqueous solution in the presence of different salts at pH 10.5: (a) Ca, (b) Mg, (c) Al, (d) Mn, (e) Cu, (f) V. 71

Figure 4-5 Change in frequency (Δf) and dissipation (ΔD) at 3, 5 and 7 overtones of the bitumen coated sensor under (a) 25 mM NaCl, (b) 25 mM Na₃Cit, (c) 25 mM EDTA, (d) 25 mM Na₂HPO₄ at pH 8.5. 72

Figure 4-6 ATR-FTIR spectra of: (a) Na₃Cit solution at pH 8.5, (b) normalized bitumen immersed in 100 mM Na₃Cit solution at pH 8.5 and (c) normalized bitumen immersed in 100 mM Na₃Cit solution at pH 8.5 and rinsed with Milli-Q water. 76

Figure 4-7 ATR-FTIR spectra of: (a) EDTA solution at pH 8.5, (b) normalized bitumen immersed in 100 mM EDTA solution at pH 8.5 and (c) normalized bitumen immersed in 100 mM EDTA solution at pH 8.5 and rinsed with Milli-Q water. 77

Figure 4-8 ATR-FTIR spectra of: (a) Phosphate solution at pH 8.5, (b) normalized bitumen immersed in 100 mM phosphate solution at pH 8.5 and (c) normalized bitumen immersed in 100 mM phosphate solution at pH 8.5 and rinsed with Milli-Q water. 79

Figure 4-9 Mechanisms of complexants modifying the zeta potential of bitumen surfaces. 80

Figure 5-1 (a) Schematic of the dynamic force apparatus. An oil drop with radius $R = 1.05 \pm 0.01$ mm was generated at the end of a capillary. The drop was driven toward the hydrophilic mica surface by a motor. (b) Thin film region corresponding to the red square in (a). (c) A snapshot of the interference fringes (green channel) obtained between an oil drop and a mica surface ($\mu_0 = 25.8 \text{ Pa} \cdot \text{s}$, $V = 1.06 \text{ mm/s}$) in 0.1 mM SDS solution. (d) Axisymmetric film thickness profile obtained from (c). 88

Figure 5-2 (a) Comparison between the experimental results (points) and the theoretical model (lines) for the film evolution of an oil drop of 0.001 Pa·s viscosity interacting with a mica surface in 0.1 mM SDS aqueous solution at the approach velocity of 1.06 mm/s ($Ca_d = 10^{-5}$). The measured times of the profiles from top to bottom are -0.015, 0.018, 0.085, 0.218, 0.55, 2.12,. 90

Figure 5-3 (a) Film thickness at the center $h(0,t)$ as a function of time for oil drops of different viscosity in 0.1 mM SDS solution at an approach velocity of 1.06 mm/s. (b) Selected drop shape profiles of an oil drop of 37.0 Pa·s viscosity from Fig. 2(b) in 0.1 mM SDS aqueous solution at the approach velocity of 1.06 mm/s at times 0.067, 0.618, and 19.7 s. 91

Figure 5-4 Height of initial dimple formation for oil drops or bubbles interacting with a hydrophilic solid surface in water, as a function of Ca_d as compared with the theoretical curve of Eq. (5-8) (line). The five different cases are (a) $V = 1.06 \text{ mm/s}$ in 0.1 mM SDS solution, $\mu_0 = 0.001 - 111.5 \text{ Pa} \cdot \text{s}$; (b) $V = 0.1 \text{ mm/s}$ in 0.1 mM SDS solution, $\mu_0 = 0.001 - 111.5 \text{ Pa} \cdot \text{s}$; (c) $V = 1.06 \text{ mm/s}$ in 1 mM SDS solution, $\mu_0 = 0.001 - 111.5 \text{ Pa} \cdot \text{s}$; (d) $\mu_0 = 111.5 \text{ Pa} \cdot \text{s}$ in 0.1

mM SDS solution, $V = 0.1 - 10$ mm/s; (e) bubble interacting with silica in water. The data of the dimple height for bubble interacting with hydrophilic silica surface in water (e) is from Ref. 16. The result of the theoretical calculation fit well with the results from corresponding experiments. The transition occurred at Ca_d around 0.1. Inset: the height of initial dimple

formation as a function of oil viscosity (same legend). 96

Figure 6-1 (a) Schematic of the dynamic force apparatus. A bitumen drop with radius $R = \dots$ 103

Figure 6-2 Film drainage process between toluene diluted bitumen drop and a hydrophobic silica

wafer in 10 mM NaCl solution at $V = 1$ mm/s (a-c) and $V = 0.1$ mm/s (d-f). (a) Comparison

between theoretical model (lines) and experimental results (points) of film thickness for 50 wt%

bitumen in toluene. The measured time from top to bottom are 0, 0.01, 0.04, 0.07, 0.16, 0.22,

0.32, 0.65, 1.36, 2.70, 5.89, 17.46 s. (b) 90 wt% bitumen in toluene at 0, 0.02, 0.34, 4.77, 13.52,

30.48, 54.31 s. (c) 93 wt% bitumen in toluene at 0, 0.01, 0.04, 0.31, 8.97s. (d) Comparison

between theoretical model (lines) and experimental results (points) of film thickness for 50 wt%

bitumen in toluene. The measured time from top to bottom are 0, 0.06, 0.27, 0.69, 1.24, 6.74 s.

(e) 90 wt% bitumen in toluene at 0, 0.07, 0.17, 1.02, 2.59, 13.91 s. (f) 93 wt% bitumen in toluene

at 0, 1.06, 1.34, 2.54, 26.4 s. 106

Figure 6-3 Film drainage process between decane diluted bitumen drop and a hydrophobic silica

wafer in 10 mM NaCl solution at $V = 1$ mm/s (a, b) and $V = 0.1$ mm/s (c, d). (a) 90 wt% bitumen

in decane. The measured time from top to bottom are: 0, 0.03, 0.31, 13.26, 38.05 s. (b) 93 wt%

bitumen in decane at 0, 0.01, 5.55, 148.43 s. (c) 90 wt% bitumen in decane at 0, 0.05, 0.50, 1.60,

3.90 s. (d) 93 wt% bitumen in decane at 0, 0.14, 2.16, 16.22 s. 111

Figure 6-4 Film drainage process between bitumen drop and a hydrophobic silica wafer in 113

Figure 6-5 Comparison between the scaled experimental dimple height and the theoretical calculation using Eq. (6-1). The theoretical calculation agrees with the experimental data very well..... 114

Figure 6-6 (a) Attachment time between different concentration of bitumen in toluene and a hydrophobic silica wafer at different approach velocities. (b) Film thickness at the center $h(0, t)$ and at the barrier rim $h(r_{rim}, t)$: symbols for experimental results, solids lines for corresponding theoretical predictions and dashed lines for guiding eyes (filled symbols for $h(0, t)$ and opened symbols for $h(r_{rim}, t)$). 116

Figure 6-7 (a) Attachment time between bitumen with different viscosity and hydrophobic silica wafer at different approach velocities. (b) Snapshot of a stable water film formed by bitumen at 40 °C and a hydrophobic silica wafer after 10 min aging at $V = 1$ mm/s within the maximum shooting time (10 min). (c) Snapshot of water film in which local attachment happens for bitumen at 40 °C. The red square represents the place where local attachment happens. 117

Figure A1 Comparison between the numerical solutions of the nonlinear Poisson-Boltzmann equations under constant potential and constant charge boundary conditions. 146

Figure A2 Charge at the Stern plane per unit area of bitumen droplets at pH 8.5 in (A) pure electrolyte solution with different concentration and (B) 4 mM CaCl_2 with different concentrations of Na_3Cit . The lines between dots are a guide to the eye. 147

Figure A3 Air/water interfacial tension as a function of time in the presence of bitumen surface. 148

Figure A4 Water contact angle on bitumen surface as a function of time..... 149

Figure A5 Interaction force between one air bubble and different positions on the bitumen surface over 30 min in 5 mM Na ₃ Cit at pH 8.5.	150
Figure A6 Schematic diagram of experimental set up of generating nanobubble suspension. ..	151
Figure A7 Contributions of disjoining pressure in (A) 10 mM NaCl and (B) 15 mM NaCl.....	153
Figure A8 Contributions of disjoining pressures in (A) 3 mM CaCl ₂ and (B) 4 mM CaCl ₂	154
Figure A9 Interaction between air bubble and bitumen surface after initial equilibration in 4 mM CaCl ₂ solution followed by the addition of 2.3 mM Na ₃ Cit.	155
Figure A10 ATR-FTIR spectra of bitumen.	158
Figure A11 (a) Snapshots of the interference fringes of green channel in a time sequence obtained between an oil drop and a mica surface. ($\mu_0 = 68.2 \text{ Pa}\cdot\text{s}$, $V = 1.06 \text{ mm/s}$, 0.1 mM SDS, frame rate 5000 fps) (b) Evolution of the light intensity at the film center in (a). (c) Film thickness as a function of time between the oil drop and the mica surface transferred from (b). The dimple height of this condition was obtained by taking an average of the film thickness in the shaded area.	163
Figure A12 Displacement controlled by the motorized actuator and the real-time velocity of the oil droplet approaching the mica surface with the approach velocity of 1.06 mm/s.	164
Figure A13 Film thickness at the center $h(0,t)$ as a function of time of oil drops with different viscosity for: (a) $V = 0.1 \text{ mm/s}$ in 0.1 mM SDS solution; (b) $V = 1.06 \text{ mm/s}$ in 1 mM SDS solution.....	165
Figure A14 Comparison between theoretical (lines) and experimental (dots) film drainage process between oil with a viscosity of 0.001 Pa·s and a mica surface in: (a) $V = 0.1 \text{ mm/s}$ in 0.1 mM SDS solution. The measured time of profiles from top to bottom is -0.025, 0.025, 0.125, 1.025, 46.692, 88.275, 124.809, and 171.042 s. (b) $V = 1.06 \text{ mm/s}$ in 1 mM SDS solution. The	

measured time of profiles from top to bottom is $-0.035, -0.001, 0.066, 0.182, 0.466, 1.866,$
 $7.316, 15.826, 45.332, 81.649, 266.349,$ and 581.649 s. 165

Figure A15 Film drainage process between oil drops with different viscosity and a solid surface
in 0.1 mM SDS solution at $V = 1.06$ mm/s. (a) $\mu_0 = 10.6$ Pa \cdot s. The measured time of the
profiles from top to bottom is: $0.020, 0.136, 1.420, 6.253, 33.836, 81.753, 161.536, 242.720,$ and
 321.453 s. (b) $\mu_0 = 111.5$ Pa \cdot s. The measured time of the profiles from top to bottom is: $0.019,$
 $0.069, 0.352, 2.102, 13.852, 81.769, 126.119, 177.802,$ and 235.469 s. 166

Figure A16 Comparison between theoretical (lines) and experimental (dots) film drainage
process between oil with different viscosity in 0.1 mM SDS solution at $V = 1.06$ mm/s. (a) $\mu_0 =$
 37.0 Pa \cdot s. The measured time of the profiles from top to bottom is: $0.067, 0.618, 19.7, 97.1,$
 $144.5, 211.0, 318.1,$ and 391.6 s. Drop stopped moving at 0.26 s. (b) $\mu_0 = 68.2$ Pa \cdot s. The
measured time of the profiles from top to bottom is: $0.025, 0.743, 3.42, 62.69, 101.6, 137.0,$
 $189.0, 243.9$ s. Drop stopped moving at 0.072 s..... 174

Figure A17 Film drainage process between bitumen drop at high temperature and a hydrophobic
silica wafer in 10 mM NaCl solution at $V = 0.1$ mm/s. (a) 40 $^{\circ}$ C. The measured time from top to
bottom are: $0, 0.352, 2.44, 14.408$ s. (b) 45 $^{\circ}$ C. The measured time from top to bottom are: $0,$
 $0.28, 1.28, 12.664$ s. 177

Chapter 1 Introduction

1.1 Background and motivation

Canada is the fourth largest crude oil producer globally, and 96% of the proven crude oil reserves in Canada are in the oil sands. To recover bitumen from oil sands ores, the open-pit mining process followed by hot water extraction is widely used in the Canadian oil sands industry. Open-pit mining technology can be applied for shallow deposits, with an overburden height of less than 70 m. The mined oil sands are crushed and mixed with hot water and primary processing aid (usually caustic, NaOH) to form a slurry. The slurry is then fed into a hydrotransport slurry pipeline, where bitumen is liberated from sand and subsequent bitumen coalescence and aeration takes place. This slurry then enters a primary separation vessel and the aerated bitumen at the top of the primary separation vessel is collected as the bitumen froth that contains roughly 60 wt.% bitumen, 30 wt.% water and 10 wt.% solids. Un-aerated bitumen droplets that remain in the slurry are further collected by induced air flotation or tailing oil vessels. After that, the collected bitumen froth is deaerated and sent to the froth treatment unit.

In the hydrotransport stage, the traveling velocity of the aqueous solution can be as high as meters per second, the relative velocity between different components is within the range of millimeters per second. The interaction between deformable droplets or bubbles and solid surfaces in aqueous solutions is of great importance in order to improve the oil sands extraction process. The dynamic drainage of the thin liquid film between an air bubble/oil drop and a solid surface is usually the main physical step that controls the attachment efficiency. When air bubble/oil drop approaches another air bubble/oil drop or solid surface, the film drainage process can be generalized into three stages. First, the air bubble/oil droplet approaches the solid surface under external forces (for example, buoyance force) and the air bubble/oil droplet remains spherical at this stage. As the air bubble/oil drop keeps approaching the solid surface, the air bubble/oil drop

starts to deform and form a dimple when the hydrodynamic pressure in the liquid film is comparable to the pressure inside the air bubble/oil drop. As the liquid drains out, the final stability of the liquid film is determined by the disjoining pressure considering surface forces, including van der Waals (vdW), electrostatic double layer (EDL), hydrophobic (HB) forces, and so on.

In the past decades, two groups of techniques had been applied to study the interaction between air bubbles/oil drops and solid surfaces. The first group directly measures the interaction force between an air bubbles/oil drop and a solid surface. By applying the bubble/drop probe atomic force apparatus (AFM), the interaction force between the deformable bubble/drop and solid surface can be obtained as a function of distance under static conditions. The second group of technique concerned both the film geometry and the interaction force. By applying the recently developed dynamic force apparatus (DFA), the spatiotemporal film thickness and the time dependent interaction force between an air bubble/oil drop and a solid surface under hydrodynamic conditions can be investigated.

In clean systems, the interaction forces and bubble/droplet geometric deformations, being investigated for decades, can be well captured by the Stokes-Reynolds-Young-Laplace model. However, the system involving bitumen and different chemical aids in the aqueous solution applied in the industry (including cations, primary and secondary processing aids) are more complicated compared with clean systems. For example, bitumen is a high viscosity heavy oil and the majority of the studies barely focus on the effect of viscosity on the dynamic film drainage. In addition, the surface property at the bitumen/water interface varies a lot at different positions of the interface. The electrolyte in the aqueous phase could possibly have some reaction with the components in bitumen, thus modifying the properties at the bitumen/water interface and influencing the interaction forces. The chemical aids additive to the oil sands extraction process

would also have a great effect on the properties of interfaces, whose effects on the dynamic interactions between various components remain unclear. Therefore, a complete understanding of the dynamic film drainage process and also the surface forces involving bitumen or modeled oil drop which has similar properties to bitumen in different aqueous solutions is of great importance to provide guidance for the industry.

1.2 Objective and scope of this thesis

The objective of this thesis is to fully understand the dynamic interaction between solid surface and air bubble/oil drop in complicated water chemistry and provide valuable insights from the fundamental perspective in the oil sands extraction process.

In Chapter 3, the effect of a novel secondary processing aid, sodium citrate, on the interaction force between an air bubble and a bitumen coated silica surface has been investigated using the AFM. Sodium citrate, recently applied in the oil sands extraction process, was found to significantly increase bitumen recovery and froth quality. The effect of pure electrolyte, including NaCl, CaCl₂, and Na₃Cit on the interaction between bubble and bitumen was investigated. Other than that, the combined effect of CaCl₂ and Na₃Cit was also studied, in order to simulate the industrial environment. The Stokes-Reynolds-Young-Laplace (SRYL) model was used to fit the experimental data. A stability map, indicating the attachment and non-attachment regions between bubble and bitumen, was also established to provide guidance for industrial application on the chemical conditions for bubble-bitumen attachment.

In Chapter 4, the possible reason for the modification of the electrical properties at the bitumen/water interface by sodium citrate was investigated. Four different electrolytes, including NaCl, Na₂SO₄, EDTA and Na₂HPO₄, were selected to be compared with sodium citrate. ICP-MS,

QCMD, and FTIR experiments were conducted to test the reaction between metal ions in bitumen and added ligands. The mechanism of how Na_3Cit and other selected ligands affect the surface charges of bitumen surfaces has been proved in this study.

In Chapter 5, the effect of the viscosity on the dynamic film drainage process between a very viscous silicone oil and a hydrophilic mica surface was investigated. By considering an extra pressure inside the oil drop, an analytical formula was developed which can successfully predict the height of dimple formation at a wide range of capillary numbers of the drop. In addition, our study clearly illustrated that the competition between the viscous normal stress and the Laplace pressure controlled the whole film drainage process.

In Chapter 6, the dynamic film drainage process between a bitumen drop with different viscosity and a hydrophobic silica surface was studied and the previous developed model was used to provide a theoretical explanation of experimental phenomenon in this complex system. The complexity of the bitumen composition, solvent addition, temperature, and the aging effect did not affect the prediction of the height of the first dimple occurrence, but had a great influence on the attachment time between bitumen and hydrophobic silica surface.

1.3 Structure of this thesis

This thesis includes 7 Chapters. Chapter 3, 5 and 6 are published papers, Chapter 4 is a submitted paper. The content of each chapter is summarized below:

Chapter 1 provides a brief introduction of the background information and motivation, objective and scope, and the structure of this thesis.

Chapter 2 is a detailed literature review of the oil sands extraction process, the experimental methods applied in the investigation of dynamic film drainage and surface force measurement, and the Stokes-Reynolds-Young-Laplace model. The main remaining questions in this project are also discussed.

Chapter 3 studies the interaction forces between an air bubble and a bitumen surface. The effect of the secondary processing aid, sodium citrate, and its combined effect with CaCl_2 on the interaction forces has been investigated. The mechanisms on sodium citrate and cations manipulating the attachment between bubble and bitumen are well explained. This chapter has been published:

Tianzi Bai, James S. Grundy, Rogerio Manica, Mingda Li and Qingxia Liu. “Controlling the Interaction Forces between an Air bubble and Oil with Divalent Cations and Sodium Citrate.” *The Journal of Physical Chemistry C*, 124, 17622-17631 (2020).

Chapter 4 discusses the possible reason of the ligands, including Na_3Cit , EDTA, and Na_2HPO_4 , on the modification of the electrical properties at the bitumen/water interface. The metal content released from bitumen to aqueous solution and the adsorption of chemical aids to bitumen/water interface were studied to support our assumption.

Tianzi Bai, Bailin Xiang, Mingda Li, Rogerio Manica and Qingxia Liu. “Role of Sodium Citrate on the Zeta Potential of Bitumen: Interactions between Bitumen Metal Content and Ligands.” Submitted to *Colloids and Surface A: Physicochemical and Engineering Aspects*.

Chapter 5 investigates the film drainage process between a very viscous oil drop and a mica surface. The oil viscosity ranging from 0.001-100 Pa·s was investigated. Considering an extra pressure inside the oil drop, viscous normal stress, a modified Stokes-Reynolds-Young-Laplace

model has been developed and an analytical formula was derived that can well predict the height of the first dimple occurrence under a wide range of drop capillary number (Ca_d). This chapter has been published:

Tianzi Bai, Rogerio Manica, Bo Liu, Evert Klaseboer, Zhenghe Xu and Qingxia Liu. “Water Film Drainage between a Very Viscous Oil Drop and a Mica Surface.” *Physical Review Letters*, 127, 124503 (2021).

Chapter 6 illustrates the impact of bitumen viscosity on the initial film drainage process and the attachment time between bitumen drop and a hydrophobic silica wafer. The effect of solvent addition, approach velocity, and temperature has been studied. It reveals that the viscosity is the dominate factor when the bitumen viscosity is much high than that of the surrounding solution. This chapter has been published:

Tianzi Bai, Rogerio Manica and Qingxia Liu. “Effect of Viscosity on the Thin Film Drainage between Bitumen and a Hydrophobic Silica Wafer.” *Energy and Fuels* (2022).

Chapter 7 summarizes the conclusions of this thesis and presents the possible future research plans.

Appendix contains additional figures and calculations for the thesis.

Chapter 2 Literature Review

2.1 Oil sands extraction process

The Clark hot water extraction process was patented by Clark in the 1920s, which is the first method applied in the commercial oil sands industry for bitumen extraction.¹ After decades of improvement, warm water is used nowadays to replace the hot water in order to save energy.² The schematic of the water-based bitumen extraction process is shown in Figure 2-1.³ Firstly, the oil sands are mined from the open-pit mine using shovels and trucks, then crushed for size reduction. The oil sands are mixed with process water with the addition of different processing aids (usually caustic, NaOH) to form a slurry, and the slurry is introduced into the hydrotransport pipeline, where the bitumen liberation and bitumen aeration take place. Bitumen liberation is the process of the recession and detachment of bitumen from the solid surface. Bitumen film would first start thinning and form pin-holes on the solid surface in the surrounding warm water. After that, the bitumen film ruptures, gradually forms droplets, and eventually detaches from the solid surface under hydrodynamic forces.⁴ Bitumen aeration is the process in which bitumen-air bubble aggregation or air bubble engulfment by bitumen followed by the recovery of the floated bitumen droplets from the slurry. The density of bitumen is almost the same as water, which causes the formation of a suspension of bitumen droplets in water solution without the bubble attachment or engulfment. Aeration reduces the apparent bitumen density and allows the aerated bitumen to float to the top of the slurry. The slurry temperature is varied from 35°C to 75°C. This slurry then enters into a primary separation vessel and the aerated bitumen at the top is collected to form the bitumen froth that contains roughly 60 wt.% bitumen, 30 wt.% water and 10 wt.% solids.³ Un-aerated bitumen droplets that remain in the slurry are further collected by induced air flotation or tailing oil vessels. After that, the collected bitumen froth is deaerated and sent to the froth treatment unit. Solvent addition, including naphtha and paraffin, can facilitate the removal of water and solids from

bitumen froth. Partial precipitation of asphaltene occurs when a paraffinic solvent is used at a high solvent to bitumen ratio. The formation of asphaltene aggregates can trap the water and solid which greatly enhances gravity separation.³ The tailings, which are at the bottom of the primary separation vessel are fed into the tailing pond for solid-liquid separation. The water from the tailings pond is recycled and reused in the bitumen extraction process.⁵ The recycled water usually contains different kinds of multivalent cations (e.g. calcium, magnesium, and ammonia), anions (e.g. bicarbonate and sulfate), and organic compounds including surfactant (e.g. naphthenic acid and humic acid) and non-surfactant (i.e. toluene, asphaltene, and benzene).⁶

Many studies have proved the important role of the interaction between air bubbles, bitumen drops, and solid particles on determining bitumen extraction efficiency and bitumen recovery.⁷⁻¹¹ In the bitumen liberation step, the most important interaction is between bitumen and sand. A stronger repulsive force facilitates the bitumen detachment from the silica surface, thus increasing the bitumen liberation efficiency.⁸ Numerous interactions are involved in the bitumen flotation step. The dynamic interaction between an air bubble and bitumen drop determines the chance of collision and attachment between them, directly affect the bitumen aeration efficiency, while the interactions between bubble and solid and/or bitumen and solid could also indirectly affect the bitumen froth quality. For example, the hydrophobic solid surface could attach to the air bubbles and bitumen drops, thus increasing the solid content in the bitumen product.^{12,13} In addition, the coalescence between two bitumen droplets is desirable in bitumen flotation due to the larger bitumen drop size facilitating bubble attachment to the bitumen surface.^{3,11,14}

When the deformable air bubble/bitumen drop approaches another air bubble/bitumen drop or solid surface, the air bubble/bitumen drop will become flat when at low approach velocity or reverse the surface curvature (which is called “dimple formation”) at a higher approach velocity.

This can be explained by the hydrodynamic pressure and/or the disjoining pressure counterbalance or be higher than the pressure inside the air bubble/oil drop.¹⁵ The height at the first dimple occurrence is highly dependent on the approaching velocity, air bubble/bitumen drop size, and interfacial tension. It has been found that a higher approach velocity, bigger droplets size and a smaller interfacial tension would lead to a higher dimple height, which would possibly result in a longer film lifetime.¹⁶⁻¹⁸ After the first dimple occurrence, the film thickness at the center point remains the same, while the film thickness at the barrier rim keeps decreasing, resulting in a more and more pronounced dimple. A bigger dimple would trap a larger amount of liquid and also the impurities in the liquid film, which could significantly decrease the bitumen froth quality. As the water drains out, the thickness of the center point further decreases. The film drainage rate and the final state of the liquid film (a stable or ruptured film and the thickness of the final film), are determined by the surface forces.¹⁹ The typical surface forces that need to be taken into consideration are van der Waals (vdW), electrical double layer (EDL), and hydrophobic (HB) forces. At the industrial operation pH range, the zeta potentials of air bubbles, solid surfaces, and bitumen drops are negative, leading to a repulsive EDL force.²⁰⁻²² If the solid is hydrophilic, the strong repulsive EDL interaction would lead to a stable water film, prevents the attachment and/or coagulation between different components. If the solid is hydrophobic, the attractive hydrophobic force would induce the film to rupture at a critical thickness. The whole dynamic thin film drainage process, including the first dimple occurrence, the following film drainage process, and the formation of the final state of the film, determines the oil sands extraction efficiency. Therefore, a comprehensive understanding of the interactions between different components in the oil sands extraction process, especially under the dynamic conditions and the industrial-like conditions, is essential.

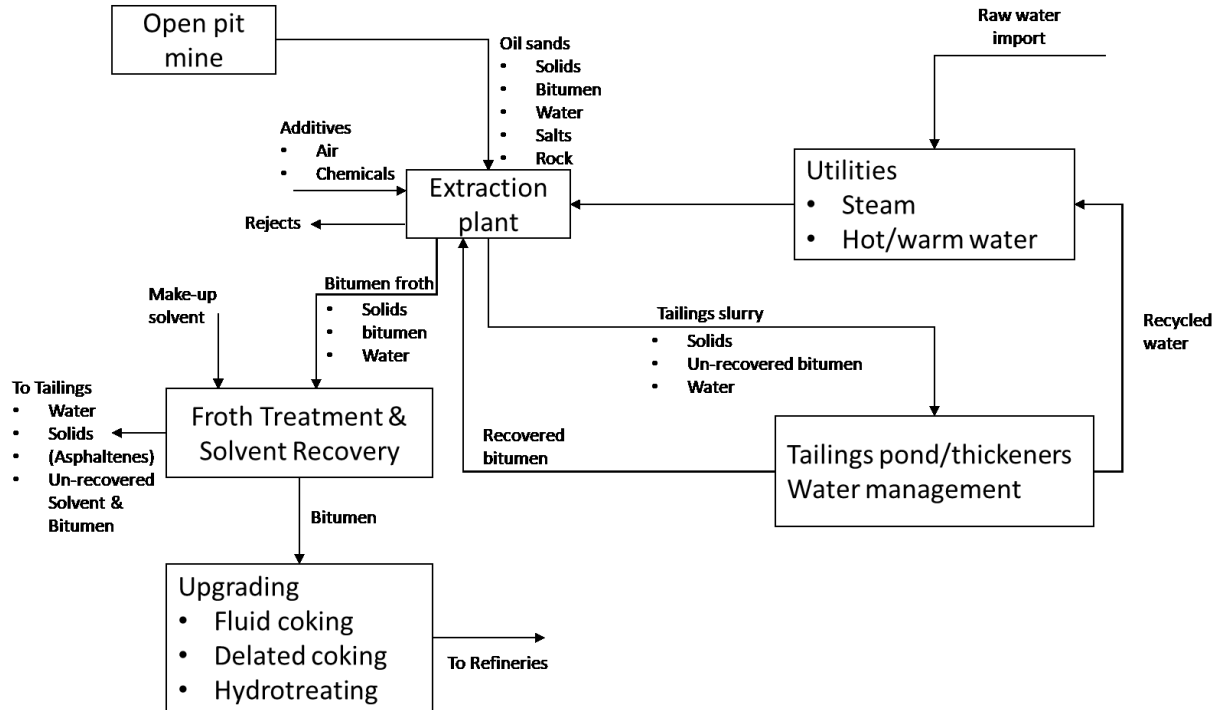


Figure 2-1 Schematic of water-based bitumen extraction process from oil sands (replotted from Masliyah et al.).³

2.2 Experimental Methods

2.2.1 Atomic force microscope

The atomic force microscopy (AFM) has been widely applied to directly measure the interaction forces in a wide range of colloidal systems. The interaction forces were converted from the cantilever deflection, which obeys Hooke's law.²³ The cantilever was driven towards the bottom object until a fixed maximum loading force was reached, at which point the cantilever was retracted. The interaction force as a function of displacement was recorded and further analyzed using MATLAB software.

AFM with colloidal cantilever techniques, which has been firstly used in 1994, could be applied to measure the interaction forces between different colloidal particles and solid surfaces/deformable drops.²⁴ The colloidal cantilever techniques have been widely applied to measure the interaction forces between different components involved in the oil sands extraction process. The interaction between two silica surfaces and silica and a bitumen surface can be investigated in different electrolyte solutions by applying a rigid silica sphere probe.^{8,22,25} In addition, the interaction between two bitumen surfaces can be achieved by using a dip coated hydrophobized silica probe in a bitumen solution.⁷ The interaction forces as a function of separation can be well predicted by the extended DLVO theory. Other than those, clay particles or other mineral particles can also be glued onto the tipless cantilever to study the interaction between clay particles and bitumen surface, which is crucial in slime coating.²⁶ It has been found that the addition of cations and the increasing ionic strength of the aqueous solution would decrease the repulsive force between the surfaces. The air bubble/oil drop could be immobilized on the bottom hydrophobic surface in order to measure the interaction between the top particle and bubble/oil drop, as shown in Figure 2-2a.¹⁰ The hydrophobic particle could induce the particle penetration onto the bubble/oil drop while the hydrophilic particle would prevent the attachment and form a stable water film. The interaction forces cannot be predicted by the SYRL model, due to the irregular shape of the particles.

The newly developed droplet probe AFM technique could be utilized to precisely investigate the interaction involving a deformable air bubble/oil drop. In this technique, a tipless cantilever with a gold patch was hydrophobized so that an air bubble/oil drop with a radius of 50-100 μm can be anchored onto it, functioning as the probe tip. Due to the smooth surface of the air bubble/oil drop and the large contact area of the tested surface, a more reliable and reproducible

result could be obtained compared with the colloidal probe AFM technique. Coupled with the established Stokes-Reynolds-Young-Laplace model, which took the disjoining pressure from surface forces and the deformation of air bubble/oil drop during interaction into consideration, the force-time profile and the spontaneous film thickness between air bubble/oil drop and surface could be precisely predicted.^{15,27} The drop probe AFM technique coupled with the SRYL model has been applied to investigate the interaction mechanism between two identical air bubbles/oil drops,²⁸⁻³¹ and between an air bubble/oil drop and a solid surface.^{20,21,32,33} A schematic of the experiment for measuring the interaction force between two air bubbles is shown in Figure 2-2b. This technique has been widely applied in many industrial systems, including mineral flotation process,³² oil sands extraction process,^{7-9,20-22,25} food emulsions stability³⁴ and so on, to control the interaction between deformable droplets and different components to improve the efficiency.

The drop probe AFM technique has been widely applied in the oil sands extraction process. To improve the bitumen aeration efficiency, the interaction between an air bubble and a bitumen coated silica wafer has been investigated in complex water chemistry by Xie et al.²⁰ and Bai et al.²¹ The experimental setup is shown in Figure 2-2c. It has been proved that the hydrophobic force between the air bubble and bitumen is the only attractive force that could induce the bubble-bitumen attachment. In addition, the effect of the novel secondary process aid, sodium citrate, has been proved cannot prevent the bubble-bitumen attachment in the presence of calcium ion at high ionic strength. The stability of the emulsified water or oil droplets has also been studied, which is crucial for increasing the bitumen content in and removing water from bitumen froth. Studies by Chen et al. proved that the adsorption of asphaltene at the oil/water interfaces would lead to an increasing EDL repulsion force and the steric repulsion, thus stabilizing the oil in water emulsion.³¹ While for the water in oil emulsion, the steric repulsion generated by the adsorbed asphaltene layer

is the main reason that stabilizes the emulsion. However, the lateral shearing could induce water coalescence in asphaltene solution due to the disrupted asphaltene coating.³⁰

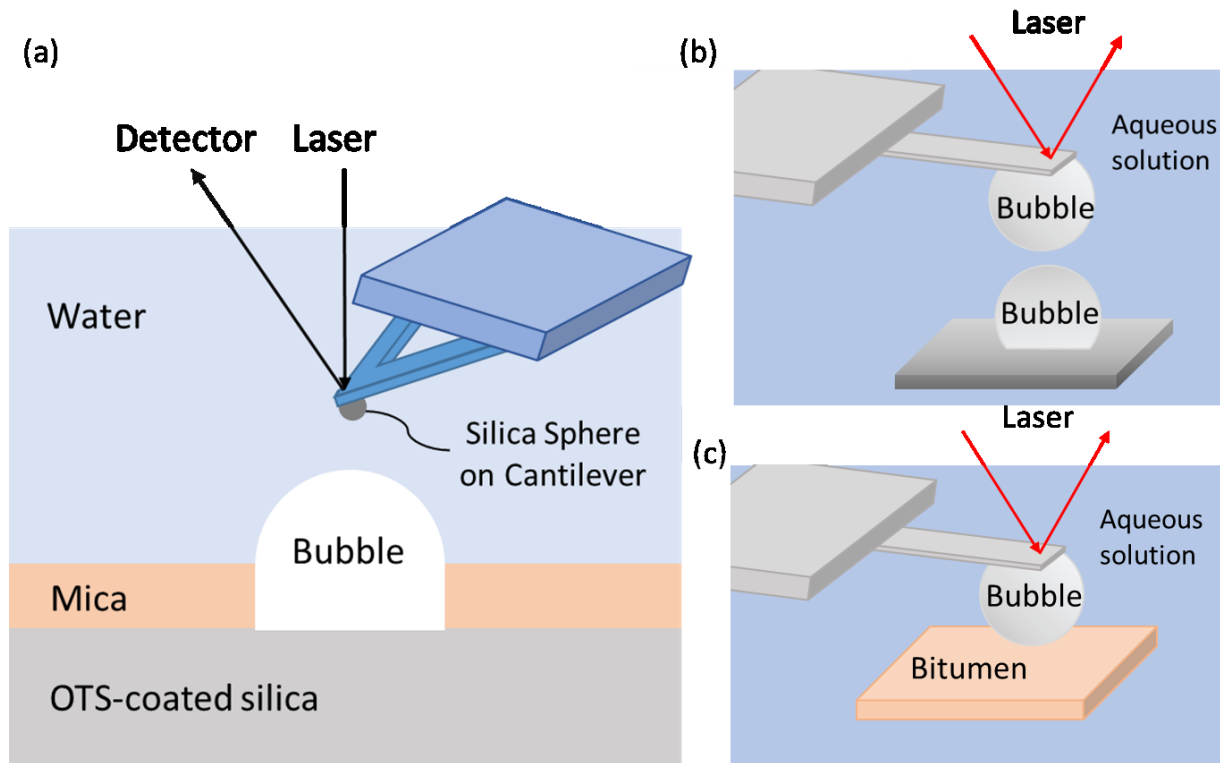


Figure 2-2 (a) Schematic figure of the experiment for measuring interaction forces between a silica particle and a surface air bubble.²⁴ (b) Optical microscopy image of a cantilever with an attached air bubble interacting with another surface air bubble.²⁸ (c) Schematic diagram of bubble probe AFM technique for measuring interaction forces between an air bubble and a bitumen surface.^{20,21}

2.2.2 Thin film interferometry method

The evaluation of the profile of the thin water film confined between two surfaces can be observed using the thin film interferometry method. By shining a light with a known wavelength on the thin liquid film, the light would reflect from both interfaces and change the intensity of the

recorded light to obtain fringes, from which we could obtain the film thickness profile using the following Eq. with nanometer accuracy.³⁵⁻³⁷

$$\frac{I(t) - I_{min}}{I_{max} - I_{min}} = \sin^2\left(\frac{2\pi nh(t)}{\lambda}\right) \quad (2-1)$$

where I is the light intensity and I_{max} and I_{min} are the maximum and minimum light intensities, respectively. The light wavelength is λ and the refractive indices of the liquid is n .

The Scheludko cell was designed applying the above method to directly observe the dynamic film drainage process between an air bubble and a solid surface. The schematic diagram of the Scheludko cell is shown in Figure 2-3a. The thin liquid film is formed by sucking out the liquid from a biconcave meniscus inside a capillary tube and the approaching speed of the top interface could be controlled by the suction rate.³⁸ The bottom object can be a drop or a solid surface. The light was shined through the thin liquid film from the bottom. In addition, by coupling the AFM and a reflection interference contrast microscopy (RICM), the interaction between an air bubble and mica surfaces with different hydrophobicity and the spatiotemporal film thickness was measured at the same time. The excellent agreement between the experimental value and the theoretical calculation was reached at a low bubble approach velocity within the micrometer range.³³

In AFM, the air bubble/oil drop barely deforms and the dynamic interaction is negligible due to its low approach velocity range ($<100 \mu\text{m/s}$). Similarly, using the Scheludko cell method, the hydrodynamic conditions are also confined within low Reynolds number regime ($\text{Re} = 2\rho RV/\mu_w < 10^{-2}$, where R is the bubble/drop radius, μ_w and ρ are the viscosity and density of aqueous phase, respectively). While the rising bubble method leads the film drainage dynamics to

fall in high Reynolds number regime ($Re > 50$).³⁹ The dynamic force apparatus (DFA) partially filled the intermediate Reynolds number regime and could achieve a higher Reynolds number from 0.027 to 37.75 by controlling the approach velocity from 0.01 to 10 mm/s. The time dependent interaction force and also spatiotemporal film thickness could be measured at the same time by applying this novel instrument.⁴⁰ The schematic diagram of the DFA is shown in Figure 2-3b. A stainless steel chamber filled with the target solution was placed on the stage of the inverted Axiovert 100 Carl Zeiss microscope. The top bubble/oil drop is generated by a capillary orifice with a radius of a millimeter. The speaker diaphragm coupled with a motorized actuator (THORLABS, Z825B) controlled the movement of the capillary. The size and the initial position of the top bubble/oil drop were monitored by a side view charged-coupled device (CCD) camera. For the measurement between two air bubbles or two oil drops, the two bubbles/oil drops were carefully aligned and monitored by the inverted microscope in order to realize a head-to-head collision. The substrate was attached to a bimorph cantilever (force resolution 0.1 μ N, 10,000 force points collected per second) that was used as the force sensor during the experiment to measure the interaction force when the bubble/drop was approached or retracted from the bottom interface. A halogen lamp (Hal 100, Zeiss) was used to shine the light on the bottom and top interfaces for the interference fringes, which were recorded using a high-speed video camera (Photron SA4, 60-500,000 fps), as shown in Figure 2-3c.

Zhang et al. applied the dynamic force apparatus to investigate the dynamics of the water film drainage process between an air bubble and a hydrophilic or hydrophobic solid surface.^{16,17,41} Experimental results and the theoretical modeling reveal the significant impact on the hydrodynamic boundary conditions at both air/water and solid/water interfaces.^{17,41} The DFA was also used to investigate the film drainage process between two air bubbles by Liu et al., which

proved that smaller surface bubbles lead to a faster coalescence due to the asymmetric film drainage at some stage.⁴² In addition, Liu et al. also provided a fundamental explanation of the reason of bubble coalescence time varying over 3 orders of magnitude.⁴³ Ivanova et al. firstly applied this instrument in the oil sands extraction process, to investigate the effect of the adsorption of asphaltene at water/oil interface on the film drainage process between a water drop and a hydrophobic or hydrophilic solid surface.¹⁸ This study has very important implications on the emulsion stability in bitumen froth and could help the industry to improve bitumen froth quality.

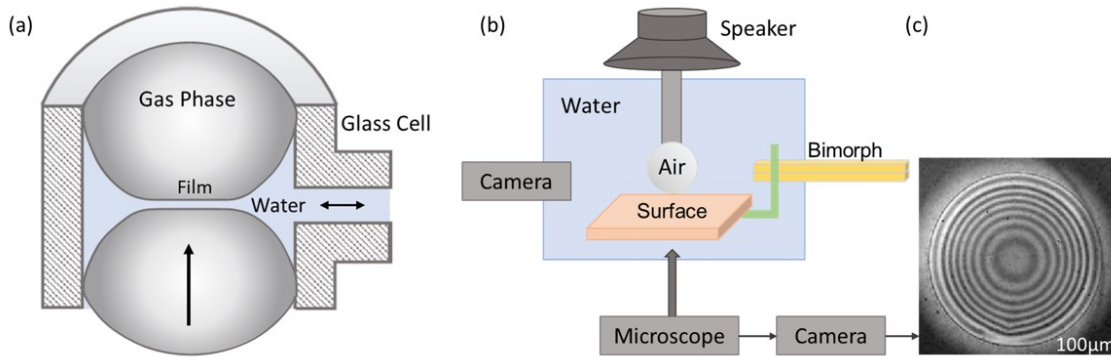


Figure 2-3 (a) Schematic for the “Scheludko” cell.³⁷ (b) Schematic diagram for the dynamic force apparatus.⁴⁰ (c) A snapshot for the observed fringes.

2.3 Stokes-Reynolds-Young-Laplace model

The Stokes-Reynolds-Young-Laplace (SRYL) model is used to model the film flow between the air bubble/oil drop and a solid surface. The pressure difference between the film region and the bulk solution is the driving force that controlled the film drainage process. For simplification, the axisymmetric film drainage is assumed in the following calculation. Lubrication theory is introduced to capture the film drainage dynamics by considering the pressure distribution and the surface deformation. The Young–Laplace equation is used to describe the drop profile. The

schematic illustration of the interaction between an air bubble/oil drop and a solid surface in the cylindrical coordinate system is shown in Figure 2-4a.

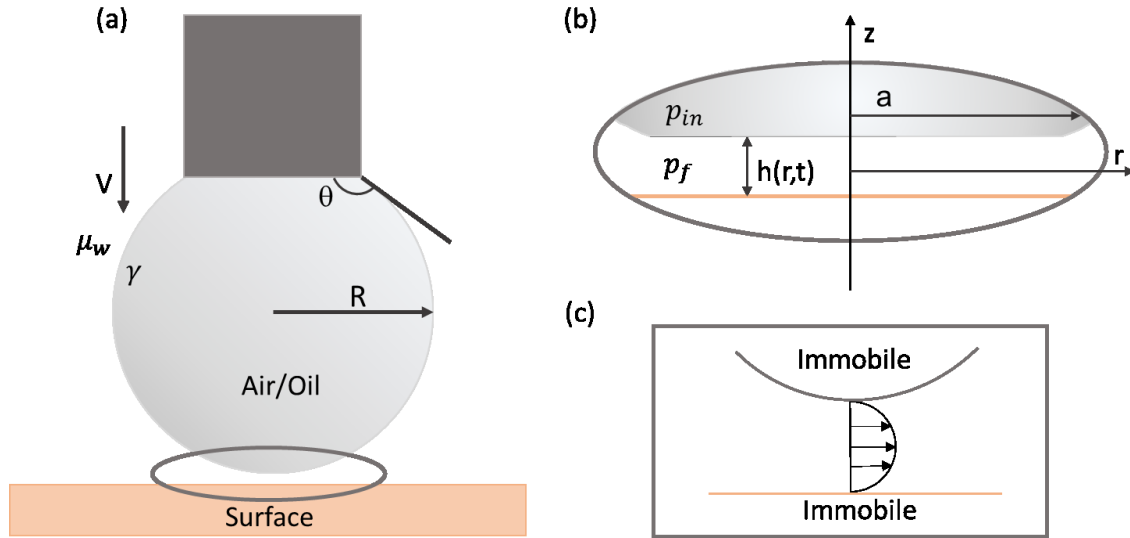


Figure 2-4 (a) Schematic illustration for air bubble/oil drop interacting with a solid surface and definition of parameters. (b) Enlargement of gray circle and definition of coordinate. (c) Schematic illustration for immobile-immobile boundary conditions.

2.3.1 Lubrication theory

The lubrication theory is simplified from the full Navier-Stokes equation to describe the liquid drainage process from thin film trapped between the deformable surface and solid surface. Three assumptions are made to permit the quantitative analysis of the film thickness $h(r, t)$ using the lubrication theory. Firstly, liquid flow is nearly unidirectional. Secondly, the fluid inertia in the film regime is negligible, which could be proved by the Reynolds number of the film flow $Re_f \ll 1$ ($Re_f = \rho h_f V_f / \mu_w$, where $\rho \sim 10^3 \text{ kg/m}^3$ is the density of water, $h_f \sim 1 \text{ }\mu\text{m}$ is the film thickness, V_f is the velocity at the air or oil/water interface and $\mu_w \sim 10^{-3} \text{ Pa}\cdot\text{s}$ is the viscosity of water). Thirdly, the interaction of two interfaces happens in a region of small radius a ($a \ll R$) and of a

small thickness h ($h \ll a$), as shown in Figure 2-4b. Within the axisymmetric film, we consider the velocity field inside the thin film from both r and z -direction $u(r, z, t)$ and $v(r, z, t)$, and according to the first assumption, $v \ll u$. Under the steady state and the incompressible flow condition, the Navier-Stokes equation in the z and r -direction can be simplified to:

$$\frac{\partial p}{\partial r} = \mu \frac{\partial^2 u}{\partial z^2} \quad (2-2)$$

$$\frac{\partial p}{\partial z} = 0 \quad (2-3)$$

where μ is the viscosity of the continuous medium and p is the pressure field inside the thin film.

In this scenario, the continuity equation can also be simplified to:

$$\frac{1}{r} \frac{\partial(ru)}{\partial r} + \frac{\partial v}{\partial z} = 0 \quad (2-4)$$

By integrating Eq (2-2) from the bottom surface ($z = 0$) to the top surface ($z = h(r, t)$), together with the boundary conditions at the solid/water and air or oil/water interface, we could obtain the film thinning rate as a function of the pressure.

The hydrodynamic boundary conditions at both solid/water and air or oil/water interfaces have been studied for several decades. Both no-slip and Navier-slip boundary conditions can be applied at the solid/water interface. In the no-slip boundary condition, the velocity of the layer of the liquid next to the solid surface is equal to the velocity of the solid surface. The physical origin of this boundary condition can be explained by the trapping of liquid molecules inside the pocket of the solid surface and has been demonstrated and accepted for numerous experiments and calculations.⁴⁴ However, some researchers recently doubted the applicability of the no-slip

boundary condition at some hydrophobic solid/water interfaces, claiming the Navier-slip boundary condition was more appropriate. This could be explained by the less attractive force between liquid molecular and solid surface leading to a fluid molecular slippery at the solid/water interface.^{41,45,46} The boundary condition at the air/water interface or oil/water interface of oil with comparable viscosity with water should be fully mobile in clean water. However, a tiny amount of surfactant or impurities in the water would transfer the boundary condition from mobile to fully immobile.^{47–49} In our study, we considered the immobile boundary condition at both solid/water and the surface velocity $U = 0$ (as shown in Figure 2-4c), which has been applied in numerous studies, to obtain:^{15,16,21,47,50}

$$\frac{\partial h(r, t)}{\partial t} = \frac{1}{12\mu r} \frac{\partial}{\partial r} \left(r h^3 \frac{\partial p(r, t)}{\partial r} \right) \quad (2-5)$$

where $h(r, t)$ is the film thickness between two interfaces, r is the radial coordinate, t is the time and $p(r, t)$ is the hydrodynamic pressure inside the water film..

2.3.2 Young-Laplace equation

The deformation of the air or oil/water interface caused by the combined effect of hydrodynamic and disjoining pressures was described by the augmented Young-Laplace equation, which assumes an equilibrium drop profile in response to the hydrodynamic pressure at any time. This assumption is satisfied due to the capillary waves of velocity (~ 1 m/s) being much higher than the characteristic approach velocities of air bubble/oil drop (up to 0.1 m/s). The augmented Young-Laplace equation is written as:

$$\frac{\gamma}{r} \frac{\partial}{\partial r} \left(r \frac{\partial h}{\partial r} \right) = p_{in} - p_f = \frac{2\gamma}{R} - p(r, t) - \Pi \quad (2-6)$$

In the above equation, the left hand side describes the curvature of the deformable surface where γ is the interfacial tension. The right hand side is the pressure difference across the interface. For most of the conditions, the pressure difference consists of Laplace pressure $2\gamma/R$, hydrodynamic pressure $p(r, t)$ and disjoining pressure Π . However, for some specific conditions, if the approach velocity of the air bubble/oil drop exceeds a certain value, extra stagnation pressure inside the deformable drop needs to be taken into consideration.⁵¹ The three terms on the right hand side control different stages of the film drainage process. The Laplace pressure leads to a spherical shape of the air bubble/oil drop when they are far away from the surface. When the air bubble/oil drop is approaching to the surface, the hydrodynamic pressure inside the film increases, resulting in a flattened surface. If the hydrodynamic pressure exceed the Laplace pressure, a dimple would form. The disjoining pressure determine the formation of a stable film or film rupture, which arises from the surface force by considering the extended DLVO theory.

2.3.3 Disjoining pressure

The disjoining pressure strongly affected the thin film drainage process, especially the film drainage rate and the final state of the thin film.^{52,53} The disjoining pressure is contributed from the surface forces, by mainly considering the van der Waals (vdW), electrostatic double layer (EDL), and hydrophobic interaction (HB) forces according to the extended DLVO theory:

$$\Pi = \Pi_{vdW} + \Pi_{EDL} + \Pi_{HB} \quad (2-7)$$

For the interactions involving hydrophilic surfaces, the contribution from the hydrophobic interaction in the disjoining pressure becomes negligible. The disjoining pressure due to the vdW interaction $\Pi_{vdW}(h(r, t))$ can be calculated:

$$\Pi_{vdW}(h(r, t)) = -\frac{A}{6\pi h^3} \quad (2-8)$$

where A is the Hamaker constant.

The disjoining pressure contributed from the EDL force is derived by solving the Poisson-Boltzmann (PB) equation. For the surface potentials below 50-80 mV, a linear PB equation by either assuming the constant charge or constant potential boundary conditions could be applied.⁵⁴ Studies had proved that the linear PB equation assuming constant potential boundary condition can describe the interactions between bubble and bitumen, bitumen and silica very well.^{8,20} The disjoining pressure due to EDL interaction assuming constant potential boundary condition for asymmetric systems can be calculated as:^{54,55}

$$\Pi_{EDL}(h(r, t)) = \frac{2\varepsilon_0\varepsilon\kappa^2[(e^{+\kappa h} + e^{-\kappa h})\Psi_1\Psi_2 - (\Psi_1^2 + \Psi_2^2)]}{(e^{+\kappa h} - e^{-\kappa h})^2} \quad (2-9)$$

where Ψ_1 and Ψ_2 are the surface potentials of two interacting objects, respectively. The Debye length κ^{-1} of the EDL force can be calculated as:

$$\kappa^{-1} = \left(\frac{\varepsilon\varepsilon_0 k_B T}{\sum_i n_{i0} e^2 Z_i^2} \right)^{\frac{1}{2}} \quad (2-10)$$

where ε_0 is the permittivity of vacuum, ε is the dielectric constant of the medium, n_{i0} is bulk concentration of electrolyte i and Z_i is the valence of ion i . For surface potentials higher than 80 mV, an accurate EDL interaction could be obtained by directly solving the non-linear PB equation.

The hydrophobic force is prove to be decaying exponentially with distance,⁵⁶ and can be calculated as:³³

$$\Pi_{HB}(h(r, t)) = -\frac{C}{2\pi D_0} e^{-\frac{h}{D_0}} = -\frac{\gamma(1 - \cos\theta)}{D_0} e^{-\frac{h}{D_0}} \quad (2-11)$$

where D_0 is the decay length of the hydrophobic interaction.

2.3.4 Initial and boundary conditions

The numerical solution of the Stokes-Reynolds-Young-Laplace requires suitable initial and boundary conditions. The initial film thickness is given by:

$$h(r, 0) = h_0 + \frac{r^2}{2R} \quad (2-12)$$

where h_0 is the initial separation between the center of air bubble/oil drop and solid surface.

We considered an axisymmetric system here, and a finite domain $0 < r < r_{max}$ was selected to calculate the film profile, where $r = 0$ is the center point of the film while $r = r_{max}$ is a carefully selected place outside the interaction.²⁷ Firstly, due to the axisymmetry, we can impose the conditions at $r = 0$:

$$\frac{\partial h}{\partial r} = \frac{\partial p}{\partial r} = 0 \quad (2-13)$$

At $r = r_{max}$, from the lubrication theory, the film thickness varies with a quadratic dependence in r , contributing to a pressure that decays like r^{-4} . This asymptotic behavior of the pressure can be expressed as:

$$r \frac{\partial p}{\partial r} + 4p = 0 \quad (2-14)$$

The final boundary condition at $r = r_{max}$ is to specify how the air bubble/oil drop is moved. There can be various forms of this boundary condition, depending on the experimental

system. For the bubble/drop-solid interaction, considering the approach velocity of bubble/drop and the deformation of the bubble/drop, the boundary condition can be expressed as:

$$\frac{\partial h(r_{max}, t)}{\partial t} = V - \frac{1}{2\pi\gamma} \frac{dF(t)}{dt} \left(\log \left(\frac{r_{max}}{2R_0} \right) + B(\theta) \right) \quad (2-15)$$

With pinned three-phase contact line, we have:

$$B(\theta) = 1 + \frac{1}{2} \log \left(\frac{1 + \cos \theta}{1 - \cos \theta} \right) \quad (2-16)$$

With a constant angle θ , we have:

$$B(\theta) = 1 + \frac{1}{2} \log \left(\frac{1 + \cos \theta}{1 - \cos \theta} \right) - \left(\frac{1}{2 + \cos \theta} \right) \quad (2-17)$$

where θ is the angle the bubble/drop make at the surface. The interaction force is calculated by integrating the excess hydrodynamic pressure and the disjoining pressure from the center to infinity based on the Derjaguin approximation:

$$F(t) = 2\pi \int_0^{\infty} [P(r, t) + \Pi(h(r, t))] r dr \quad (2-18)$$

2.4 Remaining questions

Although the surface force measurement and the thin film interferometry method has been widely applied in the oil sands extraction process to investigate the interaction mechanisms among bitumen, air bubble, sand, and clay particles. However, there are still some remaining questions unsolved, which will be reviewed in this section.

2.4.1 A novel secondary processing aid

The water-based bitumen oil sands extraction process is often conducted in a weakly alkaline environment. Inorganic bases, such as sodium hydroxide, are good process aids for the bitumen extraction process.⁵⁷ However, it has been shown that adding sodium hydroxide only slightly enhances the extraction of poor-processing ores. Schramm et al. found that the bitumen recovery of poor processing ore could only reach an average level when a high dosage of sodium hydroxide was added.⁵⁸ Therefore, many researchers studied the usage of different chemical aids to increase the bitumen recovery from poor-processing ore that do not exhibit detrimental effects on the environment.^{58,59}

Recently, sodium citrate was used as a secondary processing aid and was applied in the water-based bitumen extraction combined with sodium hydroxide. It has been found that the combination of sodium hydroxide and sodium citrate can significantly increase the bitumen recovery and froth quality not only from good processing ore but also from the poor processing ore.⁶⁰ Sodium citrate is a non-toxic and environmentally friendly chemical. Compared with the traditional caustic, the usage of sodium citrate had a minimal detrimental effect on oil sand processing and would not result in environmental pollution. Successful application of sodium citrate in the oil sands industry not only reduced the usage of caustic but also enhanced the processability of poor ore.

However, the mechanism of how sodium citrate enhanced the oil sand extraction still remains unclear. Xiang et al. found that adding sodium hydroxide and sodium citrate together could decrease the zeta potential of both bitumen droplets and silica particles compared with adding sodium hydroxide and sodium citrate alone. The increase in negative surface charges of both silica and bitumen would lead to an increase of the repulsive electrostatic double-layer force,

thus reducing the adhesion force between bitumen and silica. This would significantly enhance bitumen liberation.²² Other than that, the addition of sodium citrate would also facilitate the bitumen receding from the silica surface, which also proves the enhancement of bitumen liberation in the presence of citrate.⁶¹ In addition, it was found that citrate depressed the effect of divalent ions such as Ca^{2+} and Mg^{2+} , which was due to the chelating reactions between citrate and divalent ions. Gan et al. found that adding citrate into the solution with the presence of multivalent ions could prevent the coagulation between some particles (kaolinite) and oil (bitumen).^{62,63} This finding indicated that citrate has some effect on preventing bitumen slime coating in the oil sands extraction process, which could facilitate the attachment between bitumen and air bubble. Wang et al. studied the effect of citrate on the flotation of quartz with a sodium oleate collector in the presence of Ca^{2+} and pointed out that the depression mechanism of citrate was mainly attributed to two aspects. The first aspect was that citrate can desorb the Ca^{2+} adsorbed on quartz. The second aspect was that the chelating reaction between citrate and the adsorbed Ca^{2+} can block the subsequent adsorption of sodium oleate on quartz.⁶⁴

The effect of citrate on bitumen liberation and slime coating has been widely explored. However, the effect of citrate in combination with sodium hydroxide on bitumen aeration also lacks study. In addition, it is widely known that bitumen would exhibit a more negative zeta potential in citrate solution at alkaline conditions. However, the reason why citrate can change those surface properties is still not fully understood.

2.4.2 Viscosity and interfacial elasticity of bitumen

Bitumen is a form of petroleum in oil sands ore which has a high molar mass and extreme viscosity, which contains thousands of hydrocarbon components. Based on the solubility characteristics, bitumen can be separated into different classes. Asphaltenes are defined as the

fractions in bitumen that are soluble in aromatic solvents but insoluble in paraffinic solvents. The fractions that are soluble in n-pentane are referred to as maltenes, which can be further separated into the following fractions: saturates, aromatics and resin. The complex chemical structure provides specific properties of bitumen.

The viscosity of different source of bitumen can range from 100-1000 Pa·s at room temperature and standard atmospheric pressure.⁶⁵⁻⁶⁷ It has been found that the viscosity of bitumen is highly dependent on the chemical composition, especially the asphaltene content.⁶⁸ The increasing asphaltene content could significantly increase bitumen viscosity at low temperatures. In addition, the viscosity of bitumen is also sensitive to solvent addition and temperature.^{65,69} In some macroscopic experiments, it has been proved that the bitumen viscosity influence both bitumen liberation and aeration.^{69,70} A decrease in bitumen viscosity would increase the rate of bitumen liberation and also facilitate the bubble-bitumen attachment.^{11,65} In the industrial application, a relatively high temperature is applied for better extraction efficiency. However, the effect of the viscosity is barely taken into consideration while investigating the thin film drainage process or the surface force measurement in the system involving bitumen. The solvent diluted bitumen or asphaltene drops were usually used to study the dynamic film drainage process,^{18,71} while a bitumen-coated surface was applied in the surface force measurement.^{7,8,20-22} In those cases, compared with the real industrial system, the effect of bitumen viscosity has not been focused on, which might have a strong effect on the dynamic interaction.

Other than the bulk viscosity of bitumen, it has been proved that a mechanically strong, viscoelastic, and rigid interfacial film would form at the bitumen/water interface, which would be able to resist bitumen droplet coalescence.⁷² Many “bulk” studies showed that increased interfacial rigidity is a crucial factor for keeping the bitumen in water emulsion stability.⁷³ Some studies using

asphaltene solutions or diluted bitumen also proved that the adsorption of asphaltene at the interface is the reason preventing droplet coalescence. As a good solvent for asphaltene, the adsorbed asphaltene at the toluene/water interface would not only increase the EDL repulsion but also create the steric repulsion between the surfaces, thus increasing the repulsive force between two asphaltene drops and preventing coalescence.³¹ Using an asphaltene model compound, the existence of a steric layer, revealing a rigid cortical structure at the oil/water interface, has been observed experimentally and quantitatively characterized using the crumpling ratio measurement.^{74,75} It showed that increasing asphaltene concentration and aging time would significantly increase the crumpling ratio for O/W emulsion, thus increasing the oil droplet coalescence time.⁷⁴ In addition, by applying the interferometry method, the precipitated asphaltene particles and/or asphaltene-resin aggregates have been observed at the asphaltene in heptol/water interface and prevent the thin film drainage process.⁷¹ For the W/O system, the thin film drainage and interaction forces between two asphaltene drops in water cannot be predicted by the SRYL model due to the non-Newtonian film formed at the interface.^{76,77} However, the general understanding of the emulsion stabilization mechanism is available from the “diluted system”. Limited knowledge is available on the thin film drainage by considering both the interfacial film and the bulk viscosity.

2.4.3 Hydrophobic interaction

The hydrophobic interaction is an attraction between two nominally hydrophobic surfaces. The hydrophobic surface cannot form hydrogen bonds with the surrounding water molecules. The water molecules rearrange themselves by pointing the “dangling” –OH groups with hydrogen atoms to the surface.⁷⁸ This hydrogen bond depletion hindered the reorientation of water molecular dipole and resulted in the occurrence of a persistent dipole pair, giving rise to a structured water

shell around the hydrophobic surface.⁷⁹ The coalescence of two hydrophobic surfaces in water could break the structured shell and increase the water configuration entropy near the hydrophobic surface, leading to an attractive force between two hydrophobic surfaces.⁸⁰ This is the origin of the “intrinsic” hydrophobic interaction. This kind of hydrophobic force is usually short ranged, with the decay length within the range of 0.3-1 nm, depending on the molecular structure of the hydrophobic surfaces.^{81,82}

Some long-ranged hydrophobic forces have also been proposed in the previous study and were explained by several mechanisms. The first mechanism mistakenly includes some additional forces in the hydrophobic force measurement. Meyer et al. observed a long-ranged hydrophobic force between two neutrally charged hydrophobic surfaces that can be explained by the electrostatic attraction between positively and negatively charged micrometer-sized regions on the surface. The oppositely charged regions counterbalance each other, resulting in an overall neutral surface.⁸³ Tsao et al. claimed that the electrical field originated from the in-plane polarized domain of the ordered carbon chains is the reason for the long-range attraction force in their observation.⁸⁴ Other than the electrostatic interaction, the cavitation and capillary bridging from the presence of surface nanobubbles could also be the reason for the observation of the long-range “hydrophobic force”.^{85,86} The works in Yoon’s group claimed that the long-range hydrophobic force was caused by the structure change of water molecule between hydrophobic surfaces, and can be calculated by an extra term in the DLVO theory.^{87,88}

The bitumen surface is highly charged, and the zeta potential can vary significantly with pH, the electrolyte type and concentration in the solution, which can be explained by the accumulation of the functional groups on the bitumen/water interface. This phenomenon makes bitumen to possess a hydrophilic character. However, in the system involving bitumen, a

hydrophobic force is always taken into consideration while modeling the interaction forces between the bitumen surface and another hydrophobic surface. Studies have found that the surface charge of the bitumen varies significantly across the bitumen surface, indicating the non-uniform distribution of polar groups.^{89,90} The hydrophobic sites, such as those in asphaltenes, also exist on the bitumen/water interface to contribute to the hydrophobic behavior of bitumen. It has been proved that the decay length of the hydrophobic force between an air bubble and a bitumen surface is around 1 nm, which is a reasonable decay length of the “intrinsic” hydrophobic force.^{20,21}

2.4.4 Pressure difference between deformable drop and surrounding solution

In the SRYL model, the Young-Laplace equation describes the droplet profile in response to the pressure difference across the interface. As a result of the interfacial tension, the pressure difference between the inside and outside of a curved surface is named the “Laplace pressure”. However, some studies found that the formation of a “dimple” (an inversion of the curvature of the aqueous film appears at some stage) in the thin film drainage process is a result of interfacial tension, gravity, fluid inertial, and the viscous normal stress.^{51,91} It has been proved that an extra pressure difference across the interface contributed from gravity and fluid inertial need to be taken into consideration when the Weber and Eötvös numbers satisfy $W_e = 1 + E_o$ ($W_e = \rho_{in}RV^2/\gamma$, ρ_{in} is the density of the bubble/drop, R is the radius, V is the approaching velocity and γ is the interfacial tension. $E_o = \rho_{in}gR^2/\gamma$, where g is the acceleration of gravity).⁵¹

**Chapter 3 Controlling the Interaction Forces
between an Air Bubble and Oil with Divalent
Cations and Sodium Citrate**

Abstract

Manipulating the interaction forces between an air bubble and oil is of great importance in many industrial processes, such as oil sands extraction. Recently, sodium citrate has been applied in the hot-water extraction process to improve the recovery of bitumen from mined oil sands. In this study, bubble probe atomic force microscopy was used to directly investigate the effect of Na_3Cit on the interaction force between an air bubble and a bitumen surface in different water chemistries. The experimental forces were compared with the Stokes-Reynolds-Young-Laplace film drainage model considering contributions from surface forces, and the theoretical calculation indicated that competition between the electrostatic double layer (EDL) force and the hydrophobic force determined the bubble-bitumen attachment. In pure electrolyte solution at pH 8.5, it was observed that the ionic strength required to induce bubble-bitumen attachment followed $\text{CaCl}_2 < \text{NaCl} < \text{Na}_3\text{Cit}$. The zeta potentials of both the air bubble and bitumen surfaces increased in magnitude in the same order, indicating that the stability in sodium citrate was caused by EDL repulsion. In the presence of CaCl_2 , the addition of Na_3Cit changed both bitumen zeta potential and Debye length, modulating the EDL interaction and affecting bubble bitumen attachment behavior. By performing a series of experiments containing both CaCl_2 and Na_3Cit , a stability map was produced. Compared to sodium citrate alone, the copresence of CaCl_2 and Na_3Cit facilitated bubble-bitumen attachment. Once the CaCl_2 concentration exceeded 5 mM, bubble-bitumen attachment always happened, regardless of the Na_3Cit concentration. The findings provide insight on how Na_3Cit , in combination with CaCl_2 , affects bubble-bitumen attachment and offer valuable information on controlling the interaction force between the air bubble and bitumen by adjusting the water chemistry.

3.1 Introduction

The interaction between air bubbles and oil droplets is of critical importance to many established industrial and environmental processes, such as mineral flotation⁹² and oil sands extraction.³ The coagulation of air bubbles with oil droplets is thermodynamically favorable, enabling the collection of heavy oil droplets or oil-engulfed mineral particles from an aqueous medium by aeration.^{3,92} The attachment efficiency between an air bubble and an oil droplet directly determines the mineral or oil recovery, making it a crucial factor in froth flotation.³ However, microscopically, an energy barrier exists between an air bubble and an oil droplet in aqueous solution that can hinder their attachment.^{5,93} This energy barrier can be calculated using the extended DLVO (EDLVO) theory^{93,94} in which van der Waals (vdW),⁹⁵ electrostatic double layer (EDL),⁹⁵ and hydrophobic (HB) forces all contribute.⁵⁶ The EDL force is highly affected by water chemistry, including solution pH,^{12,58,96,97} electrolyte concentration,^{8,20} multivalent ion concentration,⁸ and surfactants.¹⁰ In many systems, the hydrophobic attraction is the main driving force for the attachment of the air bubble to oil droplets.^{3,20}

Oil sands comprise the largest oil reserves in Canada. Bitumen, a highly viscous oil with a density near that of water, is currently extracted from mined oil sands using a water-based extraction process.³ In this process, the oil sands are added to warm, alkaline water that helps liberate the bitumen from sand grains; the bitumen is then aerated by either entrained or introduced air bubbles, causing the bitumen to float while the sand sinks. Chemical aids, primarily sodium hydroxide, are introduced into the water-based oil sand production process to enhance the bitumen extraction performance.^{57,59,98} Recently, a novel secondary processing aid, sodium citrate, was found to significantly increase the bitumen recovery and froth quality when used in combination with sodium hydroxide in the oil sand extraction process.⁶⁰ Sodium citrate can chelate with

adsorbed multivalent ions or desorb multivalent ions from the bitumen surface, which both result in more negatively charged bitumen surfaces, enhance bitumen liberation, and prevent bitumen-clay aggregation.^{22,62,64} According to the EDLVO theory, the higher charge exhibited by the bitumen surface in the presence of sodium citrate would increase the EDL repulsion between air bubbles and bitumen, thus increasing the energy barrier and decreasing the bubble-bitumen attachment probability and flotation rate. This research seeks to control the interaction between the air bubble and bitumen by modifying the water chemistry and sodium citrate concentration.

The aim of this study is to investigate the effect of sodium citrate on bubble-bitumen attachment in combination with sodium hydroxide and calcium chloride using bubble-probe atomic force microscopy (AFM). This technique has been applied to study the interaction mechanism between deformable oil drops^{31,32} and air bubbles.^{28,33,53} We employ the Stokes-Reynolds-Young-Laplace (SRYL) model²⁷ to evaluate the contribution of different surface forces, including vdW, EDL, and HB, under different water chemistry (e.g., ionic strength, electrolyte) to further elucidate the factors controlling the bubble-bitumen interaction. The SRYL model can provide relevant nanoscale information including quantitatively understanding the combined effect of hydrodynamics, surface forces, and drop deformation on the interaction in different drop or bubble systems.^{28,31-33,53} Our research could provide guidance for the industry on the selection of the appropriate operational concentrations of different chemical aids.

3.2 Experimental section

3.2.1 Materials

The vacuum distillation unit (VDU) feed bitumen provided by Syncrude Canada, Ltd. was used in this study. The substrate used in the AFM force measurement was prepared by treating a

silica wafer (NanoFAB, CA) with octadecyltrichlorosilane (OTS) ($\geq 96\%$ purity, Sigma-Aldrich). Ethanol (for high-performance liquid chromatography, Acros Organics), 1-dodecanethiol ($\geq 98\%$, Sigma), sodium dodecyl sulfate (SDS, 99% purity, Sigma), and toluene (99.8% purity, Sigma) were used without any purification. Sodium chloride (NaCl, ACS grade, Fisher Scientific) and calcium chloride dihydrate ($\text{CaCl}_2 \cdot 2\text{H}_2\text{O}$, ACS grade, Fisher Scientific) were roasted in an oven at $600\text{ }^\circ\text{C}$ for 8 h before use to remove organic contaminants. All aqueous solutions were prepared using Milli-Q water with a resistivity of $18.2\text{ M}\Omega \cdot \text{cm}$ deionized by a Barnstead Nanopure system (Thermo Fisher Scientific). Hydrochloric acid (HCl, ACS reagent grade) and sodium hydroxide (NaOH, ACS reagent grade) purchased from Fisher Scientific were diluted to 1 N and used to adjust the solution pH.

3.2.2 Preparation of the bitumen surface

Silica wafers were first cut into $12\text{ mm} \times 12\text{ mm}$ pieces and then sonicated in a 2 wt % SDS solution for 10 min. The silica wafer was then sonicated in Milli-Q water for 10 min, dried with a stream of nitrogen gas, and treated with UV/ozone for 10 min to ensure adequate hydroxylation of the silica surface and remove the trace amount of organic contaminants on the surface. The cleaned silica wafer was then immersed in an OTS in toluene (0.1 vol %) solution for 30 s. After that, the treated silica wafer was rinsed with toluene and dried with nitrogen gas. This process resulted in a slightly hydrophobic (water contact angle around 80°) surface. The hydrophobic silica wafer ensured a stable thin layer of bitumen on the surface throughout the experiment.

To prepare the bitumen layer on the hydrophobic silica wafer, diluted bitumen solution was prepared by adding bitumen into toluene at a concentration of 3 mg/mL. The diluted bitumen solution was then centrifuged 5 times at 20 000 g for 15 min to remove fine solids. After that, the

supernatant was filtered through a PTFE membrane (0.2 μm). A spin coater (Laurell WS-400A-6NPP/Lite) was used to prepare a thin layer of bitumen on the hydrophobic silica wafer. About 4 drops of filtered, diluted bitumen was added onto the substrate spinning at a velocity of 2000 rpm for 50 s to ensure uniform coverage on the substrate. Then, the substrate was rotated at 4500 rpm for an additional 40 s to remove the excess solvent. Finally, the bitumen-coated silica wafer was dried in a dust-free chamber overnight at room temperature to remove the remaining trace of toluene.

3.2.3 Zeta potential measurement

Diluted bitumen was prepared at a 1:4 mass ratio of bitumen:toluene and centrifuged at 10 000 g for 15 min to remove fine solids. Then, 1 mL of the diluted bitumen was added into 40 mL of the target aqueous solution and heated to 85 $^{\circ}\text{C}$ for 40 min to evaporate the toluene. The bitumen was assumed to be free of fine solids and solvent. Then, 40 mL of bitumen emulsion was generated by a Model 550 sonic dismembrator (Fisher) for 15 min at an amplitude of 70%.

For the zeta potential measurement, 2 mL of the bitumen emulsion was added into 100 mL of the target solution. A Brookhaven ZetaPALS was used to determine the electrophoretic mobility of bitumen droplets at 22 $^{\circ}\text{C}$. The zeta potential was calculated from the electrophoretic mobility using the Smoluchowski equation. The effective diameter of the bitumen droplets was measured with the ZetaPALS to be around 1.5 μm , and the ionic strengths of the solutions used in this study were ≥ 10 mM. Therefore, the Debye length, $1/\kappa$, was less than 3.04 nm, and $\kappa a \gg 1$, meaning the Smoluchowski equation could be used to calculate the zeta potential from electrophoretic mobility measurements.⁹⁹ The zeta potential of each sample was measured with 10 runs of 5 cycles each. The standard deviation for each sample was within ± 5 mV.

It is worth noting that the ionic strength and aqueous speciation under all conditions were calculated using the Visual MINTEQ 3.1 program,¹⁰⁰ and it was assumed that no significant amount of ions were removed from or adsorbed to the bitumen surface. In addition, all solution conditions were determined to be undersaturated with respect to calcium citrate.

3.2.4 Force measurement

The interaction force between an air bubble and the bitumen surface was measured using a bubble tip MFP-3D AFM system (Asylum Research, Santa Barbara, CA) coupled with a Carl Zeiss Axiovert 200 inverted microscope. A schematic of the experimental setup is shown in Figure 3-1. By controlling the distance between the cantilever and the substrate, shown as $X(t)$ in Figure 3-1, the interaction force between the air bubble and surface was recorded from the cantilever deflection, which obeys Hooke's law, through laser beam reflection.

To prepare a bubble tip, a glass slide was first rinsed in a 10 mM OTS in toluene solution for 10 s to form a slightly hydrophobic surface. The water contact angle of the glass slide was about 30°-40°, which is enough to immobilize a small air bubble. A custom-made, ultrasharp glass pipet was used to generate the air bubble in the aqueous solution within the AFM fluid cell and attach it to the slightly hydrophobic glass slide. A rectangular silicon AFM cantilever ($L \times W \times H$: 400 $\mu\text{m} \times 70 \mu\text{m} \times 2 \mu\text{m}$) with a circular gold patch (diameter 65 μm , thickness 30 nm) was used to anchor the air bubble. The cantilever was immersed in 10 mM dodecanethiol in absolute ethanol overnight to hydrophobize the circular gold patch. The spring constant of the cantilever was measured using the Hutter and Bechhoefer thermal tune method, and the spring constant was about 0.2-0.3 N/m.³⁶ Immediately prior to force measurement, the bubble tip probe was formed by contacting the gold patch on the cantilever with an air bubble attached to the slightly hydrophobic

glass slide. The cantilever was then retracted, and the air bubble was transferred from the glass slide to the cantilever tip.

To investigate the interaction between the air bubble and the bitumen surface, the AFM bubble tip was placed above the bitumen surface. The cantilever was driven toward the bitumen surface until a fixed maximum loading force was reached, at which point the cantilever was retracted. The interfacial tension of the air bubble was measured in the presence of the bitumen surface, and it remained constant over 1 h, the maximum length of any experiment (see the Appendix A). The driving velocity of the cantilever was set at 1 $\mu\text{m/s}$ to minimize hydrodynamic effects. The force versus displacement curves were plotted in the Asylum software (Igor Pro, WaveMetrics, Inc., USA) and MATLAB. Force measurements were performed at least five times for each aqueous condition using different bitumen surfaces with different air bubbles at different positions on the bitumen surfaces to confirm reproducibility. The bubble was observed before and after the experiments following a procedure that was adopted from Vakarelski et al.²⁸ to confirm that the bubble size remained the same within the experimental time frame. Furthermore, replicated force curves did not significantly change over time, further indicating the bubble size stability (see the Appendix A).

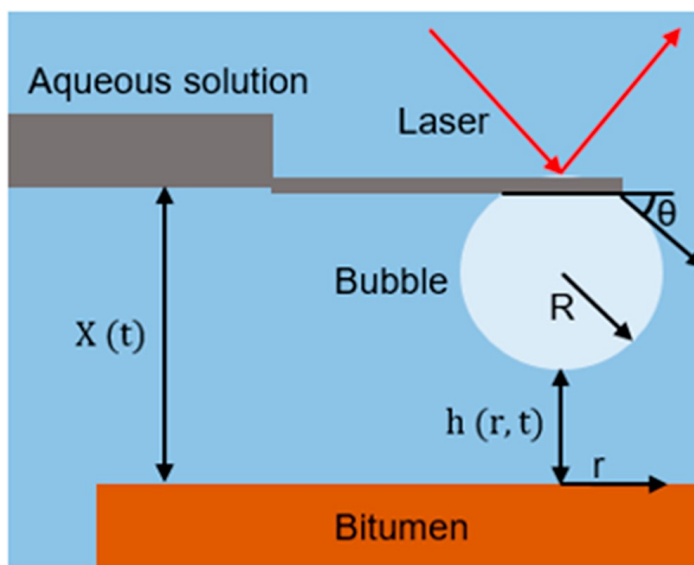


Figure 3-1 Schematic diagram of the AFM experimental setup. A bubble is anchored to an AFM tip that is driven toward the bitumen surface. θ is the water contact angle of the circular gold patch on the cantilever. The interaction force is extracted by the deflection of the cantilever as a function of displacement, which is the change of $X(t)$ over time.

3.3 Result and discussion

In this section, we report experimentally determined zeta potentials of bitumen, provide force measurements between a bubble and a bitumen surface using AFM, and compare the experimental force data with the SRYL model. Finally, we construct a stability map of bubble-bitumen interactions under different water chemistry.

3.3.1 Bitumen zeta potential

The zeta potential of bitumen droplets in pure aqueous NaCl, CaCl₂, and Na₃Cit solutions at pH 8.5 is shown in Figure 3-2A. Bitumen droplets were negatively charged under all experimental conditions. The negative charge originates from the organic molecules within bitumen that contain many functional groups including carboxyls, amines, sulfonates, and sulfates,

among others.^{58,101} In alkaline solution, these surface-active components will transfer to the bitumen surface with the polar functional groups facing aqueous solution. According to the ionizable surface group model (ISG), the surface charge on the bitumen surface originates from the dissociation of functional groups, including carboxyl group and amine groups among others. Assuming a large carboxyl content, bitumen in solutions of alkaline pH would carry negative charge due to the dissociation of the carboxyl group.^{58,96,97} It is worth noting that the direct identification of these surface functional groups is hard to achieve due to the complexity of bitumen. Although the functional group content of bulk bitumen can be estimated through analytical methods such as total acid number (TAN) ¹⁰² titration and FTIR,^{103,104} analytical identification of surface functional groups is severely complicated by the dynamic interaction of bitumen with the aqueous phase. Some researchers have used adsorption of Ni²⁺ and other metallic cations to quantify the surface carboxyl group density of particles and surfaces with known structure.¹⁰⁵ However, the complexity of the bitumen phase makes it difficult to identify the surface functional groups using methods such as these.

The magnitude of the zeta potential decreased with increasing NaCl concentrations from increased screening of the negative charge by sodium ions.^{8,97} The calculated charge at the Stern plane showed a similar trend with the zeta potential as shown in the Appendix A. Bitumen droplets exhibited significantly more negative zeta potential in sodium citrate solutions under all concentrations tested with a minimum zeta potential of about -130 mV observed in 1 mM sodium citrate. The corresponding charge at the Stern plane was calculated to be -0.0576 C/m² (Appendix A), which was much higher than that in NaCl solution. At concentrations greater than 1 mM sodium citrate, the magnitude of the zeta potential of bitumen droplets slightly decreased due to the increase of sodium concentration and associated screening ability. This phenomenon has also

been found by Xiang et al.,²² which is likely due to the removal of naturally occurring multivalent metal ions from the bitumen surface by citrate. The zeta potential of the bitumen droplets leveled off at approximately -116 mV when the sodium citrate concentration was increased to about 12 mM. However, the magnitude of charge at the Stern plane kept increasing as the sodium citrate concentration increased. This is because more surface charge is required to have the same zeta potential in higher electrolyte solutions.¹⁰⁶

Zeta potentials of bitumen droplets in all tested concentrations of CaCl_2 were less negative compared to NaCl and Na_3Cit . In addition, the calculated charges at the Stern plane of bitumen droplets in CaCl_2 solution were all less than those in NaCl solution. This is possibly due to specific adsorption of calcium ions on the carboxyl groups on the bitumen surface.^{7,62} Chow et al. used the ISG model to calculate the mobility of the bitumen droplets in CaCl_2 solution at various concentrations and pH values using dissociation constants for RCOOCa^+ and RCOOH from the literature and Gouy-Chapman theory. The good correlation between the theoretical calculation and the experimental data indicated that the reaction between carboxyl groups on the bitumen surface and Ca^{2+} reduces the negative charge on the bitumen surface. Their theoretical calculation also fits well with our experimental data.¹⁰⁷ With increasing CaCl_2 concentration, the bitumen zeta potential slightly increased, which was likely caused by increased screening from Ca^{2+} near the bitumen surface.

Figure 3-2B shows the bitumen zeta potential in 4 mM CaCl_2 with various Na_3Cit concentrations. When increasing the Na_3Cit concentration from 0.17 to 3.4 mM, the zeta potential of bitumen droplet became more negative, from approximately -40 mV to roughly -80 mV. This is caused by the decreasing free Ca^{2+} concentration in the bulk solution with increasing citrate concentration. However, a further increase of Na_3Cit concentration caused the zeta potential to

become less negative, possibly due to the reduced marginal chelating effect of citrate and the high concentration of Na^+ .

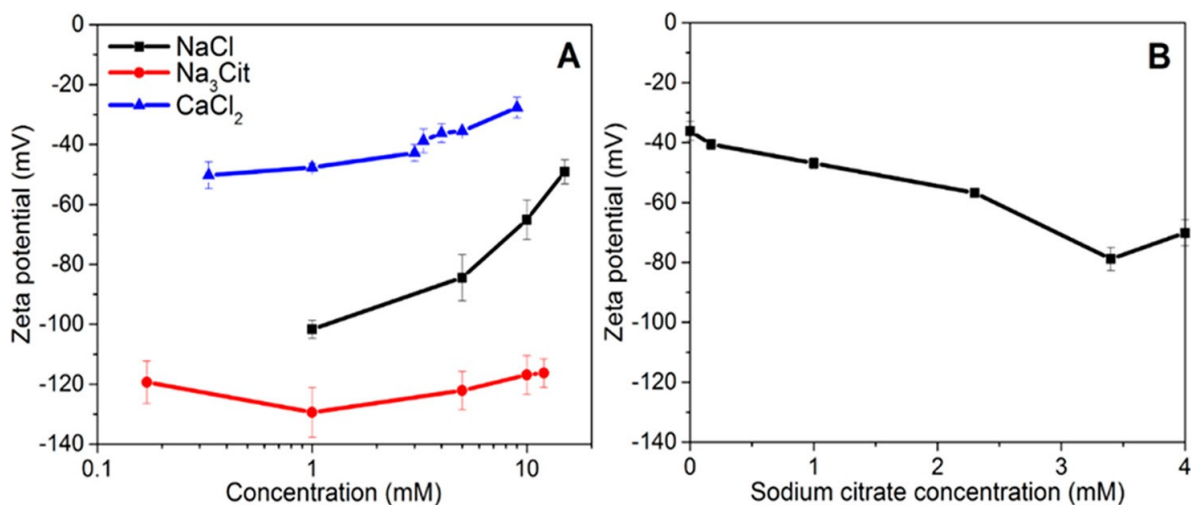


Figure 3-2 Zeta potential of bitumen droplets at pH 8.5 in (A) pure electrolyte solution with different concentration and (B) 4 mM CaCl_2 with different concentrations of Na_3Cit . The solid lines between dots are a guide to the eye.

3.3.2 Bubble-bitumen interaction in pure electrolyte solutions at pH 8.5

The interaction forces between an air bubble and bitumen surface in Na_3Cit , NaCl , and CaCl_2 solutions at pH 8.5 as determined by bubble probe AFM are presented in the following subsections. During the discussion, Stern potential refers to the potential of bubble or bitumen surfaces from fitting of the SRYL model to experimental AFM force curves. Zeta potential values were determined from the electrophoretic mobility of suspensions using a ZetaPALS instrument.

3.3.2.1 Na_3Cit .

No bubble-bitumen attachment occurred in 5 mM Na_3Cit solution with the maximum load force set to 20 nN, as shown in Figure 3-3A. The measured force showed strong repulsion during the bubble approach to the bitumen surface until the maximum loading force was reached. During

the retraction, the repulsive force decreased gradually, followed by a weak attraction which was caused by the hydrodynamic suction effect. The experimental data showed good agreement with the theoretical model when considering contributions of vdW, EDL, and HB forces to the disjoining pressure. From the SRYL fit, the minimum separation distance between the bubble and bitumen was approximately 13 nm, at which point the Laplace pressure inside the air bubble balanced the disjoining pressure. The contribution of each force to the disjoining pressure is plotted in Figure 3-3B. The Hamaker constant for air bubble and bitumen interacting across water was taken from the literature as -1.8×10^{-20} J, which led to a repulsive vdW force between the air bubble and bitumen.^{20,95} In 5 mM Na₃Cit, the Debye length was calculated to be 1.8 nm, and the zeta potentials of both the air bubble (see the Appendix A) and bitumen (Figure 3-2A) were negative. This resulted in a strong EDL repulsion between the air bubble and bitumen. The Stern potentials of the air/ water interface and bitumen/water interface were $\Psi_A = -65$ mV and $\Psi_B = -120$ mV, which were consistent with the experimental zeta potentials. The only attractive force between the air bubble and bitumen was determined to be the hydrophobic interaction as the contact angle of the air bubble on the bitumen surface was around 92°. ^{14, 25} However, in 5 mM Na₃Cit at pH 8.5, the hydrophobic force was too short ranged to trigger bubble-bitumen attachment, and the repulsive EDL force was still the dominant force.

The bitumen surface is highly charged due to the functional groups at the bitumen/water interface, which would make it seem bitumen should have a hydrophilic character. However, previous research found that the roughness of the bitumen surface increased in electrolyte solution, which was attribute to exposed hydrophobic sites.²⁰ Lin et al. and Drelich et al. found that the surface charge of bitumen varied significantly across the bitumen surface,^{89,90} which also indicated that the polar functional groups did not uniformly cover the bitumen surface. These studies suggest

that, although the bitumen surface is covered with charged functional groups, nonpolar groups (such as those in asphaltene) also exist at the bitumen/water interface and contribute to the hydrophobic behavior of bitumen.

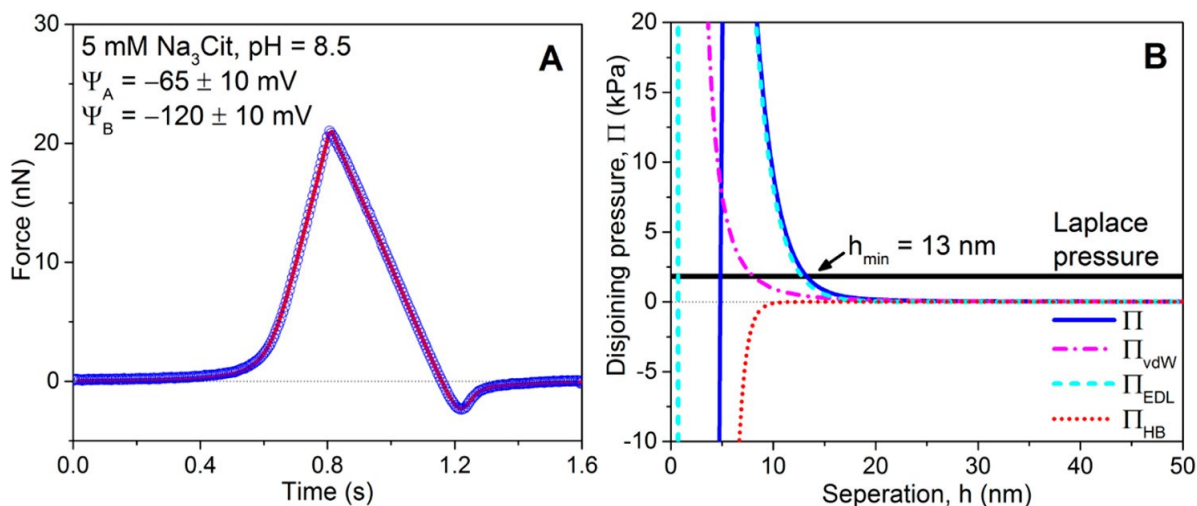


Figure 3-3 (A) Comparison of experimental interaction force and theoretical calculation between the air bubble and bitumen surface in 5 mM Na₃Cit. Blue circles represent experimental data while the red line represents the theoretical calculation. (B) Calculated disjoining pressure contribution in 5 mM Na₃Cit. The force measurements were conducted at pH = 8.5, and the bubble approach velocity was $V = 1 \mu\text{m/s}$. The bubble radius was $R = 80 \mu\text{m}$.

3.3.2.2 NaCl

Figure 3-4 shows the interaction between the bubble and bitumen at different NaCl concentrations at pH 8.5. No attachment was found in 10 mM NaCl solution up to 20 nN loading force, as shown in Figure 3-4A. The zeta potential of the bitumen droplet in 10 mM NaCl at pH 8.5 was measured to be -65 ± 7 mV. The Stern potentials of the air/water interface and bitumen/water interface were -45 and -72 mV, respectively, which were consistent with the experimental data (see the Appendix A for the bubble zeta potential). Conversely, the force curve

obtained in 15 mM NaCl showed a slightly repulsive force when the bubble approached the bitumen surface, followed by a sudden “jumpin” when the measured force reached ~6 nN, as shown in Figure 3-4B, which indicated the attachment of the bubble to the bitumen surface.

The overall disjoining pressure in 10 and 15 mM NaCl is shown in Figure 3-4C. The disjoining pressure in 10 mM NaCl solution exceeded the Laplace pressure. The air bubble could not move closer to the bitumen surface than 17 nm, at which point the Laplace pressure inside the air bubble balanced the disjoining pressure. However, in 15 mM NaCl, the disjoining pressure between air bubble and bitumen surface never exceeded the Laplace pressure, and the thin water film ruptured at the point when jump-in happened. The critical film thickness of rupture was calculated to be around 10 nm (see the Appendix A for the contribution from each force). Compared to 10 mM NaCl, the ionic strength of 15 mM NaCl is greater, which decreases the Debye length and the distance at which the EDL force becomes important. In 15 mM NaCl, the Debye length is decreased enough to allow the hydrophobic attraction to dominate and induce bubble-bitumen attachment. The decay length of the hydrophobic force was calculated to be around 1.08 nm, which was consistent with the hydrophobic decay length reported in the literature.²⁰

A 15 mM NaCl solution has roughly the same free Na⁺ concentration and about half the ionic strength of a 5 mM Na₃Cit solution. Thus, bubble-bitumen attachment happened at lower ionic strength in NaCl solution even though the sodium ion concentrations were the same for these two cases. The observed stability in 5 mM Na₃Cit is likely due to the strong negatively charged bitumen surface in the presence of citrate leading to a much stronger EDL repulsion at a separation around 10 nm, which prevents bubble-bitumen attachment.

3.3.2.3 CaCl₂

Different cations, including monovalent (Na⁺, K⁺) and divalent (Ca²⁺, Mg²⁺) ions, are always present in process water during oil sand extraction. Divalent cations were found to strongly influence bitumen aeration.^{6,9,62} In order to understand the effect of divalent ion on the interaction between the air bubble and bitumen, AFM force curves were obtained using a bubble probe in CaCl₂ at pH 8.5, as shown in Figure 3-5. Strong repulsion between the bubble and bitumen was found in 3 mM CaCl₂ solution, as shown in Figure 3-5A. The fitted Stern potentials of the air bubble and bitumen were -30 ± 5 and -40 ± 5 mV, respectively, the latter being consistent with the zeta potential of bitumen droplets from experimental measurements (-43 ± 3 mV). Fits of the experimental data to the SRYL model showed the EDL repulsion controlled the overall disjoining pressure, exceeding the Laplace pressure and preventing the rupture of the water film between the air bubble and the bitumen surface, as shown in Figure 3-5C. The calculated confined water film thickness of 15 nm between the air bubble and bitumen surface in 3 mM CaCl₂ was slightly thinner than in 10 mM NaCl, even though the ionic strength was lower. This was due to the reduced EDL repulsion force between the air bubble and bitumen surface in 3 mM CaCl₂ solution (see the Appendix A) from the reduced bitumen zeta potential (Figure 3-2A)

The jump-in behavior observed in 15 mM NaCl was also found in 4 mM CaCl₂, as shown in Figure 3-5B, but it occurred at a lower ionic strength in the presence of Ca²⁺. The reduced EDL repulsion allowed the hydrophobic attraction to become dominant at a separation distance of approximately 10 nm (Figure A8). Therefore, the overall disjoining pressure never exceeded the Laplace pressure, and the water film between the air bubble and the bitumen surface ruptured at a separation around 11 nm, as shown in Figure 3-5C.

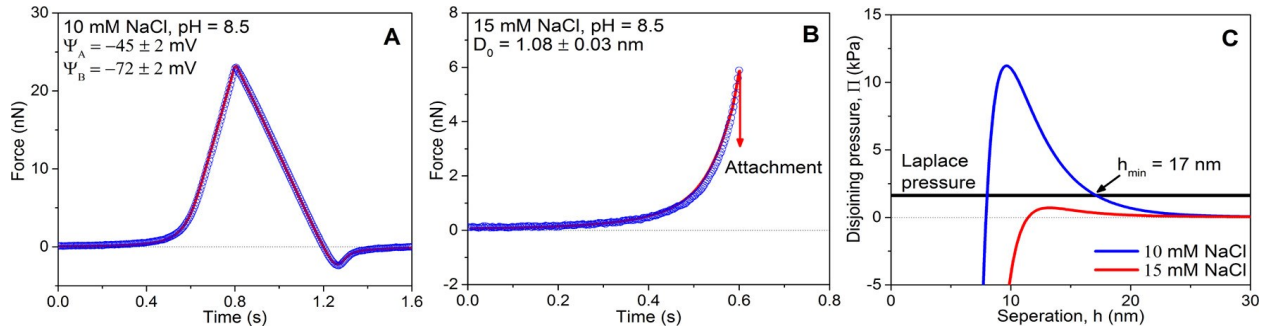


Figure 3-4 Interaction force between air bubble and bitumen surface versus time in (A) 10 mM NaCl and (B) 15 mM NaCl. Blue circles represent experimental data while the red lines represent the theoretical calculation. (C) Calculated disjoining pressures in 10 mM NaCl and 15 mM NaCl. The force measurement was conducted at pH = 8.5, and the bubble approach velocity was $V = 1 \mu\text{m/s}$. Experimental values used for SRYL fitting were $\gamma = 72.8 \text{ mN/m}$ for air/water interfacial tension and bubble radii of $R = 84 \mu\text{m}$ for 10 mM NaCl and $R = 85 \mu\text{m}$ for 15 mM NaCl.

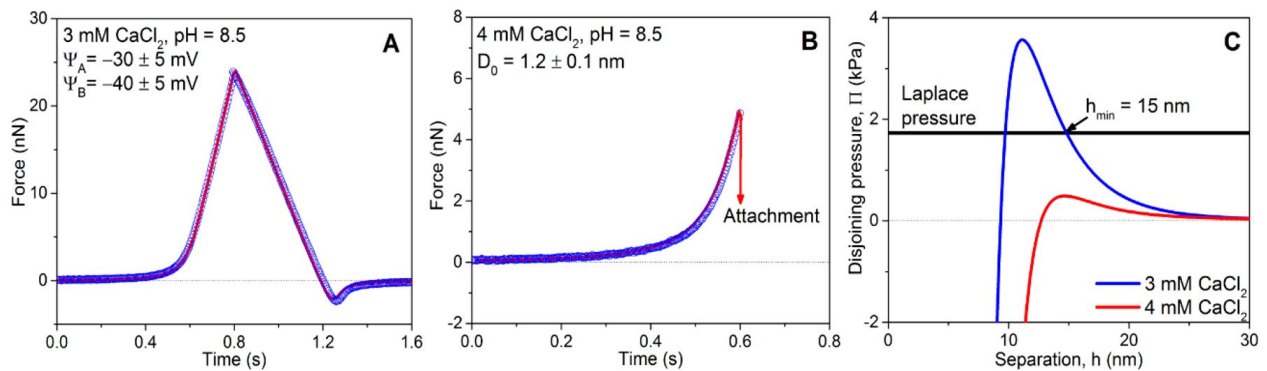


Figure 3-5 Comparison of experimental interaction force and theoretical calculation between the air bubble and bitumen surface in (A) 3 mM CaCl_2 and (B) 4 mM CaCl_2 . Blue circles represent experimental data while the red lines represent the theoretical calculation. (C) Calculated disjoining pressure in 3 and 4 mM CaCl_2 . The force measurements were conducted at

pH = 8.5, and the bubble approach velocity was $V = 1 \mu\text{m/s}$. The bubble radii were $R = 81 \mu\text{m}$ for 3 mM CaCl_2 and $R = 84 \mu\text{m}$ for 4 mM CaCl_2 .

3.3.2.4 Combined effect of Na_3Cit and CaCl_2 on bubble-bitumen interaction

Since citrate is a strong chelator of calcium and many other multivalent cations, the addition of Na_3Cit could significantly change the ionic makeup of process water. To study how citrate affects interaction forces between the bitumen and air bubble, various amounts of Na_3Cit were added in 4 mM CaCl_2 , which was the lowest CaCl_2 concentration that triggered bubble-bitumen attachment in this study. In the first set of experiments, 0.17, 2.3, and 4 mM Na_3Cit were separately added to 4 mM CaCl_2 solution, and the pH of the solution was fixed at 8.5. The interaction forces determined via AFM are shown in Figure 3-6. With the addition of 0.17 mM Na_3Cit , the aforementioned jump-in behavior occurred, as shown in Figure 3-6A. The air bubble attached onto the bitumen surface when the force reached about 6.8 nN. When the concentration of citrate was increased to 2.3 mM, the jump-in behavior disappeared, and the air bubble did not attach to the bitumen surface when the set force reached 20 nN, as shown in Figure 3-6B. However, when the Na_3Cit concentration was increased to 4 mM (Figure 3-6C), the jump-in behavior was again observed when the air bubble-bitumen interaction reached a load force of ~ 7.7 nN.

To understand this phenomenon, the EDL pressure and the overall disjoining pressure as a function of separation were calculated using the experimentally determined bitumen zeta potentials shown in Figure 3-2B. The calculated disjoining pressures are shown in Figure 3-7. Compared to 4 mM CaCl_2 with no added citrate, the addition of 0.17 mM Na_3Cit only slightly decreased the zeta potential from around -36 mV to around -40 mV, and the ionic strength remained the same. The EDL repulsion between the air bubble and the bitumen surface increased slightly, but it was not strong enough to balance the hydrophobic force and prevent bubble-bitumen attachment. When

the addition of Na₃Cit was increased to 2.3 mM, the magnitude of the zeta potential of the bitumen surface increased to approximately -55 mV. Due to chelation, the ionic strength, and thus EDL screening length, was approximately the same as the 4 mM CaCl₂ solution. The EDL repulsion, increased from the larger zeta potential magnitude, became strong enough to prevent bubble-bitumen attachment, as shown in Figure 3-7A. By increasing the concentration of Na₃Cit to 4 mM, the magnitude of the zeta potential of the bitumen surface increased further to approximately -70 mV. However, the ionic strength of the solution also increased from 12 mM to around 15 mM, which reduced the Debye length from 2.8 to 2.48 nm. The reduced influence distance of the EDL force into solution allowed the HB force to once again become the dominant force and induce bubble-bitumen attachment, as was seen for the 4 mM CaCl₂ + 0.17 mM Na₃Cit mixture.

The overall disjoining pressures of the three mixtures are shown in Figure 3-7B. The disjoining pressure of the solution in the copresence of 4 mM CaCl₂ and 2.3 mM Na₃Cit exceeded the Laplace pressure due to the strong EDL repulsion and stabilized the film at a thickness of around 14.5 nm. For the mixtures containing 0.17 mM Na₃Cit and 4 mM Na₃Cit, the slightly reduced zeta potential and the reduced Debye length, respectively, allowed the hydrophobic attraction to become dominant, thus reducing the overall disjoining pressure. The disjoining pressure of these two conditions never exceeded the Laplace pressure, which led to the bubble-bitumen attachment when the separation distance was approximately 10 nm. The previous experiments utilized mixtures of CaCl₂ and Na₃Cit so the Ca²⁺ ions were already chelated when the solution was introduced into the AFM cell. Another experiment was conducted to first immerse the spin-coated bitumen surface in 2.5 mL of 4 mM CaCl₂ solution for 15 min and then add 2.3 mM Na₃Cit for an additional 15 min to study whether similar results were achieved when the calcium ions were already adsorbed on the bitumen surface. The experimental result (Appendix A

Figure A9) also revealed nonattachment between the air bubble and bitumen surface at 20 nN maximum loading force. Agreement of the experimental results when citrate was added before and after loading of the bitumen surface with calcium suggests citrate can lead to stabilization of the air bubble and bitumen through a mechanism proposed by Wang et al.⁶⁴ Citrate would either desorb the Ca^{2+} or coadsorb with Ca^{2+} to block the subsequent attachment between the air bubble and bitumen.

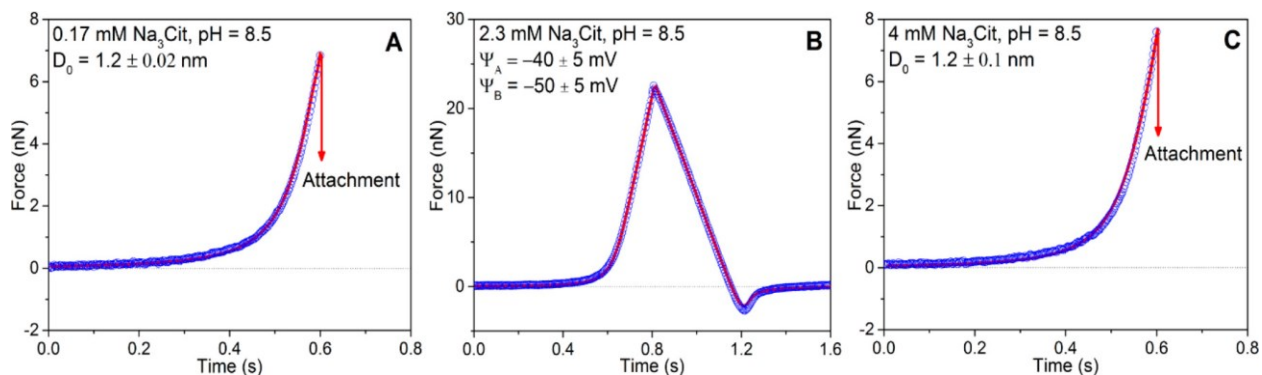


Figure 3-6 Comparison of experimental interaction force and theoretical calculation between the air bubble and bitumen surface in (A) 4 mM CaCl_2 + 0.17 mM Na_3Cit , (B) 4 mM CaCl_2 + 2.3 mM Na_3Cit , and (C) 4 mM CaCl_2 + 4 mM Na_3Cit . Blue circles represent experimental data while the red lines represent the theoretical calculation.

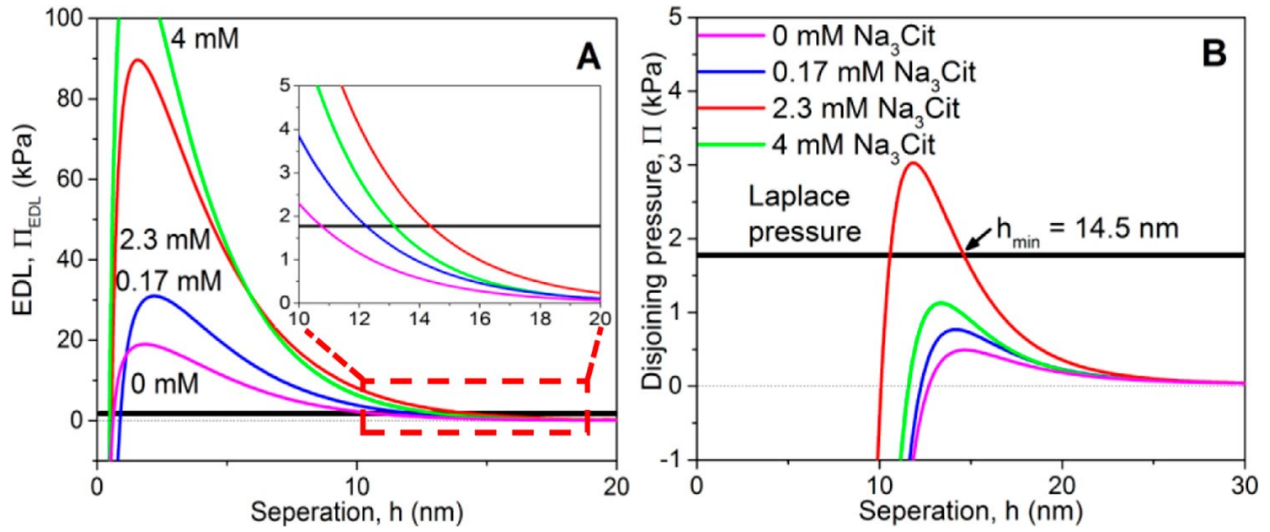


Figure 3-7(A) Calculated EDL pressure contribution to the overall disjoining pressure of one pure solution and three mixtures: 4 mM $CaCl_2$ + 0 mM Na_3Cit , 4 mM $CaCl_2$ + 0.17 mM Na_3Cit , 4 mM $CaCl_2$ + 2.3 mM Na_3Cit , and 4 mM $CaCl_2$ + 4 mM Na_3Cit . Inset: Zoom in of the red square. The axis labels of the inset are the same as that of (A). (B) Calculated overall disjoining pressure of the one pure solution and three mixtures: 4 mM $CaCl_2$ + 0 mM Na_3Cit , 4 mM $CaCl_2$ + 0.17 mM Na_3Cit , 4 mM $CaCl_2$ + 2.3 mM Na_3Cit , and 4 mM $CaCl_2$ + 4 mM Na_3Cit . The legend in (A) is the same as that in (B). The bubble radii of the pure solution and the three mixtures were $R = 84 \mu m$ for 0 mM Na_3Cit , $R = 85 \mu m$ for 0.17 mM Na_3Cit , $R = 78 \mu m$ for 2.3 mM Na_3Cit , and $R = 81 \mu m$ for 4 mM Na_3Cit .

3.3.3 Stability map

Based on the previous results, we performed a series of experiments to construct a stability map, which is plotted in Figure 3-8, representing the regions of attachment and nonattachment between the air bubble and the bitumen surface. Three parameters, including the $CaCl_2$ concentration, Na_3Cit concentration, and ionic strength, were considered, and all the experiments were conducted at pH 8.5. The nonattachment region represents stable interactions between the air

bubble and the bitumen surface when the load force reached 20 nN. The attachment region represents conditions in which the water film between the air bubble and bitumen surface ruptured and induced the air bubble to jump onto the bitumen surface. The bubble radii in this AFM study were within the range of 70-90 μm , and the bubble approach velocity was 1 $\mu\text{m/s}$. It is worth noting that the bubble radii in the actual oil sands extraction process are 0.25-1 mm, which is bigger than the bubble size used in this experiments.^{108,109} For systems involving larger bubble radii, the attachment region would somewhat shift to the right due to the decrease in the Laplace pressure. The darker shaded area between the dashed lines, estimated using the SRYL model, represents that either attachment or nonattachment could happen due to the variation of bubble radii. The region where calcium citrate tetrahydrate and calcium citrate hexahydrate are oversaturated was calculated via Visual MINTEQ. Values of log K_{sp} used for the tetrahydrate and hexahydrate forms were -17.81 ¹¹⁰ and -18.01 ,¹¹¹ respectively. Note that the K_{sp} value for calcium citrate hexahydrate was calculated from data published in the reference and assuming an association constant of log $K_{\text{c}} = 4.87$ for the CaCit^- complex, which is within the range of well accepted values. Based on the speciation calculations, no calcium citrate precipitate would form under all experimental conditions.

As seen in Figure 3-8, pure sodium citrate could prevent bubble-bitumen attachment even when the ionic strength was relatively high (around 30 mM). However, the copresence of CaCl_2 and Na_3Cit dramatically decreased the critical ionic strength that induced bubble-bitumen attachment from around 30 mM to around 20 mM. In addition, this critical ionic strength decreased with increasing CaCl_2 concentration. When the concentrations of both CaCl_2 (<3 mM) and Na_3Cit (<5 mM) were low, the low solution ionic strength and the long-range EDL repulsion always prevented bubble-bitumen attachment. At the critical point of 4 mM CaCl_2 , only a certain amount

of Na_3Cit prevented the bubble-bitumen attachment. When the CaCl_2 concentration exceeded 5 mM, bubble-bitumen attachment always happened. The stability map showed that pure Na_3Cit would significantly prevent the bubble-bitumen attachment, and zeta potential results indicate that this is due to a large zeta potential and associated EDL repulsion. However, in the presence of CaCl_2 and at high salinity, similar to oil sands processing water, adding sodium citrate had little effect on the bubble-bitumen attachment until the concentration of Na_3Cit approached that of CaCl_2 .

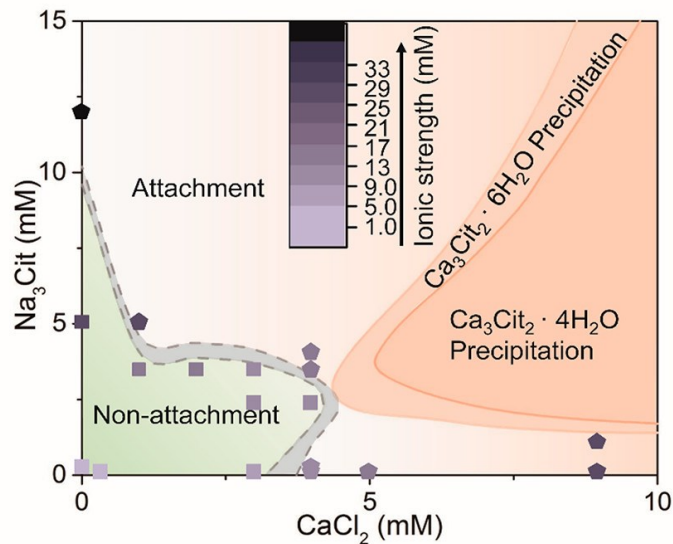


Figure 3-8 Stability map of the interaction between the air bubble and bitumen surface. All the experiments were conducted at pH 8.5. The shaded area separating the attachment and nonattachment regions was calculated using the SRYL model within experimental error.

3.4 Conclusions

In this study, we investigated the specific ion effects of Ca^{2+} and Cit^{3-} on the interaction between an air bubble and a bitumen-coated silica surface. A bubble probe AFM technique was employed to directly measure the interaction force between the air bubble and bitumen in a variety

of electrolyte types and concentrations. The SRYL model was applied to compare the experimental data with theory. In low-salinity solutions, the bitumen surface was strongly negatively charged, and the EDL repulsion prevented bubble-bitumen attachment. Increasing the solution salinity and increasing divalent ion concentration decreased the magnitude of the zeta potential of the bitumen droplet, reducing the EDL repulsion between the air bubble and bitumen and inducing bubble-bitumen attachment. Sodium citrate reduced the probability of bubble-bitumen attachment at a given ionic strength by making the bitumen surface more negatively charged. However, the stability map revealed that at high salinity, the copresence of Ca^{2+} and sodium citrate only had a little effect on the bubble-bitumen attachment, which was proved to be beneficial for the oil sand extraction process. This study provided valuable information on the effect of the secondary processing aid, sodium citrate, on the interaction forces between the air bubble and bitumen surface. In addition, this study showed that the SRYL model utilizing EDLVO theory can be used in conjunction with experimentally determined zeta potential data to predict what solution chemistries will be favorable for bubble-bitumen attachment and therefore for bitumen recovery by aeration.

**Chapter 4 Role of Sodium Citrate on the Zeta
Potential of Bitumen: Interactions between
Bitumen Metal Content and Ligands**

Abstract

Sodium citrate (Na_3Cit) has been proved to significantly increase the negative charges on bitumen surfaces, which enhances bitumen liberation and prevents slime coating. The citrate ion, which carries three negative charges with chelating ability, is expected to be related to the increased negative charges. Therefore, to understand the effect of Na_3Cit on the zeta potential of bitumen, experimental results were compared with sodium chloride (NaCl), EDTA, sodium phosphate (Na_2HPO_4), and sodium sulphate (Na_2SO_4). Similar to Na_3Cit , adding EDTA and Na_2HPO_4 resulted in a more negatively charged bitumen surface. However, increasing the concentration of Na_2SO_4 led to less negatively charged bitumen surfaces, a trend similar to NaCl .

To further understand the mechanism of how Na_3Cit , EDTA and Na_2HPO_4 change the zeta potential of bitumen surfaces, ICP-MS was used to analyze their ability to remove metal ions from bitumen to the aqueous phase. Meanwhile, QCM-D and FTIR were applied to study their adsorption on bitumen surfaces. A strong ability for Na_3Cit and EDTA to transfer metal cations from bitumen to the aqueous solution was observed. However, the concentration of metal ions released by Na_2HPO_4 was much smaller than expected. Moreover, all three anions could adsorb on the bitumen surface through mainly outer-sphere complexation and minor inner-sphere complexation. Our study proved that removing metal ions from bitumen and the adsorption onto the bitumen surface were the dominant reasons why chemicals such as Na_3Cit modified the zeta potential at the bitumen/water interface.

4.1 Introduction

The electrokinetic properties of bitumen/water interfaces are highly important in the sub-steps involved in the oil sands extraction process, indicating the magnitude of the repulsion in the colloidal system. It was reported that the more negatively charged bitumen surface decreases the adhesion and increases the long-range repulsive forces between bitumen and silica surface, facilitating the bitumen liberation.^{8,22,112} In addition, the increased surface charge at the bitumen/water interface could prevent the heterocoagulation between bitumen and clay particles, thus increasing the bitumen recovery and froth quality.²¹ However, it also increases the repulsive force between bitumen and air bubble, which could have a detrimental effect on the bitumen aeration.^{21,113}

In the traditional oil sands extraction process, sodium hydroxide (NaOH) is applied in process water to improve bitumen recovery.⁵⁷ It is believed that the organic acids and asphaltene contained in bitumen could transfer to the bitumen/water interface, and such a process can be promoted with the addition of NaOH.^{58,96,114} The deprotonation of the functional groups present in those surface-active components, i.e. carboxyl groups, is the origin of the negative charges on the bitumen/water interface.¹¹⁴ Recently, sodium citrate (Na₃Cit) has been successfully used in the oil sands extraction process as a secondary process aid combined with NaOH, significantly increasing the bitumen recovery and froth quality.¹¹⁵ One of the landmark contributions is that the combined addition of Na₃Cit and NaOH makes the bitumen/water interface more negatively charged than using NaOH alone.^{21,22,63} Surprisingly, the application of Na₃Cit had a minor effect on adjusting the solution pH, while it still increased the negative charges on bitumen/water interfaces.²²

The fundamental mechanism of Na_3Cit modifying the bitumen/water interface and affecting the zeta potential remains unknown. Based on the literature, several assumptions can be proposed.

Bitumen from oil sands contains a certain amount of metal ions such as Ca, Mg, Fe, Al, V, and so on.¹⁰¹ Metals can form bridging between different bitumen components through donor metal bridging and carboxylate group metal bridging.¹¹⁶ In this way, the metal ions could deactivate the polar groups on the bitumen/water interface and suppress the negative charges. The first assumption is that citrate is a strong chelating agent that could compete for those metal ions with the functional groups on the bitumen/water interface¹¹⁷ and transfer those metal ions into the aqueous phase, thus recovering the negative charges on functional groups and making bitumen surface more negatively charged.

Secondly, under the industrial operating pH, citrate is fully deprotonated and carry multiple negative charges. Citrate could possibly adsorb on the bitumen/water interface through metal ions with additional deprotonated carboxyl group facing the aqueous phase, thus making the bitumen zeta potential more negatively charged.

Another possible reason is that, according to the Hofmeister theory, the citrate ion is a stronger hydrated anion than chloride ion ($\text{Cit}^{3-} > \text{SO}_4^{2-} > \text{Cl}^-$), referred to as kosmotropes.¹¹⁸ According to the literature, the decrease in the absolute value of the zeta potential of some biomolecules or air/water interface would follow a reversed Hofmeister ion series.^{119,120} However, some divalent anions (i.e. SO_4^{2-}) would possibly have an inversed effect on the zeta potential due to its 2⁻ valence.¹²¹ In that case, citrate could probably make the bitumen/water interface more negatively charged than chloride since it carries three negative charges.

Our primary goal in this study is to understand the mechanism of Na₃Cit on modifying the zeta potential of the bitumen/water interface. Citrate is a well-known chelator carrying three negative charges that can form complex with most multivalent metal ions, which possibly influence the zeta potential of interfaces. To verify the dominant mechanism from the above theories and assumptions, four different sodium salts were selected to be compared to Na₃Cit. Ethylenediaminetetraacetate (EDTA) is a stronger chelating agent than Na₃Cit. Phosphate (PO₄³⁻) could form precipitates with several multivalent metal ions. Sulfate (SO₄²⁻) is a strongly hydrated multivalent anion referred to as kosmotropes, but rarely forms complexes or precipitates with multivalent metal ions. NaCl was chosen as a reference group to reflect the effect of Na ions. The zeta potentials of the bitumen/water interfaces for the selected salts were compared at a controlled solution pH. Furthermore, their ability to remove cations from bitumen and their adsorption on bitumen surfaces were analyzed to explain the mechanism of how citrate and other ligands modify the zeta potential of bitumen/water interfaces. Our study provides insights into the mechanism of how Na₃Cit changes the electrokinetic property of bitumen/water interfaces and directions on the future selection of chemical aids.

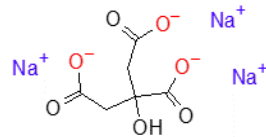
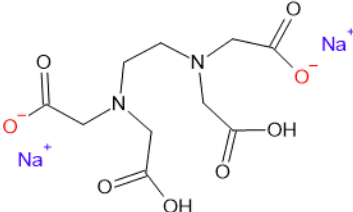
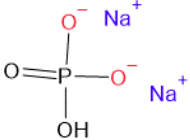
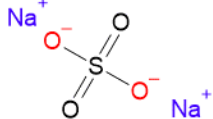
4.2 Materials and methods

4.2.1 Materials

Vacuum distillation unit (VDU) feed bitumen provided by Syncrude Canada Ltd was used in all experiments. Four different salts were selected to study their effect on the zeta potential of bitumen, including Na₃Cit, Ethylenediaminetetraacetic acid disodium salt dihydrate (EDTA-2Na), sodium phosphate dibasic (Na₂HPO₄) and sodium sulfate (Na₂SO₄). Their general details and chemical structure are listed in Table 4-1. Sodium chloride (NaCl) purchased from Alfa Aesar was

used as the control group. Sodium hydroxide solution (1 N, Fisher Scientific) and hydrochloric acid solution (1 N, Fisher Scientific) were applied to adjust the solution pHs. Octadecyltrichlorosilane (OTS) ($\geq 96\%$ purity, Sigma Aldrich) was used to hydrophobize the silicon wafers (NanoFAB, CA). Sodium dodecyl sulfate (SDS) ($\geq 90\%$ purity, Sigma Aldrich) was used to clean QCM-D accessories. Milli-Q water was used in all experiments throughout this study.

Table 4-1 Details of chemicals used in our experiments

Name	MW [g/mol]	Chemical structure	Source	Purity [%]
Na ₃ Cit	258		Fisher Scientific	>99.8
EDTA Ethylenediaminetetraacetic acid disodium salt	336.2		Sigma Aldrich	>99
Na ₂ HPO ₄ Sodium Phosphate	141.9		Fisher Scientific	>99.9
Na ₂ SO ₄ Sodium Sulfate	142		Sigma Aldrich	>99

4.2.2 Zeta potential measurement and metal content released from bitumen

A series of aqueous solutions containing chemicals listed in Table 4-1 were prepared from 0.1 mM to 10 mM, and the solution pH was adjusted to either 8.5 ± 0.1 or 10.5 ± 0.1 depending on the subsequent analysis. Figure 4-1 displays the procedures and conditions applied in bitumen zeta potential measurements and metal ions analysis.

For zeta potential measurements, 0.1 wt% of VDU feed bitumen was emulsified in 40 ml prepared solutions at pH 8.5 ± 0.1 using a Model 550 Sonic Dismembrator (70 Amplitude for 30 minutes). Since the acquired bitumen emulsions from the previous step were too concentrated to be tracked by the instrument, all emulsions were diluted 20 times with their corresponding aqueous solutions. The effect of selected salts on the zeta potentials of bitumen droplets was measured using a Brookhaven ZetaPALS. All the measurements were conducted at 22 °C, and the measured result was averaged from 10 runs (with 5 cycles for each run).

The metal content released from bitumen was examined at two pHs, using a fixed salt concentration of 5 mM. To extract the metal ions from bitumen, 0.5 wt% VDU feed bitumen was emulsified in a 40 ml prepared solution using the same method listed in the zeta potential analysis. The emulsions were first centrifuged at 5000 rpm to remove most of the oil. After that, the obtained supernatants were further filtered with 0.22 μm syringe filters. The metal content released to the aqueous solution was analyzed by Agilent 7900 Inductively Coupled Plasma-Mass Spectrometry (ICP-MS) with APHA method 3125B.¹²²

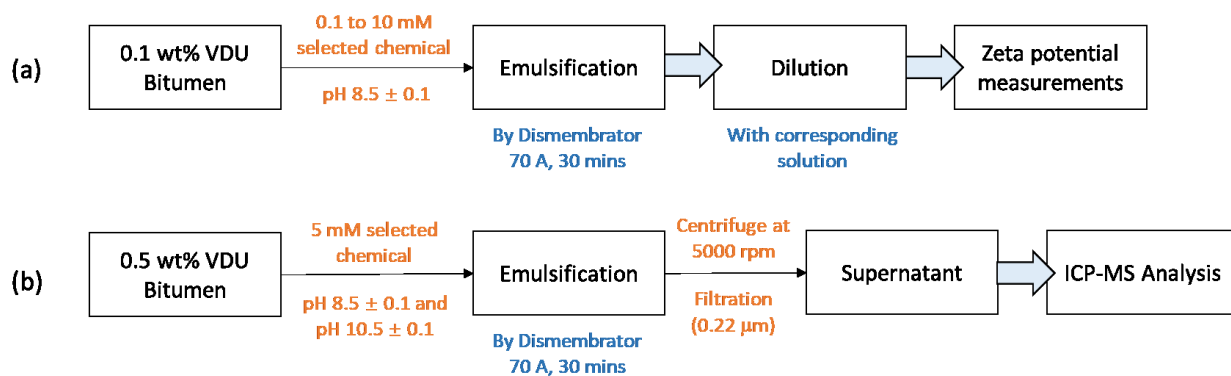


Figure 4-1 Illustration of experimental procedures: (a) zeta potential of bitumen droplets, (b) metal content released from the bitumen.

4.2.3 Adsorption measurements by QCM-D

The adsorption of various salts on the bitumen surface was performed with a QCM-D (E4 system, Biolin Scientific). The bitumen-coated hydrophobized silica sensors were prepared following the methods in our previous study.¹²³ Silica sensors were first sonicated in 2 wt% SDS solution for 30 mins and rinsed with Milli-Q water. Then, the sensors were dried with pure nitrogen gas and treated with UV/ozone for 10 mins. The cleaned silica sensors were hydrophobized by diluted OTS (0.1 vol% in toluene) for 60 s and dried with pure nitrogen gas. Spin coater (Laurell WS-400A-6NPP/Lite) was applied to prepare a uniform bitumen film. Five drops of solid-free diluted bitumen (5 wt% in toluene) were placed on the hydrophobized sensor surface during the coating process. The bitumen-coated sensors reached a contact angle around 88° and were used in the QCM-D adsorption experiment. The QCM-D flow modules and tubes were also cleaned with 2 wt% SDS solution and dried with nitrogen gas after rinsing with Milli-Q water.

A sequence of different liquids was pumped into QCM-D flow modules through a peristaltic pump at 100 μL/min. All measurements were started with Milli-Q water to establish a stable baseline, followed by the injection of sample solutions containing 25 mM of selected chemicals.

After the adsorption reached a plateau, a rinse cycle with Milli-Q water was applied to remove the loosely attached chemicals. All the solution pHs were adjusted to 8.5 ± 0.1 before performing the experiments with the temperature controlled at 22 °C. Both the viscoelastic model and the Sauerbrey equation were applied to calculate the mass adsorbed on bitumen surfaces through D-find software.

4.2.4 ATR-FTIR analysis for chemicals adsorption

A Nicolet 6700 Fourier Transform Infrared spectrometry equipped with attenuated total reflection (ATR-FTIR) was applied to confirm the adsorption of selected chemicals on bitumen surfaces. A thick layer of bitumen was placed on hydrophobized silica wafers (0.1 vol% OTS in toluene) and immersed in the sample solution containing 25 mM or 100 mM target chemicals for 1 hour. All the solution pHs were adjusted to 8.5 ± 0.1 before contacting with bitumen. Then, the bitumen surface was either dried with pure air or dried after rinsing with Milli-Q water to remove the loosely adsorbed chemicals. After that, the bitumen was pressed tightly against the ATR optical crystal. Due to the complexity of bitumen, all the spectra of adsorption on bitumen surfaces were normalized using OMNIC software. In detail, the spectrum of bitumen surface immersed in Milli-Q water was used as a control group and subtracted from the spectra of chemical adsorption on bitumen surfaces. To characterize the salts, aqueous solutions containing 100 mM of selected chemicals were dropped onto the crystal directly. In this case, the spectrum of Milli-Q water was applied as its control group and subtracted from the spectra of salt solutions. All the spectra were collected in a range from 4000 to 550 cm^{-1} , with 128 scans at a resolution of 4 cm^{-1} . The scan speed was set at 20 KHz with a 2 cm aperture, and the background was collected in air.

4.3 Results

4.3.1 Zeta potential of bitumen droplet in the presence of different sodium salts at pH 8.5

The zeta potential of bitumen droplets in different salt solutions as a function of their concentrations at $\text{pH } 8.5 \pm 0.1$ is plotted in Figure 4-2. The zeta potential of bitumen in NaCl and Na_3Cit solutions was replotted from data from Bai et al.²¹

It was observed that increasing the concentration of NaCl led to less negatively charged bitumen surfaces. This observation is consistent with previous studies in which the charge screening effect from Na^+ was responsible for the decreased magnitude of the zeta potential of the bitumen emulsion.^{97,124,125} The zeta potential was more negative in Na_3Cit , EDTA and Na_2HPO_4 solutions compared with NaCl in the tested concentration range. For Na_3Cit , the zeta potential had a valley at -130 mV (at 1 mM), which is around 30 mV lower than the NaCl at the same concentration. The group of Na_2HPO_4 showed very similar zeta potential values to that in Na_3Cit solutions from 0.1 mM to 0.5 mM. EDTA, as the best chelating agent among all the tested salts, generated the most negative bitumen zeta potentials. Both EDTA and Na_2HPO_4 reached their minimum zeta potential at around 0.5 mM, with -150 mV and -125 mV, respectively. Beyond this point, the zeta potential increased with increasing concentration due to the screening of the double layer by the Na^+ ions. Obviously, the anions that could form complexes or precipitates with the multivalent metal ions led to the more negatively charged bitumen surfaces at the same solution pH. Moreover, the stronger their chelating ability, the more they can increase the negative charges on bitumen surfaces.

Interestingly, adding Na_2SO_4 generated a similar trend as NaCl ; the zeta potential changed from around -100 mV to -65 mV when the concentration increased from 1 to 10 mM, despite that SO_4^{2-} is referred to as kosmotropes and carries multivalence. Its zeta potential behavior indicates that properties of multivalence kosmotropes are not the dominant mechanism for the increased negative charges at the bitumen/water interface.

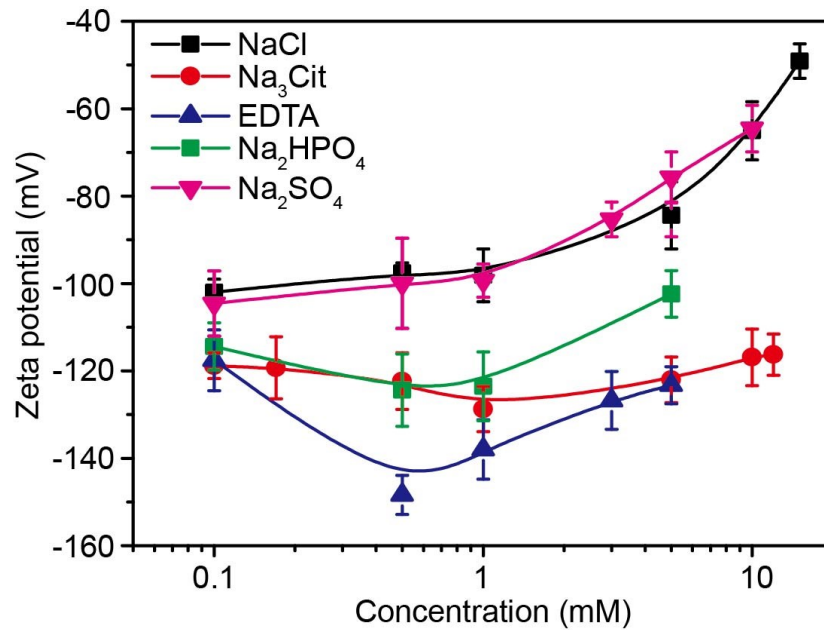


Figure 4-2 Bitumen zeta potential as a function of different salts concentration at pH 8.5.

4.3.2 Metal content released from bitumen

To examine the mechanism of increased negative charges on bitumen surfaces, the effect of different anions on extracting metal ions from bitumen to the aqueous solution was determined. According to the zeta potential results in Figure 4-2, only Na_3Cit , EDTA, and Na_2HPO_4 resulted in the more negatively charged bitumen surfaces. Therefore, these three salts were selected, and the results were compared with NaCl .

While making the bitumen emulsion in the aqueous solution, NaOH was added to adjust the pH to 8.5 and 10.5, promoting the release of natural surfactants and stabilizing the bitumen in water emulsion. The pHs of the prepared aqueous solution and their supernatant after extraction with bitumen are shown in Table 4-2. For the group of pH 8.5, the pH of Milli-Q water and NaCl solution barely changed after interacting with bitumen, and bitumen was hard to emulsify in these solutions. According to our observation, the presence of Na₃Cit, EDTA, and Na₂HPO₄ enhanced the emulsification, indicating that they promoted the release of natural surfactants from bitumen. However, the pH was slightly changed due to the buffer effect of these salts. At pH 10.5, the pH of all the extracted solutions was lower than the originally prepared solution, indicating that higher pH helps release organic acid and is beneficial for bitumen emulsification, which increases the chance for chelators to decompose the metal bridges. However, Na₃Cit showed a much lower pH than EDTA and Na₂HPO₄ because such pH is beyond its buffer range.

The ICP-MS results of some specific metal ions (Ca, Mg, Al, Mn, Cu, and V) at pH 8.5 and 10.5 are shown in Figures 4-3 and 4-4, respectively. Results of other metal ions are given in Table A2 in the Supporting Information. It is believed that the charge of bitumen surfaces is mainly related to the polar functional groups contained in resin and asphaltene.^{114,126} The naturally existing metal contents in bitumen could de-active and block the charges of those functional groups. Adding chelating agents during the emulsification process is expected to remove those metal contents from the functional groups and recover their charges. At pH 8.5 (Figure 4-3), the amount of metal ions released from bitumen to the aqueous solution was significantly higher in the presence of Na₃Cit and EDTA than in Milli-Q water or NaCl solution, especially for Ca, Al and Mn. As a stronger chelator, EDTA showed the best performance in extracting most of the metal ions, which could explain the most negative bitumen zeta potential among other solutions. Surprisingly, the

concentration of the released metal ions in the presence of phosphate was very small compared with the other salts, especially for Ca, Al, Mn, and Cu. This phenomenon is possibly because phosphate is easy to form precipitates with metal ions, and the precipitates were removed by filtration before ICP-MS analysis. At pH 10.5 (Figure 4-4), the concentrations of all the measured metal ions were much higher than those at pH 8.5. This result agrees with our observation of better emulsification at higher pH. In addition, the benefit from chelating agents is more obvious, especially for EDTA. For example, the concentration of released Ca in the presence of EDTA reached around 5 mg/L, which is about 0.125 mM. It was shown that the bitumen zeta potential can increase from -80 mV to around -40 mV in the presence of 0.1 mM CaCl₂.⁶³ Therefore, the released 5 mg/L Ca is enough to significantly modify the bitumen zeta potential.

Table 4-2 Solution pH of the extracted aqueous solution after making bitumen emulsion in different electrolyte solutions at pH 8.5 and 10.5.

pH before emulsification	Electrolyte	Concentration (mM)	pH of extracted aqueous solution
8.5 ± 0.1	Milli-Q	-	8.52
	NaCl	10	8.56
	Na ₃ Cit	5	8
	EDTA	5	8.10
	Na ₂ HPO ₄	5	8.5
10.5 ± 0.1	Milli-Q	-	8.87
	NaCl	10	6.99
	Na ₃ Cit	5	7.88
	EDTA	5	10.00
	Na ₂ HPO ₄	5	9.06

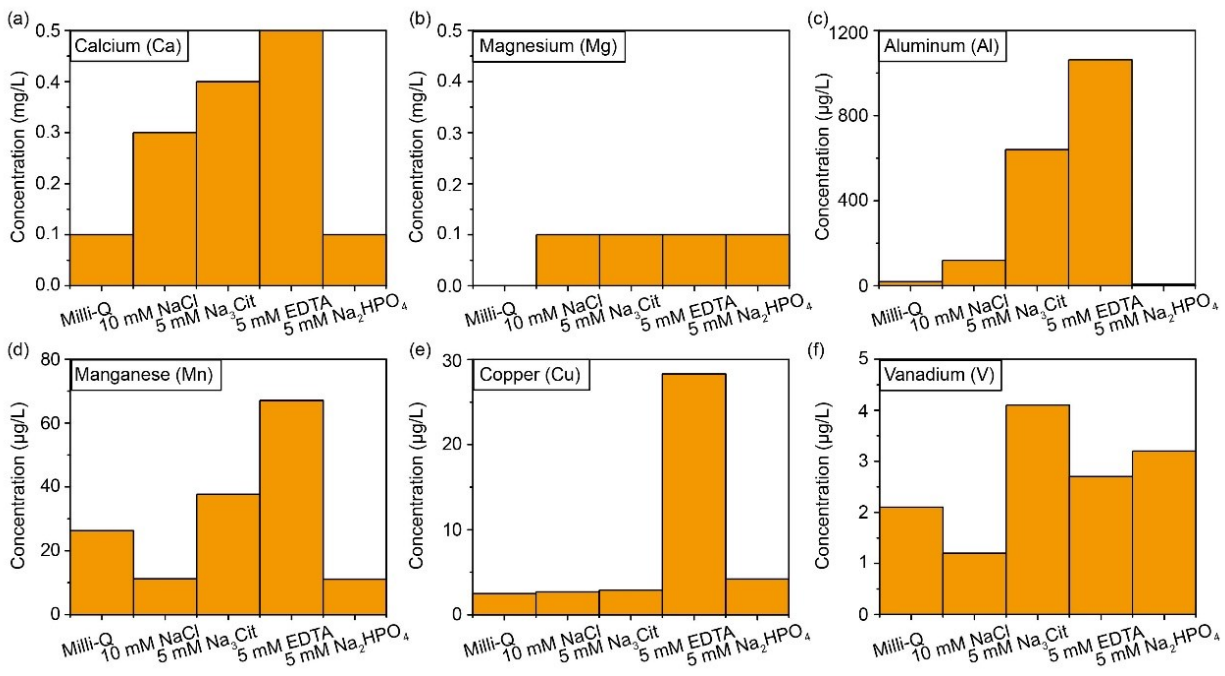


Figure 4-3 Concentration of metal ions released from bitumen to the aqueous solution in the presence of different salts at pH 8.5: (a) Ca, (b) Mg, (c) Al, (d) Mn, (e) Cu, (f) V.

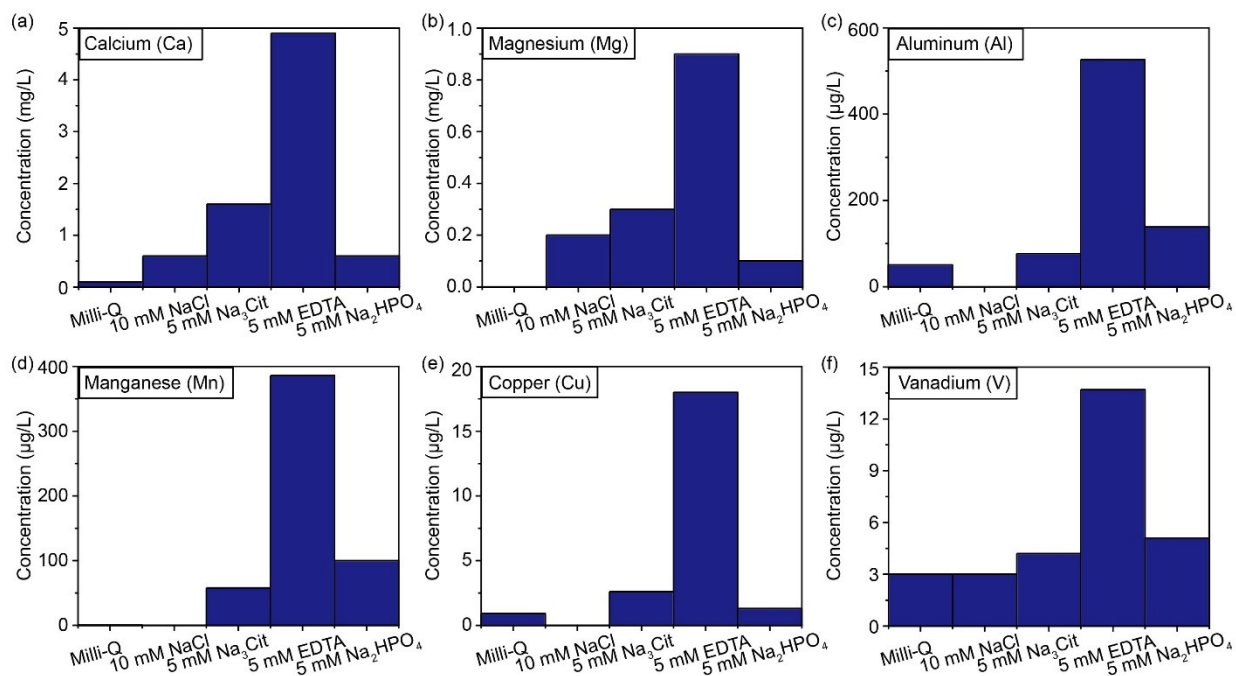


Figure 4-4 Concentration of metal ions released from bitumen to the aqueous solution in the presence of different salts at pH 10.5: (a) Ca, (b) Mg, (c) Al, (d) Mn, (e) Cu, (f) V.

4.3.3 QCM-D analysis of adsorption on bitumen surfaces

Apart from removing metal ions from bitumen, the adsorption of anions on bitumen surfaces could be another possible mechanism that modify the zeta potential. Similar to the previous section, Na₃Cit, EDTA and Na₂HPO₄ were selected to analyze their adsorption on bitumen surfaces using QCM-D. The adsorption of NaCl was also analyzed for comparison. A decrease in frequency indicates an increase of mass on the sensor surfaces and vice versa, while the dissipation signal represents the viscoelastic property of adsorbed materials. Selected QCM-D results of frequency and dissipation changes at the 3rd, 5th and 7th overtones are plotted versus time in Figure 4-5. It is worth mentioning that a signal drift (< 1 Hz/min) in frequencies was observed for all tests at all overtones, possibly resulting from the release of water-soluble species from the coated bitumen layer to the aqueous phase.

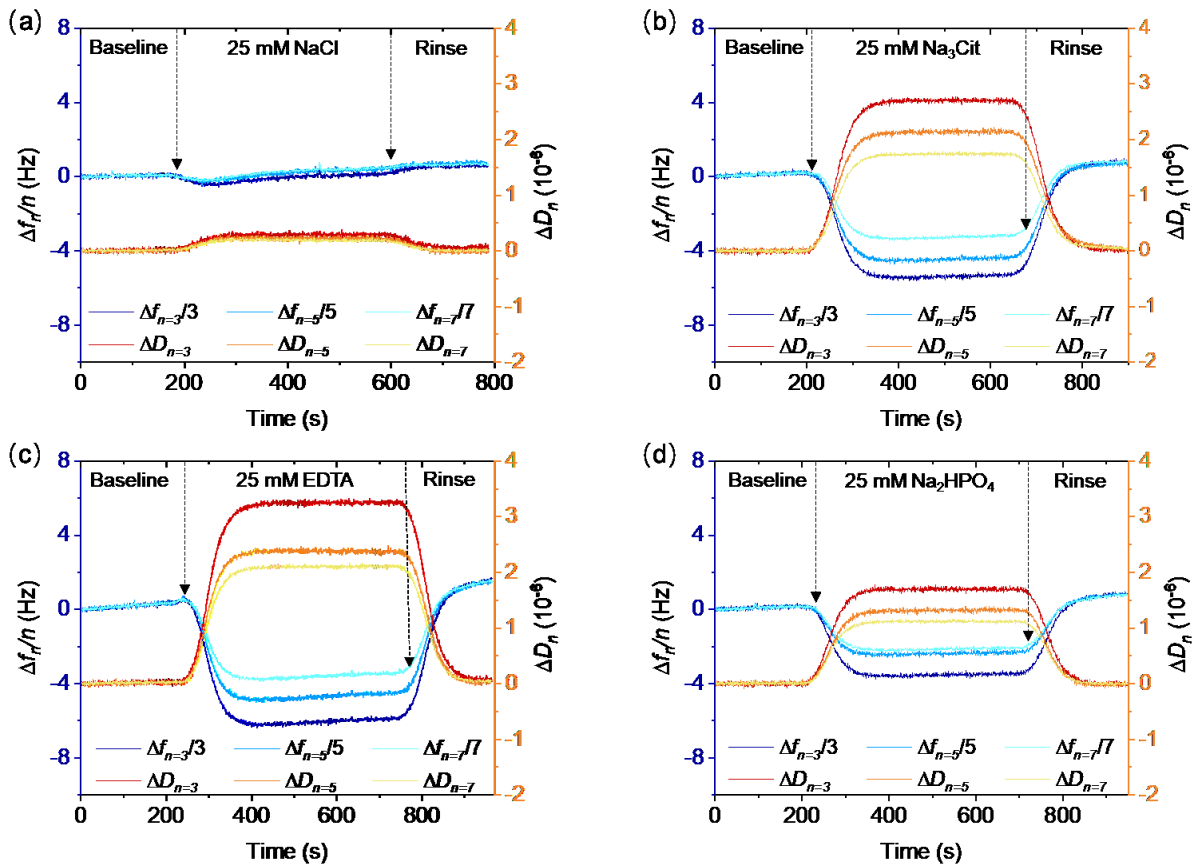


Figure 4-5 Change in frequency (Δf) and dissipation (ΔD) at 3, 5 and 7 overtones of the bitumen coated sensor under (a) 25 mM NaCl, (b) 25 mM Na_3Cit , (c) 25 mM EDTA, (d) 25 mM Na_2HPO_4 at pH 8.5.

The changes of frequencies (Δf) and dissipations (ΔD) responded differently with different salts, even though the same concentration and solution pH were used. In Figure 4-5a, negligible Δf and ΔD were observed for the injection of NaCl solution, indicating trace amounts of mass adsorbed on bitumen surfaces. The presence of 25 mM Na_3Cit or EDTA led to similar adsorption patterns (Figure 4-5b and 4-5c), with frequency dropping to around -6 Hz and dissipation significantly increasing after injection of sample solutions. This dissipation variations were likely caused by the adsorption of EDTA and citrate anions on the bitumen surfaces since both have

larger and more flexible molecular structures compared to either Na^+ or Cl^- . The presence of Na_2HPO_4 moderately decreased the frequency to around -4 Hz, as shown in Figure 4-5d. It was interesting to find that the dissipation signal switched back to its initial value and the frequency increased back to around zero (the signal drifts result in $\Delta f > 0$) after rinse cycle, indicating a reversible adsorption process for all scenarios. Therefore, only the period of injection chelating agents was applied to calculate the mass adsorbed on bitumen surfaces for all cases. With the consideration of solution density and viscosity, both Sauerbrey relation (Δm_s at the 3rd overtone) and the viscoelastic model (Δm_v) were used to calculate the mass, and the average values are summarized in Table 4-3. The Sauerbrey equation is only applicable for rigid and evenly distributed adsorption. In the measurements of Na_3Cit , EDTA and Na_2HPO_4 , the variations of dissipation were significant ($\Delta D/\Delta f > \sim 0.1 \times 10^{-6}$) and clear separations in different overtones were observed. Therefore, the Sauerbrey equation is not valid for those results. According to the Δf in Figure 4-5, it is reasonable to find that EDTA showed the highest adsorbed mass on bitumen surfaces, Na_3Cit ranked second. This trend is consistent with the zeta potential, as shown in Figure 4-2. However, for Na_2HPO_4 , only a small amount of mass was obtained from the calculation. In this study, we are unable to compare the adsorbed number density on the bitumen surfaces without considering their adsorption configuration and molecular weight, and such investigation is beyond our scope.

Table 4-3 Calculated mass deposition on bitumen surfaces pH 8.5.

Average Mass	NaCl	Na ₃ Cit	EDTA	Na ₂ HPO ₄
$\Delta m_{S(n=3)}$, ng/cm ²	12.5	42	26	9.5
Δm_V , ng/cm ²	23.5	164	230.5	35.5

4.3.4 ATR-FTIR analysis for chemicals adsorption

The ATR-FTIR spectroscopic investigation is aimed to further confirm the adsorption of Na₃Cit, EDTA and Na₂HPO₄ on bitumen surfaces and seek useful information about the anion-bitumen surface complexes. The spectra of bitumen after immersion in Milli-Q water are shown in Figure A10 in the Supporting Information, and the functional groups found in our experiment are consistent with the literature,¹²⁷ as given in Table A3. To clarify the adsorption, the normalized spectra in these cases (with and without rinsing) were compared with the spectra of pure electrolyte solution.

The spectrum of Na₃Cit solution at pH 8.5, in which the citrate species are fully deprotonated, is shown in Figure 4-6a. The fully deprotonated Na₃Cit solution has adsorption bands at 1569 cm⁻¹, 1390 cm⁻¹, and weaker adsorption at 1279 cm⁻¹, which are consistent with the reported values.¹²⁸ The first two bands correspond to the asymmetric and symmetric C-O stretching, while the weaker bond probably results from the carboxylate bending vibration. For the bitumen, after it was immersed in 25 mM Na₃Cit solution (Figure 4-6b), the asymmetric C-O band shifted to 1577 cm⁻¹ compared to 1569 cm⁻¹ observed in Na₃Cit aqueous, representing that citrate formed outer-sphere complexes on bitumen surfaces (i.e. through H-bonding or electrostatic interactions). In addition,

a weak peak formed at 1602 cm^{-1} , which could be considered as the asymmetric C-O vibration from the inner-sphere complex (i.e. direct interaction with metal ions) formed by the adsorption of Na_3Cit . For the case without rinsing, the Δ value ($\Delta = \nu_{as}\text{CO}_2^- - \nu_{sym}\text{CO}_2^-$) increased to 183 cm^{-1} comparing to 179 cm^{-1} in Na_3Cit aqueous solution, also proved the complexation of Na_3Cit on the bitumen surface.¹²⁹ After rinsing with Milli-Q water, as shown in Figure 4-6c, the intensity of the peak at 1577 cm^{-1} became much weaker, showing that the formation of outer-sphere complexes was reversible and could be washed off by Milli-Q water. This is consistent with the result from the QCMD experiments. The asymmetric C-O band at 1602 cm^{-1} representing the inner-sphere complex can still be found after rinsing with Milli-Q water. However, such adsorption is too weak to be captured by the QCMD experiments due to the signal drift on frequencies caused by unstable bitumen film.

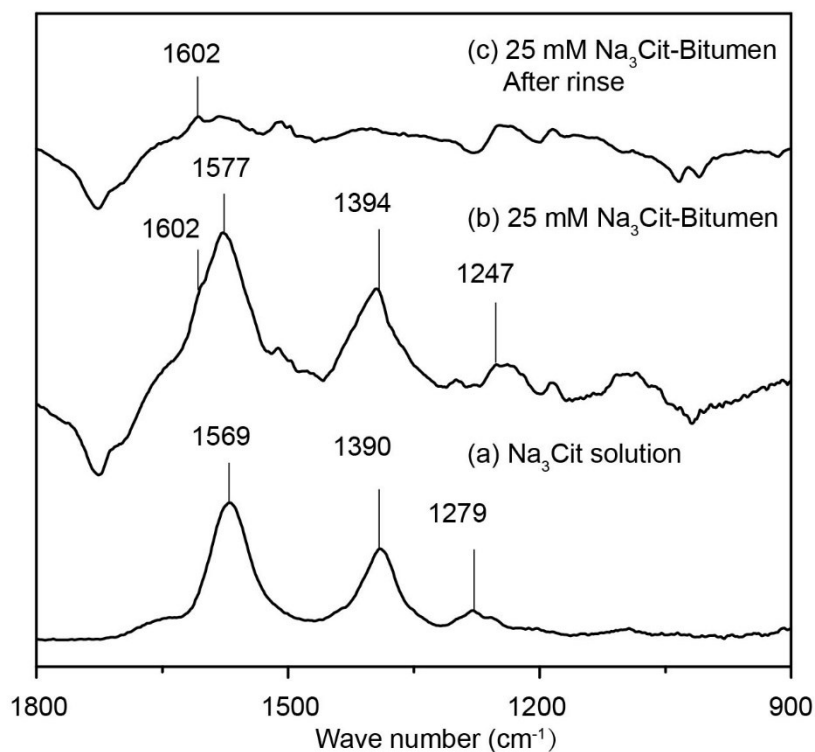


Figure 4-6 ATR-FTIR spectra of: (a) Na₃Cit solution at pH 8.5, (b) normalized bitumen immersed in 100 mM Na₃Cit solution at pH 8.5 and (c) normalized bitumen immersed in 100 mM Na₃Cit solution at pH 8.5 and rinsed with Milli-Q water.

The spectrum of EDTA solution at pH 8.5 is shown in Figure 4-7a. Under this pH, EDTA is in trisodium form. The asymmetric and symmetric C-O stretching appear at 1576 and 1401 cm⁻¹, respectively. The C-N stretching was found at 1133 cm⁻¹ for the trisodium form, which is consistent with the literature.¹³⁰ The fingerprint region is usually difficult to assign for large molecules such as EDTA, and the summary of the other bands is given in Table A4. For the adsorption of 100 mM EDTA without rinsing on bitumen surfaces (Figure 4-7b), the asymmetric C-O vibration shifted from 1576 cm⁻¹ to 1585 and 1604 cm⁻¹. The band at 1585 cm⁻¹ represents the formation of the outer-sphere complexes, while the band at 1604 cm⁻¹ possibly indicates the inner-sphere complexation. The Δ value for trisodium EDTA solution was calculated at 175 cm⁻¹, which agreed with the reported average value. It changed to 179 cm⁻¹ for EDTA adsorption on bitumen, also representing the formation of complexes on bitumen surfaces.¹³⁰ After rinsing by Milli-Q water, asymmetric C-O vibration at 1604 cm⁻¹ was still captured (Figure 4-7c), representing that the formation of the inner-sphere complexes is irreversible adsorption. Meanwhile, the disappeared asymmetric C-O band at 1585 cm⁻¹ indicated the outer-sphere complexes were removed by rinsing.

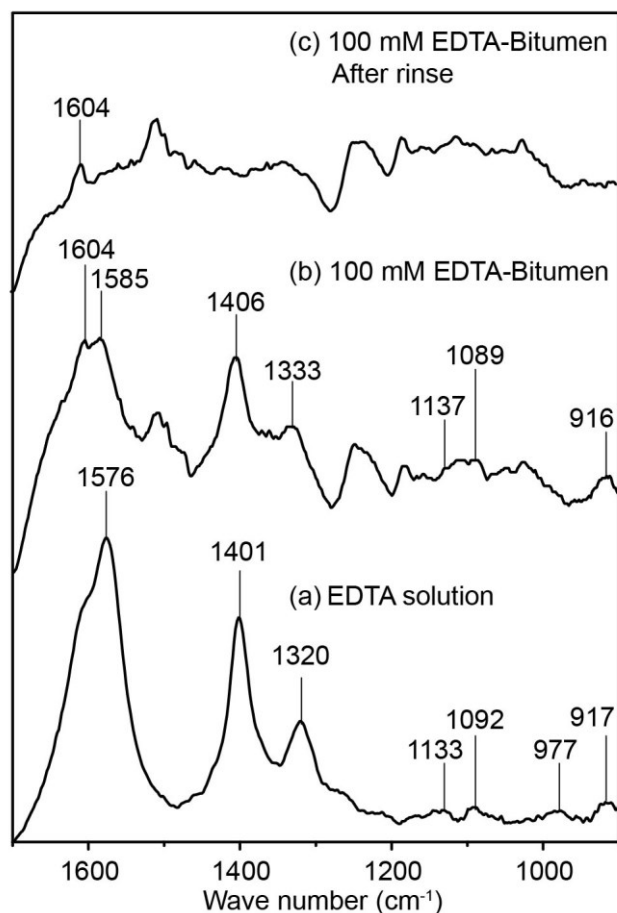


Figure 4-7 ATR-FTIR spectra of: (a) EDTA solution at pH 8.5, (b) normalized bitumen immersed in 100 mM EDTA solution at pH 8.5 and (c) normalized bitumen immersed in 100 mM EDTA solution at pH 8.5 and rinsed with Milli-Q water.

The spectrum of Na_2HPO_4 solution at pH 8.5 is shown in Figure 4-8a. At pH 8.5, the dominant species of phosphates is in monoprotonated type (HPO_4^{2-}) and has C_{3v} vibration with the ν_3 vibration splitting into two peaks at 1077 (E vibration) and 990 cm^{-1} (A_1 vibration). The ν_1 vibration is at 848 cm^{-1} , which is consistent with the literature.^{131,132} Figure 4-8b shows the normalized spectra of 100 mM Na_2HPO_4 adsorbed on bitumen without rinsing. The three main characteristic peaks at 1084, 986, and 833 cm^{-1} represent the two ν_3 vibrations and ν_1 vibration, respectively, which are similar to the characteristic bands of the phosphate solution at pH 8.5. If

monoprotonated phosphate forms an inner-sphere complex with metal ions, the symmetry of the surface complex would change from C_{3v} to C_{2v} , leading to three ν_3 bands in addition to ν_1 band¹³². As shown in Figure 4-8b, the peak at 1084 cm^{-1} becomes much wider with a shoulder appearing, and two new small peaks at 1179 and 1028 cm^{-1} , which could be explained by the splitting of ν_3 vibration of forming different inner-sphere metal-phosphate complexes. For the formation of outer-sphere complexes, a slight shift of the ν_3 vibrations is expected without changing the number of ν_3 bands¹³². Therefore, the slight increase of the E vibration and the decrease in the A_1 vibration could be related to the outer-sphere complexation of phosphate on bitumen surfaces. After rinsing with water, the high-intensity peaks at 1084 and 986 cm^{-1} disappear, representing the reversible adsorption of outer-sphere complexed phosphate (Figure 4-8c). However, the small peaks at 1184 , 1147 , 1087 , 1029 and 1003 cm^{-1} still appear, which could be the ν_3 vibration bands of different metal-phosphate inner sphere complexes.¹³¹

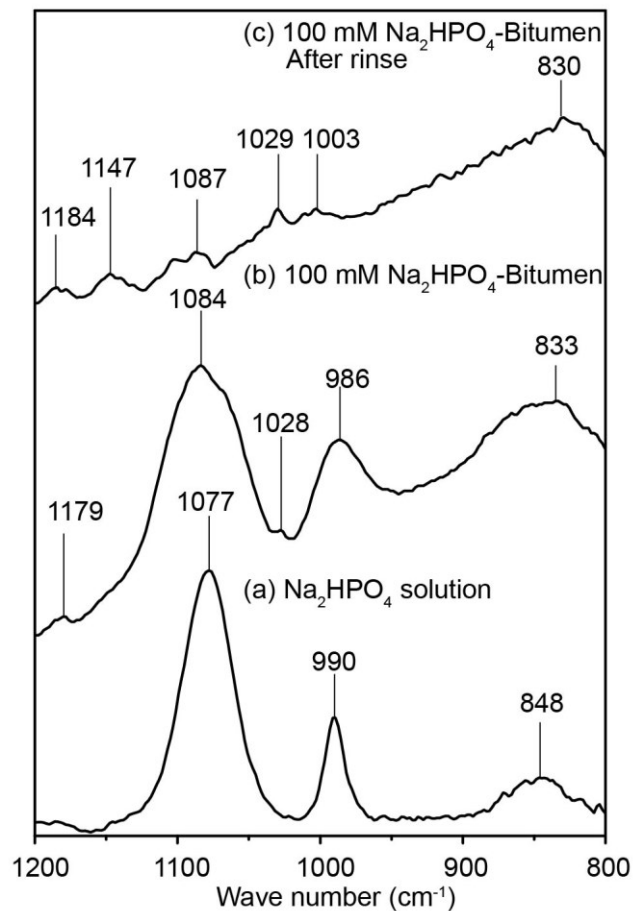


Figure 4-8 ATR-FTIR spectra of: (a) Phosphate solution at pH 8.5, (b) normalized bitumen immersed in 100 mM phosphate solution at pH 8.5 and (c) normalized bitumen immersed in 100 mM phosphate solution at pH 8.5 and rinsed with Milli-Q water.

4.4 Discussion

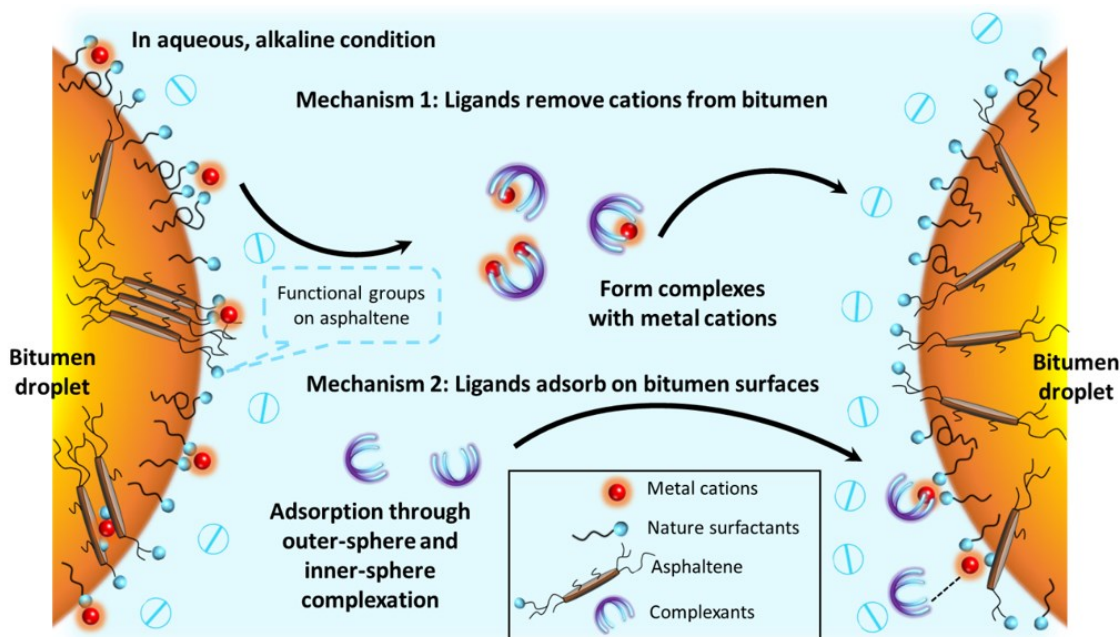


Figure 4-9 Mechanisms of complexants modifying the zeta potential of bitumen surfaces.

Based on the above results, mechanisms of chelators on modifying the zeta potential of bitumen surfaces were proposed as removing the metal contents from bitumen and adsorbing on bitumen surfaces, as illustrated in Figure 4-9. The zeta potential of bitumen surfaces comes from an overall effect from the naturally existing surface-active species, the metal contents in bitumen and the bulk solution chemistry. Metals are present as metal bridges that coordinate with organic compounds in bitumen, especially asphaltene and naphthenic acids.^{116,133} Increasing the slurry pH by adding NaOH contributes to the deprotonation of surface-active species, resulting in more negatively charged bitumen surfaces. However, the existence of metal ions potentially screens the negative charges from functional groups.

The first mechanism in Figure 4-9 describes that ligands, such as EDTA and Na₃Cit, can remove the metal bridges, which frees more functional groups contained in asphaltene and

naphthenic acids and recovers the surface charges of bitumen. The affinity of the complexants to metallic ions highly depends on their structures, especially the functional groups and their pK_a values.^{134,135} For most metallic ions, EDTA showed higher complexation strength than citrate since it contains more carboxyl groups that could form more stable complexes.¹³⁶ Therefore, it is reasonable to find that EDTA showed the best performance in releasing metal ions from bitumen. Even though much less metal content was detected in Na_2HPO_4 solution, it is expected that HPO_4^{2-} , the dominant anion under pH 8.5 and 10.5, can form low solubility salts with most metal ions.¹³⁷ Through such a mechanism, phosphate increased the negative charges on bitumen surfaces. Moreover, phosphate salts had been applied in lab-scale oil sands extraction experiments. Enhanced bitumen liberation and reduced interfacial tension of bitumen/water interface were observed with the application of phosphate, possibly related to its ability to form precipitates and complexes with metal ions.^{138,139}

The existence of metals inside bitumen also provides a chance for anions to adsorb on the bitumen/water interface, as described in mechanism 2 in Figure 4-9. Under the tested pH conditions, all the selected salts carry multiple negative charges, which potentially increase the negative charges on bitumen through adsorption. QCM-D measurements quantified the adsorption of the selected salts on bitumen surfaces, while ATR-FTIR provided bonding information of those ligands. Significant adsorption of EDTA and Na_3Cit on bitumen surfaces was confirmed by QCM-D, and both inner-sphere and outer-sphere complexation were identified from the ATR-FTIR measurements. It is worth mentioning that the observed intensities of inner-sphere complexes were very weak at pH 8.5, and the majority of adsorption was contributed from the reversible outer-sphere complexes. According to the literature, the adsorption of carboxylic acids on mineral surfaces is highly dependent on the pH and type of minerals.¹²⁹ For citric acid, the outer-sphere

complexation can be observed for a broad pH range, while inner-sphere complexation only dominates at acidic pH.^{128,140} However, the bitumen surface is different from the general mineral surfaces (i.e. metal oxides). Inner-sphere complexation is possibly caused by the direct coordination of ligands to the metal ions at the bitumen/water interface. Therefore, the asymmetric C-O vibration intensity from the inner-sphere complex was more obvious in EDTA than Na₃Cit because EDTA has a higher affinity to metal ions. The H-bonding and electrostatic interaction are assumed to be the main reason for outer-sphere complexation. Besides, metal complexes (i.e., released metal content form complexes with ligands in solution) could behave like ligands and adsorb on mineral surfaces to modify the surface charges.¹⁴¹ Those weakly bonded outer-sphere complexes are easily removed from the surfaces, which agreed with our QCM-D results that a rinse cycle removed almost all of the adsorption. The QCM-D results showed much less adsorbed HPO₄²⁻ than Na₃Cit and EDTA, while ATR-FTIR provided little evidence of HPO₄²⁻ adsorption on bitumen surfaces. Therefore, the mechanism for HPO₄²⁻ to change the zeta potential of bitumen surfaces is inconclusive and requires further analysis on the composition of precipitations in solution.

Obviously, SO₄²⁻ showed no effect on increasing the negative charges at the bitumen/water interface, which is consistent with the previous study that the kosmotropes could not modify the zeta potential of the oil-water interface.^{142,143} Therefore, the effect from the Hofmeister theory could be negligible. We believe that the reaction with the metal cations contained in bitumen is the crucial mechanism for citrate to modify the bitumen zeta potential.

4.5 Conclusion

Our study systematically investigated the mechanism of several sodium salts on modifying the bitumen/water zeta potential. We found that, similar to Na_3Cit , both EDTA and Na_2HPO_4 could make the zeta potential at the bitumen/water interface more negative compared with NaCl. As well-known chelators, EDTA and Na_3Cit have a higher tendency to transfer the metal ions from bitumen to the aqueous phase than other tested salts, which recovered the negative charges on surface-active components from bitumen. Meanwhile, both anions carried multiple negative charges and strongly adsorbed on bitumen surfaces through both outer-sphere and inner-sphere complexation. These processes potentially make the bitumen surface more negatively charged. As for Na_2HPO_4 , its ability to remove metal ions from bitumen remains unclear, and less adsorption on bitumen surfaces was observed. However, the ATR-FTIR results proved metal-phosphate complexes formed on bitumen surfaces, which also confirmed the effect of adsorption on varying the zeta potential of bitumen.

On the other hand, increasing the concentration of Na_2SO_4 reduced the negative charges on the bitumen/water interface, similar to the effect of NaCl. Thus, the effect of Hofmeister theory on the zeta potential was negligible in our study. The interactions between ligands and metal content from bitumen were the dominant mechanism for modifying the zeta potential at the bitumen/water interface.

**Chapter 5 Water Film Drainage between a Very
Viscous Oil Drop and a Mica Surface**

Abstract

We investigate thin film drainage between a viscous oil drop and a mica surface, clearly illustrating the competing effects of Laplace pressure and viscous normal stress (τ_v) in the drop. τ_v dominates the initial stage of drainage, leading to dimple formation (h_d) at a smaller critical thickness with an increase in the drop viscosity (the dimple is the inversion of curvature of the drop in the film region). Surface forces and interfacial tension control the last stage of film drainage. A scaling analysis shows that h_d is a function of the drop size R and the capillary numbers of the film (Ca_f) and drop (Ca_d), which we estimate by $h_d = 0.5R\sqrt{Ca_f/(1 + 2Ca_d)}$. This equation clearly indicates that the drop viscosity needs to be considered when $Ca_d > 0.1$. These results have implications for industrial systems where very viscous liquids are involved, for example, in 3D printing and heavy oil extraction process.

5.1 Introduction

The film drainage process between an oil drop or air bubble and solid surfaces is of great importance in many industrial applications, including heavy oil extraction and 3D printing. This is particularly true for heavy oils or fluids of ultrahigh viscosity, which is a crucial property of bitumen and some polymers applied in 3D printing. As a drop approaches a solid surface in an aqueous phase, an inversion of the curvature of the aqueous film appears at some stage, which is called “dimple formation”.¹⁴⁴ Such a dimple may lead to the capture of small water drops and air bubbles, which is detrimental for 3D printing technology.^{145,146} The Stokes–Reynolds–Young–Laplace model¹⁵ is well established to predict film drainage between an oil drop of relative low viscosity (< 0.1 Pa·s) and a solid surface. A wide range of capillary numbers of the water film ($Ca_f = \mu_w V / \gamma$, where μ_w is the viscosity of water, V is the approach velocity, and γ is the oil-water interfacial tension) ranging from $Ca_f = 10^{-8}$ to 10^{-2} has been investigated and a universal relation for the height of initial dimple formation has been established, which can be expressed as $h_d \sim R \sqrt{Ca_f}$, where R is the radius of the drop.^{16,19,50,147} Increasing the approach velocity and decreasing the oil-water or air-water interfacial tension^{16,19} was found to affect the height of the dimple occurrence. However, the effect of the capillary number of the oil drop ($Ca_d = \mu_o V / \gamma$, with μ_o being the viscosity of oil) on the film drainage process received little attention. Langley et al.^{148,149} studied the impact of an ultraviscous drop on solid and water surfaces in air. The initial dimple was scaled by an empirical impact parameter that resulted in a relationship of $h_d \sim \mu_o^{-\frac{1}{9}}$. Some axisymmetric models for the coalescence between two ultraviscous drops or a drop against a solid surface have also been developed. The tangential immobile boundary condition was shown to be applicable at the oil-water interface for the systems with high oil-water viscosity ratio (μ_o / μ_w).¹⁵⁰ In addition, some numerical models were developed to calculate the

drop profile and lubrication force under the assumption of constant approach velocity or constant interaction force.^{151,152} However, the viscosity ratio considered in those models was still not high enough for the viscous stress to play a role in the drop deformation. Such subject therefore remains to be addressed.

In this thesis, we report the drainage of the thin liquid water film between an oil drop of ultrahigh viscosity and a mica surface using high-speed interferometric images that can provide quantitative information throughout the whole film drainage process. The capillary number of the oil drop Ca_d in this study ranged from 10^{-8} to 30 using drops of viscosity ranging from ~ 0.001 to ~ 100 Pa·s. The capillary number of the aqueous film Ca_f ranged from 10^{-7} to 10^{-4} . The height of dimple occurrence was precisely obtained by analyzing the interference fringes. Using scaling arguments, we derived an analytical formula that can accurately predict the dimple height over a wide range of drop capillary numbers, which requires one to take the viscous normal stress inside the oil drop into consideration. We observed a substantially different film drainage process, which was likely caused by the competition between the Laplace pressure and the viscous normal stress across the surface.

5.2 Experimental section

The drainage of the aqueous film between highly viscous drops and a surface was studied using the dynamic force apparatus (DFA). A schematic of the DFA is shown in Fig. 5-1(a).¹⁶ An oil drop with radius $R = 1.05 \pm 0.01$ mm was generated at the end of a capillary tube. The mica surface was freshly cleaved before its use to obtain a hydrophilic surface with the water contact angle of $\sim 0^\circ$. The initial distance between the oil drop and the mica surface was set at 350 μm , which was monitored and controlled by a side view camera. By using the motorized actuator, the oil drop was driven toward to mica surface for 500 μm , which we termed “displacement,” so that

interaction happens, and the oil drop will form a dimple, as seen in the schematic of Fig. 5-1(b). The drop approach velocities were selected from 0.1 to 10 mm/s.

The interference fringes were observed by an inverted Axiovert 100 Carl Zeiss microscope and were recorded by a high-speed video camera (Photron SA4, 60–500 000 frames/s). Figure 5-1c shows an example of the interference fringes between a drop of 25.8 Pa·s viscosity interacting with the mica surface. The film thickness as a function of radial coordinate was obtained by analyzing the fringes using the method adopted by Scheludko and Platikanov.³⁶

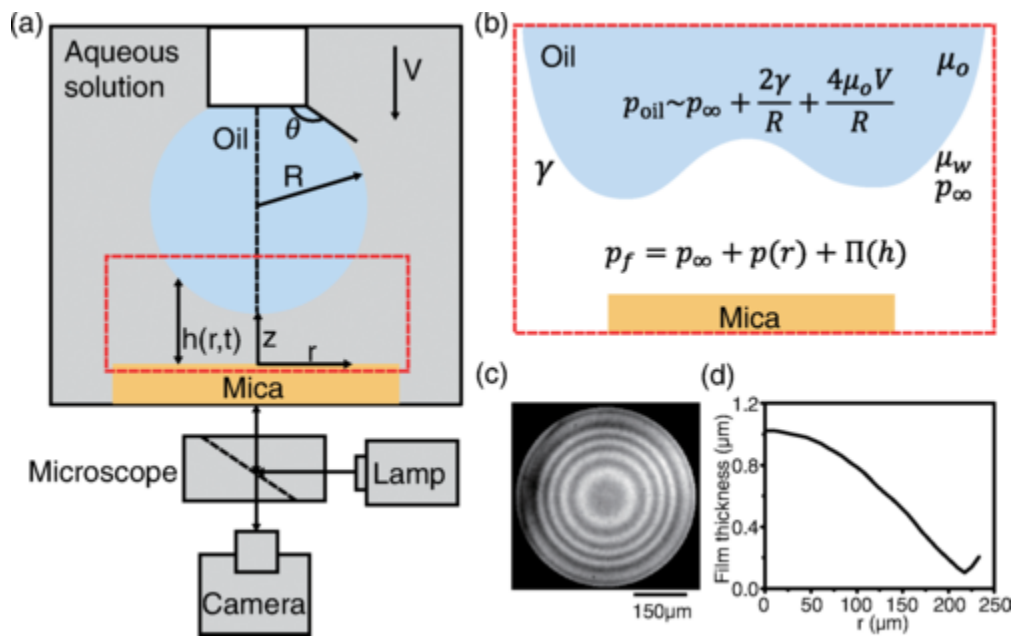


Figure 5-1 (a) Schematic of the dynamic force apparatus. An oil drop with radius $R = 1.05 \pm 0.01$ mm was generated at the end of a capillary. The drop was driven toward the hydrophilic mica surface by a motor. (b) Thin film region corresponding to the red square in (a). (c) A snapshot of the interference fringes (green channel) obtained between an oil drop and a mica surface ($\mu_o = 25.8$ Pa·s, $V = 1.06$ mm/s) in 0.1 mM SDS solution. (d) Axisymmetric film thickness profile obtained from (c).

5.3 Results and discussion

The evolution of the film thickness between the oil drop of 0.001 Pa s viscosity and the surface is shown in Fig. 5-2(a). It is noted that the viscosity of oils used in this study was measured by the hybrid rheometer and remained constant for shear rates range from 0.001 to 10 s^{-1} . Sodium dodecyl sulfate (SDS) was added into the solution to fully immobilize the oil-water interface for the low-viscosity oil drop and to adjust the oil-water interfacial tension by changing its concentration.^{43,48,49} The time $t = 0$ is defined as the moment of dimple formation. In this case, the drop forms a dimple at a height of around 2570 nm. As the film drains, the film thickness at the center first decreases to and then remains at around 2243 nm [$t = 0.085 \text{ s}$ in Fig. 5-2(a)]. The dimple becomes increasingly more pronounced as the film thickness at the barrier rim keeps decreasing. With the drive being stopped at $t = 0.218 \text{ s}$, the film thickness at the center first slightly increases, which is called the “center bounce” phenomenon.^{16,19} After that, the water film continues to drain with the film width remaining almost constant.

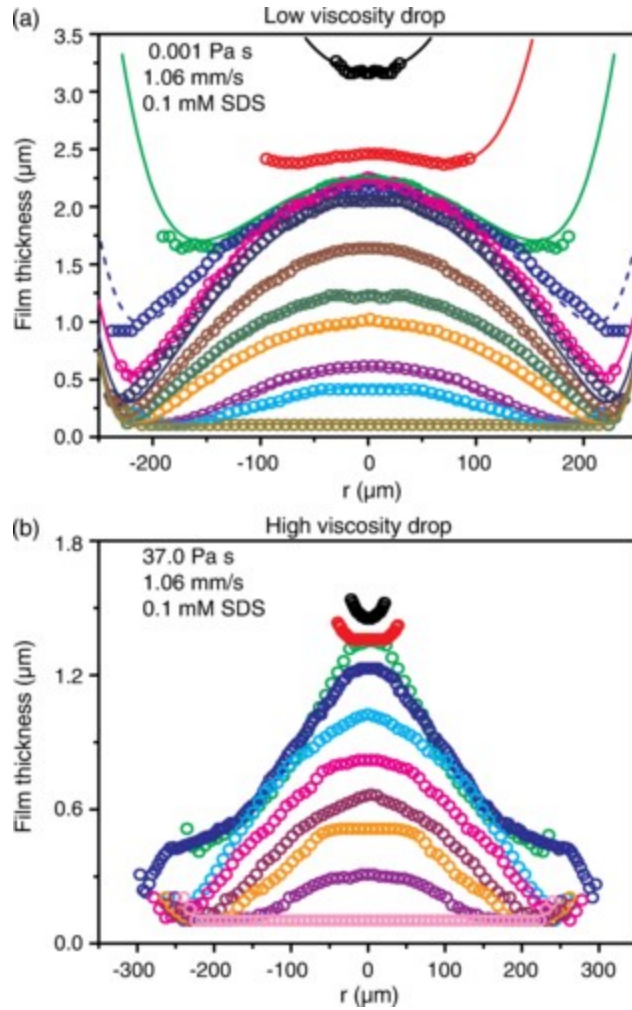


Figure 5-2 (a) Comparison between the experimental results (points) and the theoretical model (lines) for the film evolution of an oil drop of 0.001 Pa·s viscosity interacting with a mica surface in 0.1 mM SDS aqueous solution at the approach velocity of 1.06 mm/s ($Ca_d = 10^{-5}$). The measured times of the profiles from top to bottom are -0.015, 0.018, 0.085, 0.218, 0.55, 2.12, 9.07, 31.8, 66.4, 153.5, 211.9, and 331.7 s. The dashed line indicates when the oil drop stopped moving. (b) Film drainage process using an oil drop of 37.0 Pa·s viscosity in 0.1 mM SDS aqueous solution at the approach velocity of 1.06 mm/s ($Ca_d = 0.8$). The measured times of the profiles from top to bottom are -0.001, 0, 0.067, 0.618, 19.7, 97.1, 144.5, 211.0, 318.1, and 391.6 s. Drop stopped moving at 0.26 s.

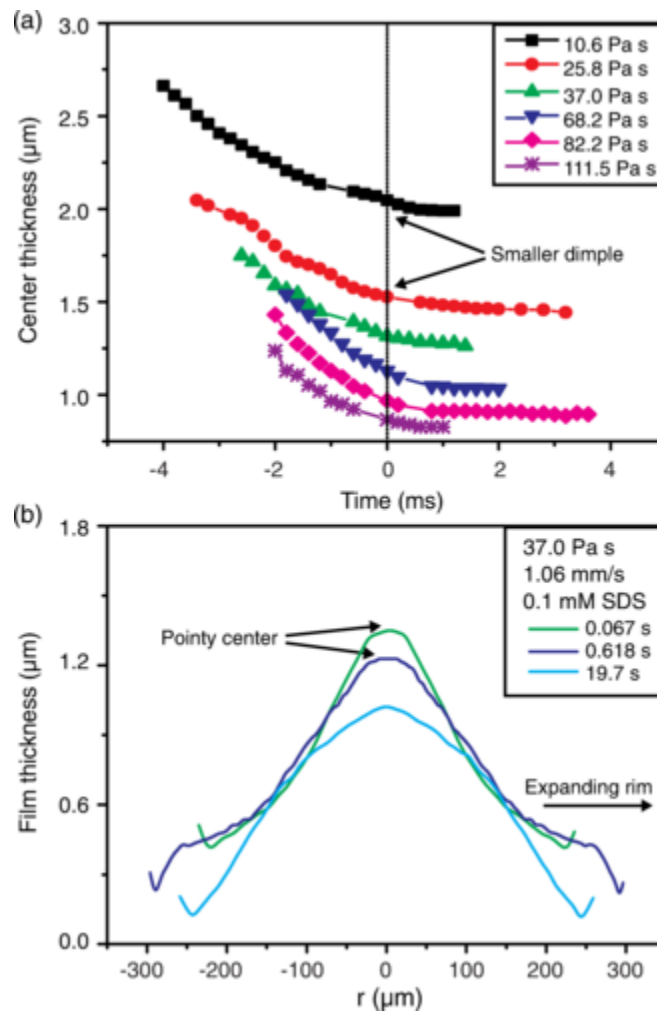


Figure 5-3 (a) Film thickness at the center $h(0,t)$ as a function of time for oil drops of different viscosity in 0.1 mM SDS solution at an approach velocity of 1.06 mm/s. (b) Selected drop shape profiles of an oil drop of 37.0 Pa·s viscosity from Fig. 2(b) in 0.1 mM SDS aqueous solution at the approach velocity of 1.06 mm/s at times 0.067, 0.618, and 19.7 s.

The film drainage process for an oil drop of high viscosity interacting with the solid surface exhibits different features. Figure 5-2(b) shows an example of the film profiles between a silicone oil drop of 37.0 Pa·s viscosity interacting with the mica surface. A distinctly different film drainage process is described as follows.

During the approach of the drop to the solid surface, the dimple formed at a lower height, as shown in Fig. 5-2(b). The height of dimple formation decreased further when increasing the oil viscosity [Fig. 5-3(a)], which is consistent with impacting highly viscous drops in air.¹⁴⁸ Such a feature cannot be explained by the silicone oil-water interfacial tension, as it barely changes with the increasing viscosity.¹⁵³ At a lower approach velocity (0.1 mm/s) for oil drops of a lower interfacial tension (in 1 mM SDS solution), the initial dimple height also decreased with increasing oil viscosity. (See Appendix C for detailed definition of dimple height, film drainage process of other selected conditions, and physical properties of oil.)

After dimple formation, the film height at the center of the film remains almost stationary despite the decrease in the minimum film height at the barrier rim. However, a pointy-shaped dimple was formed, as shown in the green curve ($t = 0.067$ s) in Fig. 5-3(b). After the drop stopped moving at $t = 0.26$ s, the water drained out, resulting in a decrease of center film thickness followed by expansion of the barrier rim. A film shape of a changing curvature formed at the same time, as shown in the dark blue curve ($t = 0.618$ s) in Fig. 5-3(b). The change in film curvature at a radius of around 250 μm was also found in impacting drop experiments.^{28, 29} Finally, the radius of the barrier rim decreased and the pointy center gradually disappeared, as shown in the light blue curve ($t = 19.7$ s) in Fig. 5-3(b).

Eventually, the water drained out under the Laplace pressure, with the final thickness controlled by the repulsive disjoining pressure due to the negatively charged drop and mica surfaces.^{95,154–156} A stable film of about 100 nm was formed.

We applied a scaling method to explain the decreasing height of dimple formation as a function of drop viscosity. In this model, we used the Stokes equation to describe the dynamics of the viscous drop.¹⁵⁷ The detailed derivation of equations can be found in the Supplemental

Material. By applying a simplified scaling analysis while considering the vertical velocity at the center point of the drop $v_{center} \sim V$ and radial dimension $r \sim R$ inside the oil drop, we estimated the contribution of the normal stress τ_v from the viscosity of the drop by

$$\tau_v \simeq \frac{2\mu_o V}{R} \quad (5-1)$$

Considering the contributions to the film pressure by the Laplace pressure and the pressure in the bulk solution (p_∞), we approximate the pressure p_{oil} along the bottom of the oil drop [see also Fig. 5-1(b)] by

$$p_{oil} \simeq 2 \left(\frac{\gamma}{R} + \frac{2\mu_o V}{R} \right) + p_\infty \quad (5-2)$$

The difference between the pressure inside the oil drop and in the thin film ($p_{oil} - p_f$), which drives the lubrication flow, is

$$p_{oil} - p_f = \frac{2\gamma}{R} + \frac{4\mu_o V}{R} - p(r) - \Pi(h) \quad (5-3)$$

where $p(r)$ is the excess hydrodynamic pressure in the water film and $\Pi(h)$ is the disjoining pressure due to surface forces. We define the characteristic pressure p_0 from Eqs. (5-2) and (5-3) as having contributions from the Laplace pressure and the viscous normal stress given by

$$p_0 = \frac{\gamma}{R} + \frac{2\mu_o V}{R} = \frac{\gamma}{R} (1 + 2Ca_d) \quad (5-4)$$

The thin film drainage is described by Reynolds lubrication theory. Here, we assume tangentially immobile boundary conditions at oil-water interfaces because the viscosity of an oil drop is much higher than the surrounding aqueous solution.¹⁵⁰ For the low-viscosity oil, the surfactant in the solution can also give rise to a immobile boundary condition,^{43,48,49}

$$\frac{\partial h}{\partial t} = \frac{1}{12\mu_w r} \frac{\partial}{\partial r} \left(rh^3 \frac{\partial p}{\partial r} \right) \quad (5-5)$$

Based on the radial dimension $r_0 = \sqrt{Rh_0}$ ^{50,158} and $h_0/t_0 = V$, Eq. (5-5) provides the following relation between all nondimensional parameters

$$V = \frac{1}{\mu_w} \frac{h_0^3 p_0}{R h_0} \quad (5-6)$$

Eliminating p_0 with Eq. (5-4) results in the characteristic film thickness

$$h_0 = R \sqrt{\frac{Ca_f}{1 + 2Ca_d}} \quad (5-7)$$

We note that the nondimensional thickness of dimple formation $h_d' = h_d/h_0$ for the interaction between two drops or between a drop and a solid surface can vary from 0.4 to 0.7 if the drops or bubbles are pinned to a solid surface, depending on the pinning angle and the fluid-fluid boundary conditions.^{15,159,160} Since the angle that the oil or bubble makes at the end of the capillary in our experiment is around 140° with immobile boundary conditions, the film thickness at which the dimple appears is around $h_d' \sim 0.5$.¹⁶ Thus, a general relation that holds at both low and high oil viscosity can be expressed as

$$h_d = 0.5h_0 = 0.5R \sqrt{\frac{Ca_f}{1 + 2Ca_d}} \quad (5-8)$$

Figure 5-4 shows the comparison between the experimental and calculated scaled dimple height using Eq. (5-8) as a function of Ca_d . The film thickness at dimple formation is scaled using the length scales $R\sqrt{Ca_f}$ typical of current system. The inset shows the dimple height as a function of oil viscosity. The prediction based on Eq. (5-8) is in good agreement with the results of our experiments. It is worth noting that obtaining the exact value of the dimple height is extremely difficult, if not impossible, although a very high frame rate (5000 frames/s) was used in this study.

The reported dimple heights are an average of the center height of 3 – 5 frames of two videos and the height of the initial dimple formation varied within a range of around 50 nm.

The master curve in Fig. 5-4 predicts the thickness of initial dimple formation for the drop capillary number Ca_d ranging from 10^{-8} to 30, including different approach velocities, interfacial tension, and drop viscosity. For a system of comparable viscosity of the drop to that of bulk solutions, i.e., $Ca_d < 0.1$, the viscous contribution to the normal stress inside the oil drop is small as compared with the Laplace pressure; that is, $Ca_d \ll 1$. The pressure difference across the oil-water interface is mainly due to the Laplace pressure. The scaling $h_d' = 0.5$ and $h_d \sim R\sqrt{Ca_f}$ holds for both our study and the results of a bubble in water against a silica surface.^{4, 8} When the oil viscosity is larger (in other words, increasing Ca_d), p_{oil} increases due to the larger viscous normal stress $2\mu_o V/R$. Increasing pressure difference across the oil-water interface, which has a similar effect as increasing the effective interfacial tension, renders the drop more difficult to deform, thus resulting in a decrease in h_d . When Ca_d is greater than 0.1, as shown in Fig. 5-4, the viscous effect inside the drop cannot be neglected. However, the model can only qualitatively predict the full drainage process as the expression of the viscous normal stress is based on scaling argument.

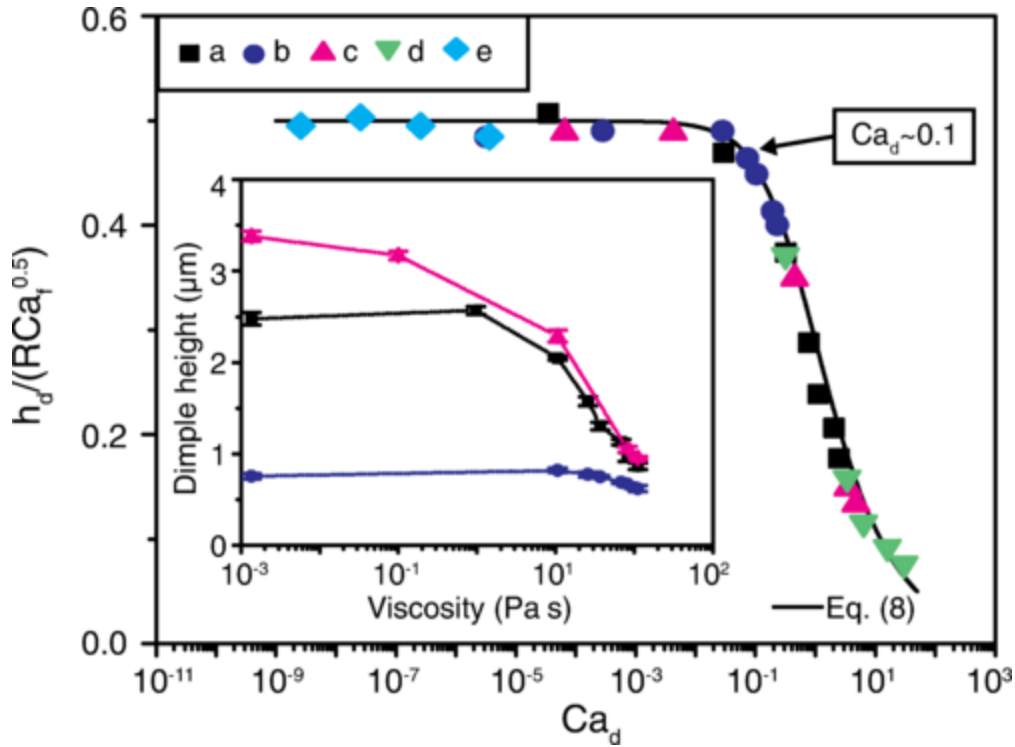


Figure 5-4 Height of initial dimple formation for oil drops or bubbles interacting with a hydrophilic solid surface in water, as a function of Ca_d as compared with the theoretical curve of Eq. (5-8) (line). The five different cases are (a) $V = 1.06 \text{ mm/s}$ in 0.1 mM SDS solution, $\mu_o = 0.001 - 111.5 \text{ Pa}\cdot\text{s}$; (b) $V = 0.1 \text{ mm/s}$ in 0.1 mM SDS solution, $\mu_o = 0.001 - 111.5 \text{ Pa}\cdot\text{s}$; (c) $V = 1.06 \text{ mm/s}$ in 1 mM SDS solution, $\mu_o = 0.001 - 111.5 \text{ Pa}\cdot\text{s}$; (d) $\mu_o = 111.5 \text{ Pa}\cdot\text{s}$ in 0.1 mM SDS solution, $V = 0.1 - 10 \text{ mm/s}$; (e) bubble interacting with silica in water. The data of the dimple height for bubble interacting with hydrophilic silica surface in water (e) is from Ref. 16. The result of the theoretical calculation fit well with the results from corresponding experiments. The transition occurred at Ca_d around 0.1. Inset: the height of initial dimple formation as a function of oil viscosity (same legend).

5.4 Conclusion

In summary, by considering the viscous normal stress inside the oil drop, we showed that the competition between the Laplace pressure and viscous normal stress inside the drop was responsible for a significantly reduced height of initial dimple formation. After the drive of the drop stopped, the viscous normal stress became negligible, resulting in the film drainage being controlled by the disjoining pressure. The initial deformation characteristics for the oil interacting with a solid surface in a SDS aqueous solutions was well captured by an analytical formula [Eq. (5-8)], which holds for a wide range of drop capillary numbers. At low drop capillary number, the capillary force was found to be dominant and the universal scaling $h_d \sim R\sqrt{Ca_f}$ described the drop deformation. When the capillary number of the oil drop $Ca_d > 0.1$, the viscosity of the oil drop needed to be taken into consideration and the drop capillary number became a dominant factor. Our systematic study verified that the viscous normal stress inside the very viscous oil drop, which leads to a higher effective interfacial tension, is the fundamental reason for decreasing the drop deformation.

Chapter 6 Effect of Viscosity on the Thin Film

Drainage between Bitumen and a Hydrophobic

Silica Wafer

Abstract

The drainage of the thin liquid film between a high viscosity droplet and a solid surface or two approaching droplets is crucial in many industrial applications. For example, in oil sands extraction the viscosity of bitumen significantly affects the liberation and aeration stages. However, previous studies rarely considered the effect of the bitumen viscosity on the dynamic thin film drainage. In this study, we used the dynamic force apparatus (DFA) to study the initial film drainage process between a bitumen drop with high viscosity compared to the surrounding aqueous solution and a hydrophobic silica wafer in 10 mM NaCl solution at pH 8.5 with Reynolds number ranging from 0.27 to 3.8. The film drainage process of bitumen with comparable viscosity to the aqueous phase can be well predicted by the Stokes-Reynolds-Young-Laplace model. However, the film drainage between bitumen with high viscosity and silica would form a much thinner dimple, followed by a film with a pointy-shaped center and a change of curvature at the radius of around 300 μm . The addition of different types of solvent or increasing the experimental temperature would not affect the initial stage of dimple formation. A higher approach velocity and a smaller interfacial tension would result in a more pronounced dimple, but this effect would become minor when the bitumen viscosity is high enough. The initial height of dimple formation between bitumen with different viscosity and a hydrophobic surface can be perfectly predicted by the analytical formula derived using pure oil and a hydrophilic surface, $h_d = 0.5R\sqrt{Ca_f/(1 + 2Ca_d)}$. It also shows that a lower bitumen drop approach velocity, a higher bitumen/water interfacial tension, and a smaller bitumen viscosity would facilitate bitumen attachment to the silica surface. Our study provides valuable information on the dynamic film drainage process, which has crucial implications for many industrial applications involving high viscosity oils.

6.1 Introduction

Bitumen is a form of petroleum that has a very high viscosity. Studies have shown that the viscosity of bitumen is usually over 100 Pa·s at room temperature and standard atmospheric pressure, and can be as high as 1000 Pa·s, depending on the source of bitumen.⁶⁵⁻⁶⁷ The viscosity of the Athabasca bitumen was also found to decrease significantly by increasing the temperature and decreasing the pressure.⁶⁷ To improve the bitumen recovery, increasing the operating temperature and the addition of solvent were applied in the industrial process.¹⁶¹ It has been found that, at the same bitumen/water interfacial tension, the decrease in bitumen viscosity would increase the rate of bitumen liberation.⁶⁵ Using a model oil, a faster receding of the oil contact area has been observed on a hydrophilic silica sphere with less viscous oil and similar oil/water interfacial properties, which also indicated that the viscosity of the oil is a limiting parameter for the oil receding process.¹⁶² In spite of the bitumen liberation and oil receding process, the reduction of the bitumen viscosity would also facilitate the bubble-bitumen attachment for the bitumen containing less than 10 wt% solvent, thus enhancing the bitumen aeration process.^{11,161}

When a bitumen drop approaches a solid surface, an air bubble, or another bitumen drop, the drainage of the intervening thin water film between the surfaces determines the stability behavior of the bitumen drop. The properties at the interfaces (including the interfacial tension γ ¹⁷ and the zeta potential²¹), inherent properties of the oil drop (viscosity μ_o ⁴⁷), hydrodynamic factor (approach velocity V ^{16,18}) and the surrounding aqueous solution (salinity¹⁶) would all have relevant influence on the formation of the dimple and the following dynamic thin film drainage process. The thickness and the stability of the final thin water film are determined by the extended DLVO theory, considering the van der Waals (vdW), electrostatic double layer (EDL), and hydrophobic (HB) forces.

To investigate this intervening thin water film, atomic force microscopy (AFM), surface force apparatus (SFA), and dynamic force apparatus (DFA) have been applied. AFM and SFA have been widely used for the direct measurement of colloidal interactions between an air bubble²¹ or oil drop³² and a solid surface or two bubbles/oil drops²⁸ under low Reynolds number regime ($Re = 2\rho RV/\mu_w < 10^{-2}$, where R is the bubble/drop radius, μ_w and ρ are the viscosity and density of aqueous phase, respectively). The drop barely deforms in this regime of Reynolds number and the dynamic interaction is also negligible.³³ However, in the water-based heavy oil extraction process, the traveling velocity of the slurry in the hydrotransport can be up to several meters per second. The relative velocity between bitumen drop, air bubble, and solids is in the range of millimeter per second, which determines the dynamic interactions. With the combined usage of a motorized actuator and a speaker, the DFA could achieve a higher Reynolds number from 0.027 to 37.75 by controlling the approach velocity from 0.01 to 10 mm/s.¹⁶ This instrument can measure the spatiotemporal film thickness between bubble/bitumen drop and solid/bubble in aqueous systems.^{16,43}

However, studies on real bitumen droplet are always hard to conduct using those instruments due to the high viscosity of bitumen. For the studies using AFM and SFA, a bitumen surface was usually created on a hydrophobic silica wafer by spin-coating^{20,21} or on a silica sphere by dip-coating^{22,26} As for the DFA, a solvent diluted bitumen or an asphaltene drop were used.^{18,71} In these cases, compared to the real industrial application, the viscosity of bitumen has not been the focus of previous studies, which might have a strong effect on the dynamic thin liquid drainage process.

In this study, we used the DFA to investigate the initial film drainage process between real bitumen or bitumen diluted by little amount of solvent, and a hydrophobic silica surface. The

impacts of solvent, approach velocity, and temperature on the initial film drainage process were investigated using a bitumen drop with the viscosity close to the industrial applications. The experimental film drainage process was analyzed using a theoretical model based on Reynolds lubrication theory and a modified Young-Laplace equation considering the viscous normal stress inside the bitumen drop. The initial height of dimple formation was predicted by an analytical formula. Our results provide valuable information on the thin film drainage between bitumen with comparable viscosity as the industrial application and a solid surface that will have great implications on the heavy oil extraction process.

6.2 Experimental section

6.2.1 Materials and Methods

Vacuum distillation unit (VDU) feed bitumen provided by Syncrude Canada, Ltd. was used in this study. The substrate was prepared by treating a transparent silica wafer (NanoFAB, CA) with octadecyltrichlorosilane (OTS) (>96% purity, Sigma Aldrich). Sodium dodecyl sulfate (SDS, 99% purity, Sigma), decane (>99% purity, Fisher), and toluene (99.8% purity, Sigma) were used without any purification. Sodium chloride (NaCl, ACS grade, Fisher Scientific) was roasted in an oven at 600 °C for 8 h before use to remove organic contaminants. All aqueous solutions were prepared using Milli-Q water with a resistivity of 18.2 M Ω ·cm deionized by a Barnstead Nanopure system (Thermo Fisher Scientific). Sodium hydroxide (NaOH, ACS reagent grade) purchased from Fisher Scientific was diluted to 1N and used to adjust the solution pH.

6.2.2 Instrument setup

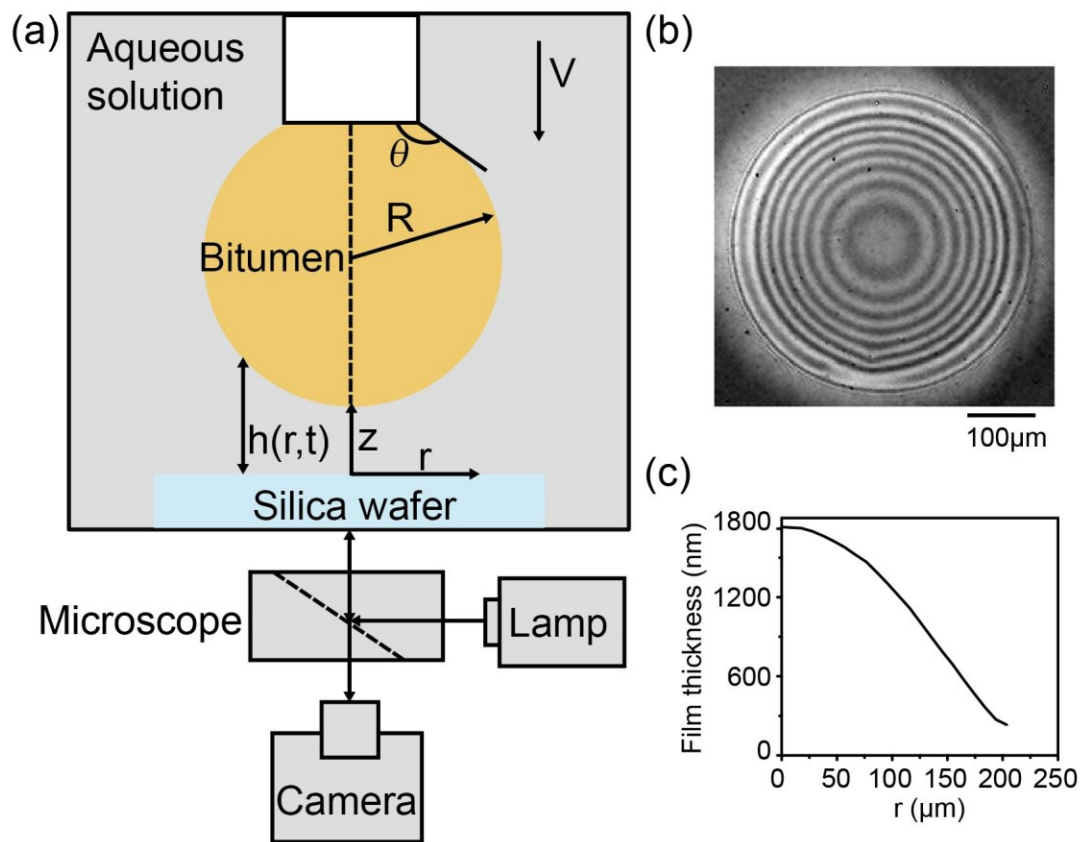


Figure 6-1 (a) Schematic of the dynamic force apparatus. A bitumen drop with radius $R = 1 \pm 0.01 \text{ mm}$ was generated at the end of a capillary tube. The drop was driven towards the hydrophobic silica wafer by a motor. (b) A snapshot of the interference fringes (green channel) obtained between a 90 wt% bitumen in toluene and a silica surface ($\mu_o = 23.4 \text{ Pa}\cdot\text{s}$, $V = 1 \text{ mm/s}$) in 10 mM NaCl solution. (c) Axisymmetric film thickness profile obtained from (b).

The drainage of the aqueous film between a bitumen drop and a hydrophobic silica wafer was studied using the dynamic force apparatus (DFA) in 10 mM NaCl solution at pH 8.5 for all experiments. A schematic of the DFA is shown in Figure 6-1a. A bitumen drop with radius $R = 1 \pm 0.01 \text{ mm}$ was generated at the end of a capillary tube. To obtain a hydrophobic silica wafer, the silica surface was immersed in piranha solution for 2 h. The cleaned silica wafer was then rinsed with a great amount of Milli-Q water to remove the residual acid. After that, the silica wafer

was dried with nitrogen gas and then immersed in 25 mM OTS in toluene solution overnight to obtain a uniform hydrophobic surface. The water contact angle of the hydrophobic silica wafer was measured to be around 100°. The initial distance between the bitumen drop and the silica surface was set at 350 μm , which was monitored and controlled by a side-view camera. The displacement of the bitumen drop was controlled to be 500 μm . The drop approach velocities were selected as 0.1 mm/s and 1 mm/s, which were achieved by a motorized actuator.

The interference fringes were observed by an inverted Axiovert 100 Carl Zeiss microscope and were recorded by a high-speed video camera (Photron SA4, 60-500,000 fps). Figure 6-1b shows an example of the interference fringes between 90 wt% bitumen in toluene interacting with the hydrophobic silica wafer. The film thickness as a function of radial coordinate was obtained by analyzing the fringes using the method adopted by Scheludko and Platikanov¹⁶³ (See details in Appendix D) and the corresponding film thickness is shown in Figure 6-1c.

The viscosity of the solvent diluted bitumen was measured using the hybrid rheometer (HR-2) under the shear rates ranging from 0.001 to 10 s^{-1} at room temperature (22.5 °C).

The viscosity of pure bitumen was measured at 40 and 45 °C under the 0.001 to 1 s^{-1} shear rate to avoid the considerable temperature increase of the sample due to the dissipation arising from viscous flow at a high shear rate. The measured viscosity remained constant within the experimental shear rate range.

6.3 Results

It is worth noting that the viscosity of bitumen used in this study at room temperature is around 2000 Pa·s, which cannot form a spherical drop at the end of the capillary. Therefore, high temperature or solvent addition were used to slightly decrease the bitumen viscosity.

6.3.1 Solvent diluted bitumen

Toluene and decane were selected as two typical solvents to dilute bitumen. The solvent and bitumen mixture was shaken for at least 24 hr to ensure that solvent and bitumen were well mixed. Diluted bitumen was used immediately after mixing to minimize the effect of aging and solvent evaporation. The properties of different diluted bitumen drops are given in Table 6-1. It is worth noting that the decane diluted bitumen/water interfacial tension was taken from the interfacial tension of a 30 wt% decane diluted bitumen. According to the study by Schramm et al., added n-decane does not alter the bitumen/water interfacial tension until the mass concentration of n-decane exceeds about 50 wt%.^{61,164,165}

Table 6-1 Physical properties of different solvent diluted bitumen

Oil type	Oil viscosity (Pa·s)	Interfacial tension (mN/m)
50 wt% bitumen in toluene	0.009	18 ⁷¹
90 wt% bitumen in toluene	23 ± 2	5 ⁶⁵
93 wt% bitumen in toluene	80 ± 6	8 ⁶⁵
90 wt% bitumen in decane	30 ± 1	18 ⁶¹
93 wt% bitumen in decane	93 ± 6	18 ⁶¹

6.3.1.1 Toluene diluted bitumen

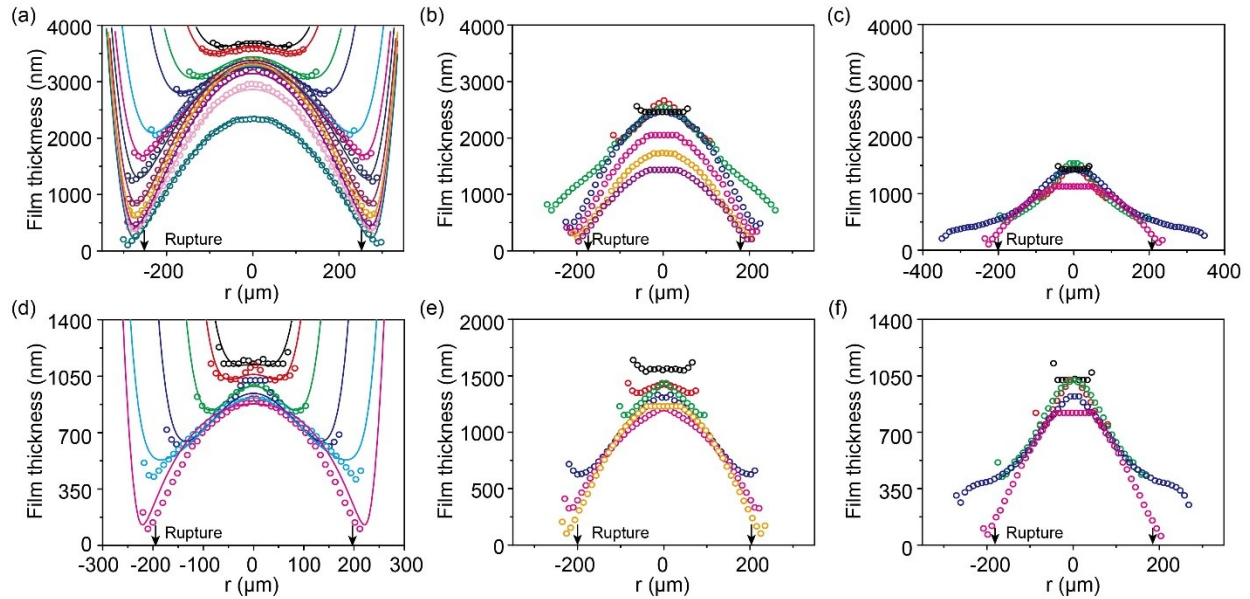


Figure 6-2 Film drainage process between toluene diluted bitumen drop and a hydrophobic

silica wafer in 10 mM NaCl solution at $V = 1$ mm/s (a-c) and $V = 0.1$ mm/s (d-f). (a)

Comparison between theoretical model (lines) and experimental results (points) of film thickness

for 50 wt% bitumen in toluene. The measured time from top to bottom are 0, 0.01, 0.04, 0.07,

0.16, 0.22, 0.32, 0.65, 1.36, 2.70, 5.89, 17.46 s. (b) 90 wt% bitumen in toluene at 0, 0.02, 0.34,

4.77, 13.52, 30.48, 54.31 s. (c) 93 wt% bitumen in toluene at 0, 0.01, 0.04, 0.31, 8.97s. (d)

Comparison between theoretical model (lines) and experimental results (points) of film thickness

for 50 wt% bitumen in toluene. The measured time from top to bottom are 0, 0.06, 0.27, 0.69,

1.24, 6.74 s. (e) 90 wt% bitumen in toluene at 0, 0.07, 0.17, 1.02, 2.59, 13.91 s. (f) 93 wt%

bitumen in toluene at 0, 1.06, 1.34, 2.54, 26.4 s.

The film drainage process of different concentration of toluene diluted bitumen interacting with a hydrophobic silica wafer is shown in Figure 6-2. The dots represent the experimental data while the lines represent the theoretical calculation. The downward arrows represent the water film rupture for the last film profile. The zero time for all the conditions is defined as the time of dimple

formation. The methodology of defining the dimple formation can be found in our previous study.⁴⁷ It is worth noting that the interference fringes were recorded after aging the bitumen drop in water solution for 10 min. With the decreasing toluene content inside the bitumen, the viscosity of the diluted bitumen increase from ~ 0.009 Pa·s to ~ 80 Pa·s. The film drainage process showed significantly different features with the increasing oil viscosity.

Figure 6-2a shows the film drainage process between 50 wt% toluene diluted bitumen and a hydrophobic silica wafer at the approach velocity of 1 mm/s. The oil viscosity was around 0.009 Pa·s, close to the viscosity of the surrounding aqueous phase. As the drop was approaching the solid surface, once the hydrodynamic pressure of the water film exceeded the pressure inside the bitumen drop, the curvature of the bitumen drop inverted, resulting in dimple formation. For this condition, the height of dimple occurrence was around 3584 nm. After the dimple formed, the height at the center remained almost constant while the height at the barrier rim kept decreasing over time, resulting in a more and more pronounced dimple. After the drop stopped moving at $t = 0.22$ s, the film thickness at the center of the film slightly increased from 3254 nm to 3337 nm, with the height at the barrier rim still decreasing. This is known as the “center bounce” phenomenon that has been found in previous studies, which might be the consequence of the discontinuity in acceleration as the bitumen drop stopped moving.^{16,19} After that, the height at the center and barrier rim kept decreasing, with the film radius remaining mostly constant and eventually the water film ruptured when the film thickness at the barrier rim reached around 100 nm. It is worth noting that the film thickness at the barrier rim was always greater than 100 nm for the 50 wt% bitumen in toluene, which is well beyond the range of surface forces for this system. This is probably caused by surface roughness or minor contaminants in the system. The experimental drop profile could be well predicted by the SRYL model, as shown in Figure 6-2a.

For the bitumen drop with high viscosity, as shown in Figures 6-2b and c, the film drainage exhibited significantly different features. When the bitumen concentration was increased from 50 wt% to 90 wt%, the bitumen/water interfacial tension decreased from 18 to 5 mN/m, and increased to around 8 mN/m for the 93 wt% bitumen in the toluene case. It is worth noting that the bitumen/water interfacial tension was measured to be around 1 mN/m using the drop relaxation method.⁶⁵ However, the interfacial tension was fitted to be around 5 mN/m in our study, which is likely due to the less surfactant content in our solution. Ideally, the height of dimple occurrence would increase with the decreasing interfacial tension when the drop radius and the approach velocity remain the same. However, the height of dimple formation decreased from 3584 nm to around 2450 nm and further decreased to around 1211 nm when the bitumen concentration increased from 50 wt% to 93 wt%. After the initial dimple formation, a pointy-shaped film was formed afterward. The pointy shape became more and more significant when the bitumen concentration increased from 90 wt% to 93 wt%, as shown as the green curve in Figure 6-2c. This could be explained by the drop viscosity increasing from 23 Pa·s to 80 Pa·s. The film thickness at the barrier rim continued decreasing and a plateau was formed at the radius of around 300 μm , given as the blue curve in Figure 6-2c. Unlike the low viscosity cases, the rim radius expanded initially then shrank slightly after the drop stopped moving and then remained mostly constant and the pointy center disappeared in the meantime, as shown in the red curve in Figure 6-2c. This phenomenon has also been found in the previous study.⁴⁷ Eventually, the film drained out controlled by the Laplace pressure and the drop attached to the surface when the film thickness was around 50 nm.

Figure 6–2d-f shows the film drainage process between different toluene diluted bitumen and a hydrophobic silica wafer at the approach velocity of 0.1 mm/s. The film drainage process of

low viscosity case (50 wt% bitumen in toluene, 0.009 Pa·s) is also in agreement with the SRYL theoretical model. However, a less favorable agreement between experiment and theory compared with high approach velocity case showed in this condition due to the fewer interference fringes, as shown in Figure 6-2d. A significantly smaller dimple was formed at the lower approach velocity. The height of the initial dimple formation decreased from 3584 nm to around 1126 nm when the approach velocity was reduced from 1 mm/s to 0.1 mm/s. With the increasing drop viscosity (90 wt% and 93 wt% bitumen in toluene), the height of dimple formation first increased to around 1525 nm then decreased to around 1001 nm at lower approach velocity. When the approach velocity is low ($V = 0.1$ mm/s), the effect of bitumen/water interfacial tension becomes a dominant factor compared with the oil viscosity that would affect the initial height of dimple formation. The bitumen/water interfacial tension first decreased then increased with the increasing bitumen content resulting in a first increasing then decreasing dimple height. Decreasing the velocity would decrease the initial height of dimple formation for both low and high viscosity cases. With the increasing oil viscosity, the difference between the heights of dimple formation at high and low velocity decreased. This is because the effect of velocity becomes minor when the oil viscosity is relatively high.

The height of dimple formation is still much lower than the theoretical value predicted by the SRYL model for 90 wt% toluene diluted bitumen at approach velocity of 0.1 mm/s, as shown in Figure 6-2e. However, the film drainage process is still similar to the cases when the oil viscosity is comparable to water. When the oil viscosity is around 80 Pa·s at $V = 0.1$ mm/s, the water film shows different features, including the pointy-shaped center and an expanding and shrinking rim. At low approach velocity, the features typical for the water film for high viscosity oil exhibit at a

much higher oil viscosity compared with high approach velocity conditions, indicating the combined effect of approach velocity and oil viscosity on the thin film drainage.

6.3.1.2 Decane diluted bitumen

The film profile of decane diluted bitumen interacting with the hydrophobic silica wafer is shown in Figure 6-3. Only high bitumen concentration (90 wt% and 93 wt% bitumen in decane) was used in this study to minimize the asphaltene precipitation. With the increasing oil viscosity, the initial height of dimple formation decreased at both high and low approach velocities. For the oil with the same viscosity, a decrease in approach velocity would also result in a smaller dimple. The height of the initial dimple formation for the decane diluted bitumen under all the cases was slightly lower than that for the toluene diluted bitumen, which is caused by a higher viscosity and bitumen/water interfacial tension for decane dilute bitumen. However, the features of the aqueous film are the same as those for toluene diluted bitumen. The water film formed a pointy-shaped center, followed by a changing curvature. Moreover, an increase in the rim radius could be found at high approach velocity and the high viscosity case at low approach velocity. Thus, the slight asphaltene precipitation and the solvent type does not affect the initial stage of dimple formation.

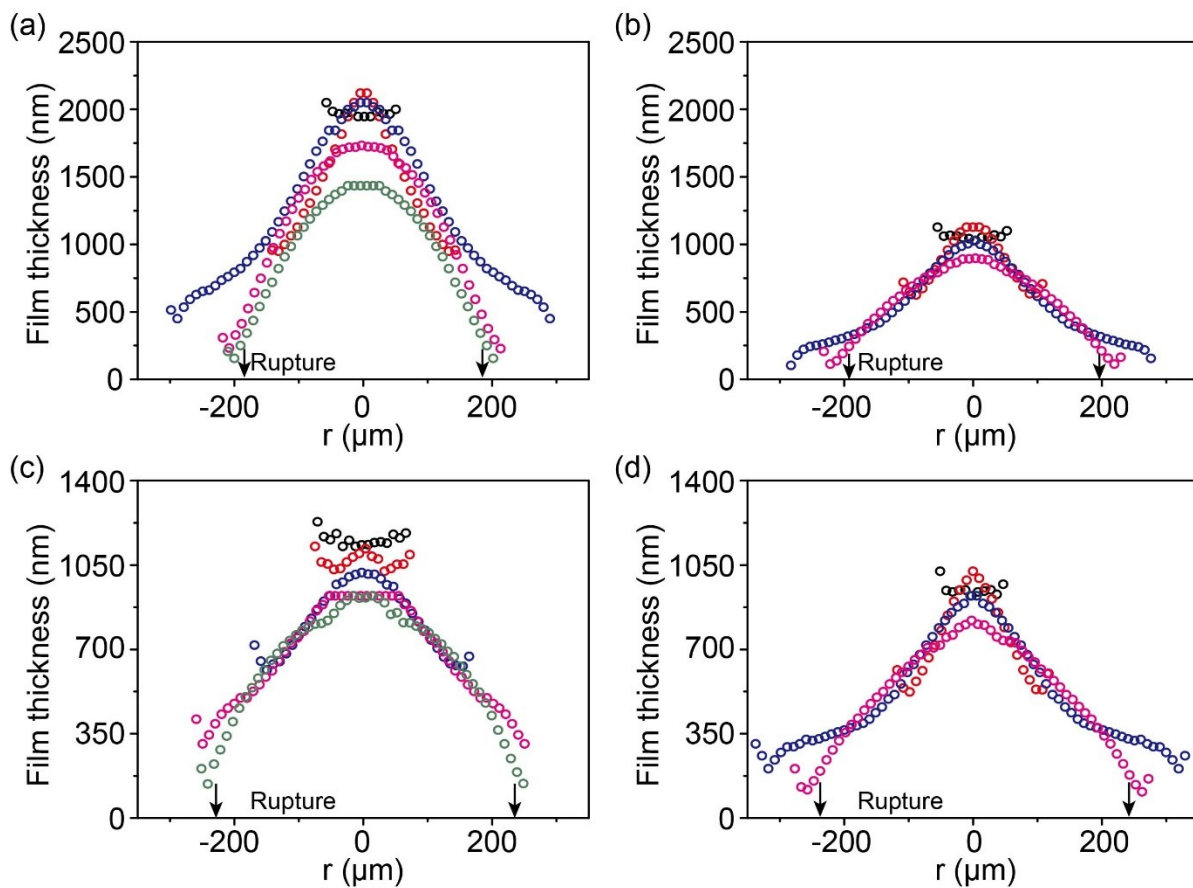


Figure 6-3 Film drainage process between decane diluted bitumen drop and a hydrophobic silica wafer in 10 mM NaCl solution at $V = 1 \text{ mm/s}$ (a, b) and $V = 0.1 \text{ mm/s}$ (c, d). (a) 90 wt% bitumen in decane. The measured time from top to bottom are: 0, 0.03, 0.31, 13.26, 38.05 s. (b) 93 wt% bitumen in decane at 0, 0.01, 5.55, 148.43 s. (c) 90 wt% bitumen in decane at 0, 0.05, 0.50, 1.60, 3.90 s. (d) 93 wt% bitumen in decane at 0, 0.14, 2.16, 16.22 s.

6.3.2 Bitumen at different temperature

Table 6-2 Physical properties of bitumen at different temperature

Temperature (°C)	Oil viscosity (Pa·s)	Interfacial tension (mN/m)
40	281 ± 10	18
45	133 ± 2	17.5

The experiments at high temperature were conducted in a water bath in order to maintain the temperature constant. The temperature of the aqueous solution was measured before and after the experiments and it remained almost the same. The properties of bitumen at 40 and 45 °C were shown in Table 6-2. It was revealed that the bitumen/water interfacial tension varied little with temperature at the experimental pH of 8.5. Thus, the interfacial tension at high temperature was estimated based on the data at 20 °C by a linear correlation with a temperature coefficient of -0.013 mN/(m·deg).^{2,166}

The initial film drainage process between bitumen and a hydrophobic silica wafer at 40 and 45 °C are shown in Figures 6-4a and b at an approach velocity of 1 mm/s. It is worth noting that there is a certain amount of small particles that stick to the bitumen/water interface and that would have some effect on the analysis of the interference fringes. There is no attachment happening between bitumen and hydrophobic silica wafer at both 40 and 45 °C after 10 min aging within the experimental shooting time. However, it would not affect the initial dimple formation. The bitumen viscosity is measured to be around 281 Pa·s at 40 °C and the bitumen drop could still have a very small deformation during the approach process at this high viscosity. The initial height of dimple formation barely changed (628 ± 14 nm at 1 mm/s and 573 ± 40 nm for 0.1 mm/s, see film drainage process at 0.1 mm/s in the Appendix D) under this condition when the approach

velocity decreased from 1 mm/s to 0.1 mm/s. At 45 °C, the bitumen viscosity decreased to around 132 Pa·s, only causing a slight increase of 200 nm to the height of dimple formation, as shown in Figure 6-4b. Decreasing the approach velocity from 1 mm/s to 0.1 mm/s could cause a 100 nm decrease in the height of dimple formation.

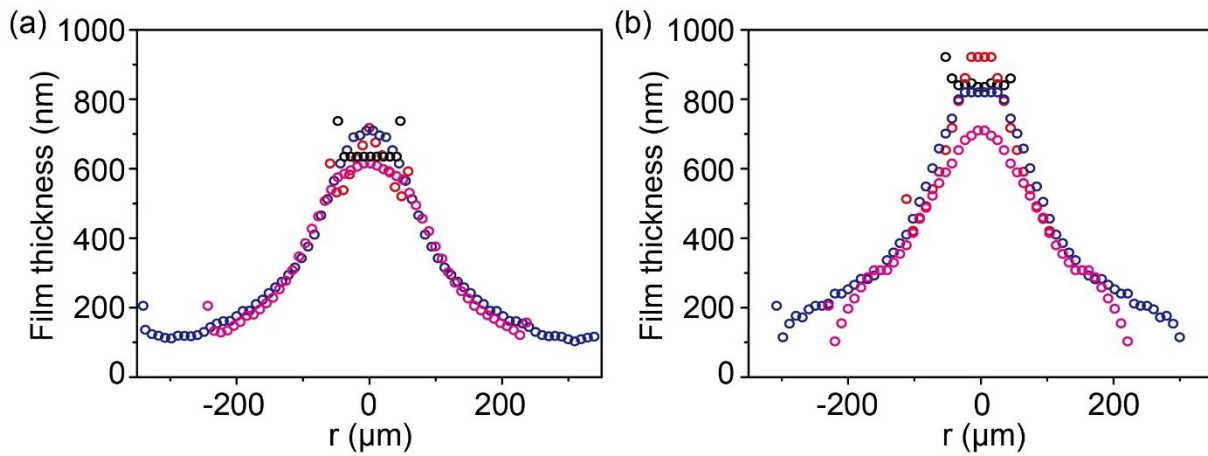


Figure 6-4 Film drainage process between bitumen drop and a hydrophobic silica wafer in 10 mM NaCl solution at $V = 1$ mm/s at high temperature: (a) 40 °C. The measured time from top to bottom are: 0, 0.002, 0.67, 16.0 s. (b) 45 °C. The measured time from top to bottom are: 0, 0.01, 1.66, 47.91 s.

6.4 Discussion

6.4.1 The moment of dimple formation

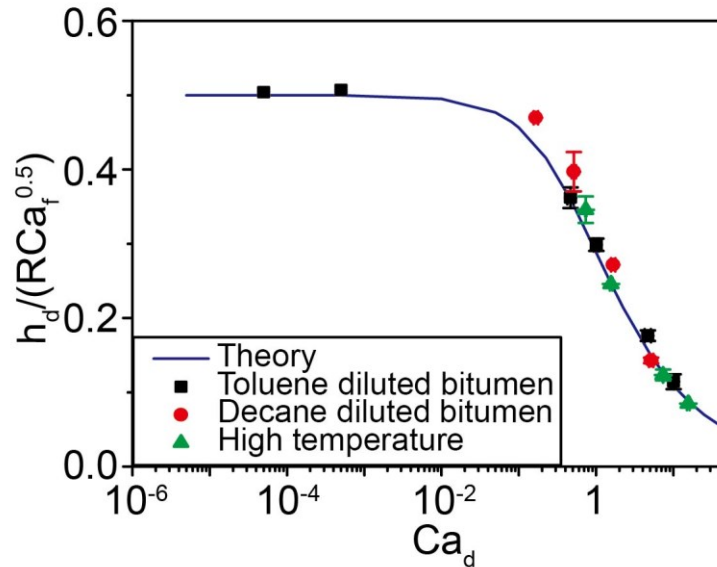


Figure 6-5 Comparison between the scaled experimental dimple height and the theoretical calculation using Eq. (6-1). The theoretical calculation agrees with the experimental data very well.

The competition between the Laplace pressure ($2\gamma/R$) and the viscous normal stress ($4\mu_o V/R$) inside the bitumen drop is the primary reason for the different features of the evolution of the water film for bitumen drop with high viscosity. The viscous normal stress is proportional to the velocity of the center of the drop. The velocity at the center is at its maximum and nearly equal to the approach velocity when the drop is approaching the surface. After the initial dimple occurrence, the central velocity starts decreasing and reaches almost zero when the drop stops moving. At the approaching stage, the viscous normal stress controls the process, leading to a much lower initial dimple height and a pointy-shaped film center. After that, the water film shape of a changing curvature is formed, followed by an increase of the radius of the barrier rim, which

is likely due to the drop reaction to the sudden stop under the high viscous normal stress. After the drop stops moving, the viscous normal stress becomes negligible, resulting in the typical film drainage process controlled by the Laplace pressure.

As previously reported, the initial height of dimple formation is strongly affected by the interfacial tension, velocity, and especially the viscosity of the drop. Consider a drop with an immobile boundary condition, the first occurrence of dimple between a pure oil and a hydrophilic silica wafer can be expressed as a function of the capillary number of the water film and bitumen drop:⁴⁷

$$h_d = 0.5R \sqrt{\frac{Ca_f}{1 + 2Ca_d}} \quad (6-1)$$

Figure 6-5 shows the comparison between the experimental and calculated scaled dimple height using Eq. (6-1) as a function of Ca_d . The film thickness of dimple formation is scaled using the length scale ($R\sqrt{Ca_f}$), typical of the current system. It shows that the analytical formula derived from the ideal system with a hydrophilic surface can also be applied in the complicated bitumen system with a hydrophobic surface. Eq. (6-1) can well predict the scaled dimple height for all the conditions in our experiments. Eq. (6-1) clearly shows that when the viscosity of the bitumen drop is comparable to the surrounding aqueous solution, the approach velocity and the interfacial tension would have a dominant effect on the height of the dimple occurrence. When the viscosity of bitumen drop is much larger than that of the surrounding solution, the effect of the approach velocity and the interfacial tension becomes less important and the drop viscosity is the dominant factor that affects the height of dimple occurrence. As shown in Figure 6-5, when the capillary number of the drop is relatively low, the scaled dimple height is constant at 0.5, which is consistent with the previous study between an air bubble and a hydrophilic solid surface in water.¹⁶ When

$Ca_d > 0.1$, the effect of Ca_d needs to be taken into consideration and the scaled dimple decreases with the increasing Ca_d .

6.4.2 Attachment time

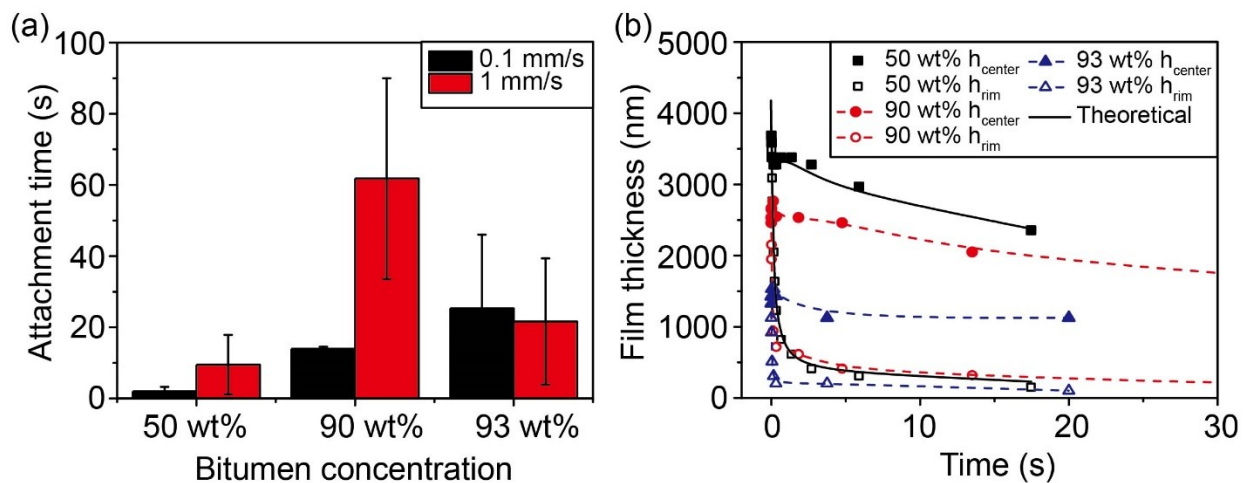


Figure 6-6 (a) Attachment time between different concentration of bitumen in toluene and a hydrophobic silica wafer at different approach velocities. (b) Film thickness at the center $h(0, t)$ and at the barrier rim $h(r_{rim}, t)$: symbols for experimental results, solids lines for corresponding theoretical predictions and dashed lines for guiding eyes (filled symbols for $h(0, t)$ and opened symbols for $h(r_{rim}, t)$).

The attachment time could vary considerably when comparing two experiments under similar conditions. For example, it could vary by over a factor of 10 between two bubbles under the same experimental conditions.¹⁶⁷ This is probably because the attachment between either drop and solid or two drops (bubbles) could easily be induced by a tiny amount of impurities.

We define the attachment time in our study as the time between dimple occurrence and film rupture; it is obtained by averaging 5 experimental runs. The attachment time of the toluene diluted bitumen and the hydrophobic silica wafer is shown in Figure 6-6a. At 1 mm/s approach velocity,

the attachment time would first increase then decrease with the increasing bitumen concentration. The film thickness at the center and rim as a function of time is shown in Figure 6-6b. When the bitumen concentration was increased from 50 wt% to 90 wt%, the bitumen/water interfacial tension decreased from 18 mN/m to 5 mN/m, leading to a much slower film drainage rate and a longer film lifetime. For example, for 50 wt% bitumen in toluene, it took around 9 s for the height of the barrier rim to decrease from 3584 nm to 102 nm. But it took around 62 s for the height of the barrier rim to decrease from 2365 nm to 102 nm for 90 wt% bitumen in toluene. When the bitumen concentration was increased from 90 wt% to 93 wt%, the increasing bitumen/water interfacial tension and also the decreasing height of dimple occurrence both caused a shorter film lifetime, leading to a decrease in attachment time. The decreasing approach velocity would cause a decrease in attachment for all conditions, which is consistent with a previous study.¹⁸ This could be explained by the larger dimple formation at high approach velocity, leading to a longer film lifetime when the interfacial tension remained the same.

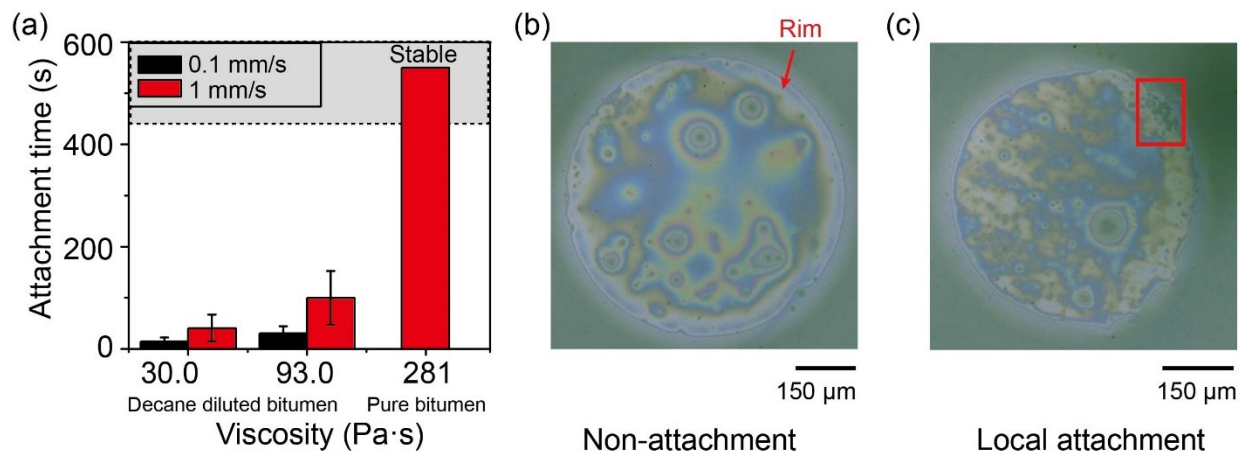


Figure 6-7 (a) Attachment time between bitumen with different viscosity and hydrophobic silica wafer at different approach velocities. (b) Snapshot of a stable water film formed by bitumen at 40 °C and a hydrophobic silica wafer after 10 min aging at $V = 1$ mm/s within the maximum

shooting time (10 min). (c) Snapshot of water film in which local attachment happens for bitumen at 40 °C. The red square represents the place where local attachment happens.

For the decane diluted bitumen, attachment would happen for all conditions within tens of seconds after 10 min aging time, as shown in Figure 6-7. The solid particles or the asphaltene aggregates on the oil/water interface and the heterogeneity of the bitumen surface would induce attachment, causing a huge standard deviation on the attachment time. However, it still seems that the attachment time increases with the increasing drop viscosity for two approach velocities, especially for the decane diluted bitumen drop, although the height of dimple formation increases with the decane concentration. For the pure bitumen, the attachment time could possibly increase to dozens of minutes, which exceed the experimental shooting time (10 min). A dimple would still form at the beginning, and drain out afterwards. However, the film would not rupture after the water drains out and the thin water film is stable. As shown in Figure 6-7b, a stable water film was formed with a thickness at the barrier rim of around 50 nm. Due the solid particles or some asphaltene aggregates sticking to the bitumen surface, the water film has some higher or lower domains which is hard to analyse. For some other conditions, bitumen could have local attachment to the solid surface, as shown as the red square in Figure 6-7c. However, the three phase contact line would not spread within the experimental shooting time (10 min). This is probably caused by the solidification of the bitumen drop preventing it from attaching to the solid surface. The decreasing oil viscosity would enhance the mobility of the bitumen/water interface at the same aging time, which is responsible for the shorter attachment time.^{11,161}

For the bitumen drop with the same viscosity and the same bitumen/water interfacial tension, the formation of a smaller dimple could significantly decrease the attachment time. A decrease in bitumen/water interfacial tension would significantly slow down the film drainage

process, thus significantly increasing the attachment time, even if a smaller dimple formed. The increase of the bitumen viscosity would facilitate the solidification of the bitumen drop and prevent bitumen attachment to the silica surface.

6.5 Conclusion

Our study systemically investigated the effect of approach velocity and interfacial tension on the film drainage process between bitumen droplets with a wide viscosity range (0.009 to 283 Pa·s) and a hydrophobic silica wafer using the DFA. For the bitumen with comparable viscosity with the aqueous solution, the evolution of the film drainage process was perfectly predicted by the SRYL model. For the high-viscosity bitumen drop, the film drainage process exhibited different features, which were explained by the competition between the viscous normal stress and the Laplace pressure. The viscous normal stress dominates the approach stage, giving rise to a reduced height of initial dimple formation with the increasing Ca_d , followed by a pointy-shape water film and an expanding and shrinking rim radius. After the drop stops moving, the viscous normal stress becomes negligible, resulting in the film drainage being controlled by the disjoining pressure and film rupture happened at the film thickness at around 100 nm.

Pure bitumen as well as solvent diluted bitumen exhibited similar film profile evolution at high temperature, indicating that viscosity is the dominant factor that affects the film drainage process. The height of dimple formation for the bitumen droplet interacting with a hydrophobic silica wafer was a function of approach velocity, bitumen/water interfacial, and also bitumen drop viscosity. It was well captured by an analytical formula, indicating that the effect of viscosity becomes dominant when the capillary number of the bitumen droplet $Ca_d > 0.1$. The attachment time between the bitumen droplet and the silica wafer was strongly affected by the approach velocity, bitumen/water interfacial tension, and bitumen viscosity. A lower approach velocity,

higher interfacial tension, and a smaller bitumen viscosity would all facilitate the attachment of bitumen droplets to the hydrophobic silica surface. Our work provides valuable information on the film drainage process between bitumen with high viscosity and a hydrophobic silica wafer, with important implications to the industrial application on the heavy oil extraction process involving high viscosity features.

Chapter 7 Conclusion and Future work

7.1 Conclusion

This study provided a systematic understanding of the entire film drainage process between deformable air bubble/oil droplet and a solid surface and its application in the oil sands extraction process. The home-made Dynamic Force Apparatus and the droplet probe AFM technique were applied to directly measure the spatiotemporal evolution of the liquid film and the interaction forces, respectively. A theoretical model based on the lubrication theory and the Young-Laplace equation was used to predict the film thickness as a function of time and the interaction force. Our study provided great implications to both science and engineering.

By applying the droplet probe AFM technique, we manipulated the interaction force between the air bubble and the bitumen coated silica wafer by adjusting the water chemistry, especially the concentration of the novel secondary processing aids, sodium citrate, and calcium chloride. The force measurement together with theoretical modeling proved that the significantly more negatively charged bitumen and air bubble surface in pure sodium citrate solution at alkane condition, leading to a stronger EDL repulsion between bubble and bitumen, was the main reason that would prevent the bubble-bitumen attachment. However, the co-presence of calcium and citrate would only have a minor effect on bubble-bitumen attachment. The Stokes-Reynolds-Young-Laplace model predicted the interaction force between bubble and bitumen very well under all conditions and it proved that the competition between the EDL force and the hydrophobic force controlled the bubble-bitumen attachment. A stability map was constructed as a function of calcium chloride and sodium citrate concentration, in which regions of attachment or non-attachment between an air bubble and bitumen surface were established.

The fundamental mechanism of how Na_3Cit modifies the zeta potential at the bitumen/water interface was revealed. Similar to Na_3Cit , ligands such as EDTA and Na_2HPO_4 that could form complexes/precipitates with metal cations, led to a more negatively charged bitumen/water interface compared to NaCl at pH 8.5. It was proved that ligands promoted the release of metal cations from bitumen which recovered the negative charges of natural surfactants from bitumen. Meanwhile, the ligands were capable of adsorbing on bitumen surfaces through outer-sphere (i.e. through H-bonding or electrostatic interaction) and inner-sphere (i.e. direct interaction with metal ions) complexation, thus making the bitumen/water interface more negatively charged.

Due to the high viscosity of bitumen, a systematic study of the film drainage process between very viscous oil drops and a solid surface in both an ideal system and a bitumen system was explored using DFA. We found a decreased dimple height with the increasing oil viscosity and a three-stage film drainage process between the high viscous oil and a solid surface, which could be explained by the competition between the viscous normal stress and the Laplace pressure inside the drop. Applying a scaling method, an analytical formula $h_d = 0.5R\sqrt{Ca_f/(1 + 2Ca_d)}$ was derived, which could perfectly predict the height of dimple formation for a wide range of drop capillary numbers in both pure and bitumen system. The modified Stokes-Reynolds-Young-Laplace model, after considering the viscous normal stress inside the Young-Laplace equation, could predict the film drainage process between a high viscous oil and a solid surface. In the bitumen system, it has been proved that the viscosity of bitumen was the dominant parameter that affected the initial stage of dimple formation. The interfacial tension, approach velocity, and viscosity affected the film lifetime and the formation of the three-phase contact line. This work provided the fundamental understanding of the physics involved in the high viscous oil drop during the film drainage process, making essential steps towards solving the overall film drainage process

between a very viscous drop and a solid surface. This work also bridges the fundamental knowledge to the real oil sands extraction applications.

7.2 Future research

Some possible future research are listed below:

- In Chapter 3, the AFM was applied to investigate the interaction force between bubble and bitumen in the Milli-Q water with different electrolytes. However, the process water in the industry always contains various ions, solid particles, and fine clays. It is worth investigating the interaction force between bubble and bitumen in the process water under various conditions using AFM.
- In Chapter 4, phosphate could lead to a more negatively charged bitumen/water interface compared with NaCl solution. However, the metal content released from bitumen to the aqueous phase did not increase in the presence of phosphate compared with NaCl. It is possible a consequence of the formation of metal-phosphate precipitates, which were removed by the filtration before the ICP-MS experiment, but the exact reason still needs to be explored.
- Our modified SRYL model in Chapter 5 is based on a scaling method. It cannot quantitatively predict the film drainage process between a very viscous oil and a solid surface. Further attention could be paid to this field to solve the entire problem.
- By applying the DFA, the film drainage process between bitumen and a hydrophobic silica wafer in NaCl solution was investigated. It is also worth investigating the effect of different ions that normally exist in the process water on the film drainage process. In addition, the effect of clay particles is also valuable to study.

References

- (1) Clark, K. A. Process and Apparatus for Separating and Treating Bituminous Sands, 1929.
- (2) Long, J.; Drelich, J.; Xu, Z.; Masliyah, J. H. Effect of Operating Temperature on Water-Based Oil Sands Processing. *Can. J. Chem. Eng.* **2007**, *85* (5), 726–738.
- (3) Masliyah, J.; Zhou, Z. J.; Xu, Z.; Czarnecki, J.; Hamza, H. Understanding Water-Based Bitumen Extraction from Athabasca Oil Sands. *Can. J. Chem. Eng.* **2004**, *82* (August), 628–654.
- (4) Wallwork, V.; Xu, Z.; Masliyah, J. Processibility of Athabasca Oil Sand Using a Laboratory Hydrot Ransport Extraction System (LHES). **2010**, *82* (August 2004), 687–695.
- (5) Masliyah, J. H.; Czarnecki, J. and Xu, Z. *Handbook on Theory and Practice on Bitumen Recovery from Athabasca Oil Sands*; 2011.
- (6) Allen, E. W. Process Water Treatment in Canada’s Oil Sands Industry: I. Target Pollutants and Treatment Objectives. *J. Environ. Eng. Sci.* **2008**, *7* (2), 123–138.
- (7) Liu, J.; Xu, Z.; Masliyah, J. Colloidal Forces between Bitumen Surfaces in Aqueous Solutions Measured with Atomic Force Microscope. *Colloids Surfaces A Physicochem. Eng. Asp.* **2005**, *260* (1–3), 217–228.
- (8) Liu, J.; Xu, Z.; Masliyah, J. Studies on Bitumen-Silica Interaction in Aqueous Solutions by Atomic Force Microscopy. *Langmuir* **2003**, *19* (9), 3911–3920.
- (9) Liu, J.; Xu, Z.; Masliyah, J. Role of Fine Clays in Bitumen Extraction from Oil Sands.

- AIChE J.* **2004**, *50* (8), 1917–1927.
- (10) Ren, S.; Masliyah, J.; Xu, Z. Studying Bitumen-Bubble Interactions Using Atomic Force Microscopy. *Colloids Surfaces A Physicochem. Eng. Asp.* **2014**, *444*, 165–172.
- (11) He, L.; Lin, F.; Li, X.; Xu, Z.; Sui, H. Effect of Solvent Addition on Bitumen-Air Bubble Attachment in Process Water. *Chem. Eng. Sci.* **2015**, *137*, 31–39.
- (12) Englert, A. H.; Ren, S.; Masliyah, J. H.; Xu, Z. Interaction Forces between a Deformable Air Bubble and a Spherical Particle of Tuneable Hydrophobicity and Surface Charge in Aqueous Solutions. *J. Colloid Interface Sci.* **2012**, *379* (1), 121–129.
- (13) Wang, L.; Xu, Z.; Masliyah, J. H. Dissipation of Film Drainage Resistance by Hydrophobic Surfaces in Aqueous Solutions. *J. Phys. Chem. C* **2013**, *117* (17), 8799–8805.
- (14) Moran, K.; Masliyah, J.; Yeung, A. Factors Affecting the Aeration of Small Bitumen Droplets. *Can. J. Chem. Eng.* **2000**, *78* (4), 625–634.
- (15) Chan, D. Y. C.; Klaseboer, E.; Manica, R. Theory of Non-Equilibrium Force Measurements Involving Deformable Drops and Bubbles. *Adv. Colloid Interface Sci.* **2011**, *165* (2), 70–90.
- (16) Zhang, X.; Manica, R.; Tchoukov, P.; Liu, Q.; Xu, Z. Effect of Approach Velocity on Thin Liquid Film Drainage between an Air Bubble and a Flat Solid Surface. *J. Phys. Chem. C* **2017**, *121* (10), 5573–5584.
- (17) Zhang, X.; Manica, R.; Tang, Y.; Liu, Q.; Xu, Z. Bubbles with Tunable Mobility of Surfaces in Ethanol-NaCl Aqueous Solutions. *J. Colloid Interface Sci.* **2019**, *556*, 345–

351.

- (18) Ivanova, N. O.; Manica, R.; Liu, Q.; Xu, Z. Effect of Velocity, Solid Wettability, and Temperature on Drainage Dynamics of C5PeC11-in-Toluene Liquid Films between Silica and Water Droplet. *Energy and Fuels* **2020**, *34* (6), 6834–6843.
- (19) Connor, J. N.; Horn, R. G. The Influence of Surface Forces on Thin Film Drainage between a Fluid Drop and a Flat Solid. *Faraday Discuss.* **2003**, *123* (1), 193–206.
- (20) Xie, L.; Shi, C.; Cui, X.; Huang, J.; Wang, J.; Liu, Q.; Zeng, H. Probing the Interaction Mechanism between Air Bubbles and Bitumen Surfaces in Aqueous Media Using Bubble Probe Atomic Force Microscopy. *Langmuir* **2018**, *34* (3), 729–738.
- (21) Bai, T.; Grundy, J. S.; Manica, R.; Li, M.; Liu, Q. Controlling the Interaction Forces between an Air Bubble and Oil with Divalent Cations and Sodium Citrate. *J. Phys. Chem. C* **2020**, *124* (32), 17622–17631.
- (22) Xiang, B.; Truong, N. T. V.; Feng, L.; Bai, T.; Qi, C.; Liu, Q. Study of the Role of Sodium Citrate in Bitumen Liberation. *Energy and Fuels* **2019**, *33* (9), 8271–8278.
- (23) Hutter, J. L.; Bechhoefer, J. Calibration of Atomic-Force Microscope Tips. *Rev. Sci. Instrum.* **1993**, *64* (7), 1868–1873.
- (24) Ducker, W. A.; Xu, Z.; Israelachvili, J. N. Measurements of Hydrophobic and DLVO Forces in Bubble–Surface Interactions in Aqueous Solutions. *Langmuir* **1994**, *10* (9), 3279–3289.
- (25) Sili Ren, Hongying Zhao, Jun Long, Zhenghe Xu, and J. M. Understanding Weathering of Oil Sands Ores by Atomic Force Microscopy. *AIChE J.* **2009**, *556* (12), 3277–3285.

- (26) Liu, J.; Xu, Z.; Masliyah, J. Interaction Forces in Bitumen Extraction from Oil Sands. *J. Colloid Interface Sci.* **2005**, *287* (2), 507–520.
- (27) Chan, D. Y. C.; Klaseboer, E.; Manica, R. Film Drainage and Coalescence between Deformable Drops and Bubbles. *Soft Matter* **2011**, *7* (6), 2235–2264.
- (28) Vakarelski, I. U.; Manica, R.; Tang, X.; O’Shea, S. J.; Stevens, G. W.; Grieser, F.; Dagastine, R. R.; Chan, D. Y. C. Dynamic Interactions between Microbubbles in Water. *Proc. Natl. Acad. Sci. U. S. A.* **2010**, *107* (25), 11177–11182.
- (29) Dagastine, R. R.; Manica, R.; Carnie, S. L.; Chan, D. Y. C.; Stevens, G. W.; Grieser, F. Dynamic Forces between Two Deformable Oil Droplets in Water. *Science (80-.)*. **2006**, *313* (5784), 210–213.
- (30) Shi, C.; Zhang, L.; Xie, L.; Lu, X.; Liu, Q.; He, J.; Mantilla, C. A.; Van Den Berg, F. G. A.; Zeng, H. Surface Interaction of Water-in-Oil Emulsion Droplets with Interfacially Active Asphaltenes. *Langmuir* **2017**, *33* (5), 1265–1274.
- (31) Shi, C.; Zhang, L.; Xie, L.; Lu, X.; Liu, Q.; Mantilla, C. A.; Van Den Berg, F. G. A.; Zeng, H. Interaction Mechanism of Oil-in-Water Emulsions with Asphaltenes Determined Using Droplet Probe AFM. *Langmuir* **2016**, *32* (10), 2302–2310.
- (32) Feng, L.; Manica, R.; Grundy, J. S.; Liu, Q. Unraveling Interaction Mechanisms between Molybdenite and a Dodecane Oil Droplet Using Atomic Force Microscopy. *Langmuir* **2019**, *35* (18), 6024–6031.
- (33) Shi, C.; Cui, X.; Xie, L.; Liu, Q.; Chan, D. Y. C.; Israelachvili, J. N.; Zeng, H. Measuring Forces and Spatiotemporal Evolution of Thin Water Films between an Air Bubble and

- Solid Surfaces of Different Hydrophobicity. *ACS Nano* **2015**, *9* (1), 95–104.
- (34) Mettu, S.; Berry, J. D.; Dagastine, R. R. Charge and Film Drainage of Colliding Oil Drops Coated with the Nonionic Surfactant C12E5. *Langmuir* **2017**, *33* (20), 4913–4923.
- (35) Contreras-Naranjo, J. C.; Ugaz, V. M. A Nanometre-Scale Resolution Interference-Based Probe of Interfacial Phenomena between Microscopic Objects and Surfaces. *Nat. Commun.* **2013**, *4* (May).
- (36) Parkinson, L.; Ralston, J. The Interaction between a Very Small Rising Bubble and a Hydrophilic Titania Surface. *J. Phys. Chem. C* **2010**, *114* (5), 2273–2281.
- (37) Karakashev, S. I.; Manev, E. D. Hydrodynamics of Thin Liquid Films: Retrospective and Perspectives. *Adv. Colloid Interface Sci.* **2015**, *222*, 398–412.
- (38) Velev O. D.; Constantinides G. N.; Avraam D. G.; Payatakes A. C.; Borwankar R. P. Investigation of Thin Liquid Films of Small Diameters and High Capillary Pressures by a Miniaturized Cell.Pdf. *J. Colloid Interface Sci.* **1995**, *175*, 68–76.
- (39) Niecikowska, A.; Krasowska, M.; Ralston, J.; Malysa, K. Role of Surface Charge and Hydrophobicity in the Three-Phase Contact Formation and Wetting Film Stability under Dynamic Conditions. *J. Phys. Chem. C* **2012**, *116* (4), 3071–3078.
- (40) Zhang, X.; Tchoukov, P.; Manica, R.; Wang, L.; Liu, Q.; Xu, Z. Simultaneous Measurement of Dynamic Force and Spatial Thin Film Thickness between Deformable and Solid Surfaces by Integrated Thin Liquid Film Force Apparatus. *Soft Matter* **2016**, *12* (44), 9105–9114.
- (41) Zhang, X.; Manica, R.; Tang, Y.; Tchoukov, P.; Liu, Q.; Xu, Z. Probing Boundary

- Conditions at Hydrophobic Solid-Water Interfaces by Dynamic Film Drainage Measurement. *Langmuir* **2018**, *34* (40), 12025–12035.
- (42) Liu, B.; Manica, R.; Zhang, X.; Bussonnière, A.; Xu, Z.; Xie, G.; Liu, Q. Dynamic Interaction between a Millimeter-Sized Bubble and Surface Microbubbles in Water. *Langmuir* **2018**, *34* (39), 11667–11675.
- (43) Liu, B.; Manica, R.; Liu, Q.; Klaseboer, E.; Xu, Z.; Xie, G. Coalescence of Bubbles with Mobile Interfaces in Water. *Phys. Rev. Lett.* **2019**, *122* (19), 1–5.
- (44) Neto, C.; Evans, D. R.; Bonaccorso, E.; Butt, H. J.; Craig, V. S. J. Boundary Slip in Newtonian Liquids: A Review of Experimental Studies. *Reports Prog. Phys.* **2005**, *68* (12), 2859–2897.
- (45) Vinogradova, O. I. Drainage of a Thin Liquid Film Confined between Hydrophobic Surfaces. *Langmuir* **1995**, *11* (1), 2213–2220.
- (46) Vinogradova, O. I. Slippage of Water over Hydrophobic Surfaces. *Int. J. Miner. Process.* **1999**, *56* (1–4), 31–60.
- (47) Bai, T.; Manica, R.; Liu, B.; Klaseboer, E.; Xu, Z.; Liu, Q. Water Film Drainage between a Very Viscous Oil Drop and a Mica Surface. *Phys. Rev. Lett.* **2021**, *127* (12), 124503.
- (48) Langevin, D. Bubble Coalescence in Pure Liquids and in Surfactant Solutions. *Curr. Opin. Colloid Interface Sci.* **2015**, *20* (2), 92–97.
- (49) Amarouchene, Y.; Cristobal, G.; Kellay, H. Noncoalescing Drops. *Phys. Rev. Lett.* **2001**, *87* (20), 206104-1-206104-4.

- (50) Klaseboer, E.; Chevaillier, J. P.; Gourdon, C.; Masbernat, O. Film Drainage between Colliding Drops at Constant Approach Velocity: Experiments and Modeling. *J. Colloid Interface Sci.* **2000**, *229* (1), 274–285.
- (51) Klaseboer, E.; Manica, R.; Chan, D. Y. C. Universal Behavior of the Initial Stage of Drop Impact. *Phys. Rev. Lett.* **2014**, *113* (19), 1–5.
- (52) Manica, R.; Connor, J. N.; Carnie, S. L.; Horn, R. G.; Chan, D. Y. C. Dynamics of Interactions Involving Deformable Drops: Hydrodynamic Dimpling under Attractive and Repulsive Electrical Double Layer Interactions. *Langmuir* **2007**, *23* (2), 626–637.
- (53) Tabor, R. F.; Manica, R.; Chan, D. Y. C.; Grieser, F.; Dagastine, R. R. Repulsive Van Der Waals Forces in Soft Matter: Why Bubbles Do Not Stick to Walls. *Phys. Rev. Lett.* **2011**, *106* (6), 1–4.
- (54) Butt, H. J.; Cappella, B.; Kappl, M. Force Measurements with the Atomic Force Microscope: Technique, Interpretation and Applications. *Surf. Sci. Rep.* **2005**, *59* (1–6), 1–152.
- (55) Carnie, S. L.; Chan, D. Y. C. Interaction Free Energy between Plates with Charge Regulation: A Linearized Model. *Journal of Colloid And Interface Science.* 1993, pp 260–264.
- (56) Israelachvili, J.; Pashley, R. The Hydrophobic Interaction Is Long Range, Decaying Exponentially with Distance (Israelachvili and Pashley, 1982).Pdf. *Nature* **1982**, *300* (November), 341–342.
- (57) Clark, K. A. and P. D. S. Hot Water Separation of Bitumen from Alberta Bituminous

- Sand. *Ind. Eng. Chem. Res.* **1923**, *24*, 1410–1416.
- (58) Schramm, L. L.; Smith, R. G. Two Classes of Anionic Surfactants and Their Significance in Hot Water Processing of Oil Sands. *Can. J. Chem. Eng.* **1987**, *65* (5), 799–811.
- (59) Li, H.; Zhou, Z. A.; Xu, Z.; Masliyah, J. H. Role of Acidified Sodium Silicate in Low Temperature Bitumen Extraction from Poor-Processing Oil Sand Ores. *Ind. Eng. Chem. Res.* **2005**, *44* (13), 4753–4761.
- (60) Long, J. and Gu, Y. J. Sodium Citrate and Caustic as Process Aids for the Extraction of Bitumen from Mined Oil Sands.
- (61) Xiang, B.; Li, R.; Liu, B.; Manica, R.; Liu, Q. Effect of Sodium Citrate and Calcium Ions on the Spontaneous Displacement of Heavy Oil from Quartz Surfaces. *J. Phys. Chem. C* **2020**, *124* (38), 20991–20997.
- (62) Gan, W.; Liu, Q. Coagulation of Bitumen with Kaolinite in Aqueous Solutions Containing Ca^{2+} , Mg^{2+} and Fe^{3+} : Effect of Citric Acid. *J. Colloid Interface Sci.* **2008**, *324* (1–2), 85–91.
- (63) Gan, W.; Crozier, B.; Liu, Q. Effect of Citric Acid on Inhibiting Hexadecane-Quartz Coagulation in Aqueous Solutions Containing Ca^{2+} , Mg^{2+} and Fe^{3+} Ions. *Int. J. Miner. Process.* **2009**, *92* (1–2), 84–91.
- (64) Wang, Y.; Ahmed Khoso, S.; Luo, X.; Tian, M. Understanding the Depression Mechanism of Citric Acid in Sodium Oleate Flotation of Ca^{2+} -Activated Quartz: Experimental and DFT Study. *Miner. Eng.* **2019**, *140* (March), 105878.
- (65) He, L.; Lin, F.; Li, X.; Xu, Z.; Sui, H. Enhancing Bitumen Liberation by Controlling the

- Interfacial Tension and Viscosity Ratio through Solvent Addition. *Energy and Fuels* **2014**, 28 (12), 7403–7410.
- (66) Mehrotra, A. K. Viscosity of Cold Lake Bitumen and Its Fractions. *Can. J. Chem. Eng.* **1990**, 68 (2), 348–348.
- (67) Mehrotra, A. K.; Svrcek, W. Y. Viscosity of Compressed Athabasca Bitumen. *Can. J. Chem. Eng.* **1986**, 64 (October), 844–847.
- (68) Luo, P.; Gu, Y. Effects of Asphaltene Content on the Heavy Oil Viscosity at Different Temperatures. *Fuel* **2007**, 86 (7–8), 1069–1078.
- (69) Long, J.; Drelich, J.; Xu, Z.; Masliyah, J. H. Effect of Operating Temperature on Water-Based Oil Sands Processing. *Canadian Journal of Chemical Engineering*. 2007, pp 726–738.
- (70) Drelich, J. Wetting Phenomena in Oil Sand Systems and Their Impact on the Water-Based Bitumen Extraction Process. *Miner. Metall. Process.* **2008**, 25 (1), 1–12.
- (71) Khristov, K.; Taylor, S. D.; Czarnecki, J.; Masliyah, J. Thin Liquid Film Technique - Application to Water-Oil-Water Bitumen Emulsion Films. *Colloids Surfaces A Physicochem. Eng. Asp.* **2000**, 174 (1–2), 183–196.
- (72) Kimbler, O. K.; Reed, R. L.; Silberberg, I. H. Physical Characteristics of Natural Films Formed at Crude Oil-Water Interfaces. *Soc. Pet. Eng. J.* **1966**, 6 (02), 153–165.
- (73) Moran, K.; Sumner, R. J. Aging Effects on Surface Properties and Coalescence of Bitumen Droplets. *Can. J. Chem. Eng.* **2007**, 85 (5), 643–653.

- (74) Niu, Z.; Manica, R.; Li, Z.; He, X.; Sjoblom, J.; Xu, Z. Interfacial Properties Pertinent to W/O and O/W Emulsion Systems Prepared Using Polyaromatic Compounds. *Colloids Surfaces A Physicochem. Eng. Asp.* **2019**, *575* (May), 283–291.
- (75) Dabros, T.; Czarnecki, J. On the Interfacial Properties of Micrometre-Sized. *Proc. R. Soc. Lond. A* **1999**, *455*, 3709–3723.
- (76) Tchoukov, P.; Yang, F.; Xu, Z.; Dabros, T.; Czarnecki, J.; Sjöblom, J. Role of Asphaltenes in Stabilizing Thin Liquid Emulsion Films. *Langmuir* **2014**, *30* (11), 3024–3033.
- (77) Kuznicki, N. P.; Harbottle, D.; Masliyah, J.; Xu, Z. Dynamic Interactions between a Silica Sphere and Deformable Interfaces in Organic Solvents Studied by Atomic Force Microscopy. *Langmuir* **2016**, *32* (38), 9797–9806.
- (78) Guillaume Stirnemann, Peter J. Rossky, J. T. H. and D. L. Water Reorientation, Hydrogen-Bond Dynamics and 2D-IR Spectroscopy next to an Extended Hydrophobic Surface. *Faraday Discuss.* **2010**, *146*, 13–18.
- (79) Despa, F.; Berry, R. S. The Origin of Long-Range Attraction between Hydrophobes in Water. *Biophys. J.* **2007**, *92* (2), 373–378.
- (80) Djikaev, Y. S.; Ruckenstein, E. A Probabilistic Approach to the Effect of Hydrogen Bonding on the Hydrophobic Attraction. *J. Chem. Phys.* **2009**, *130* (12).
- (81) Cui, X.; Liu, J.; Xie, L.; Huang, J.; Liu, Q.; Israelachvili, J. N.; Zeng, H. Modulation of Hydrophobic Interaction by Mediating Surface Nanoscale Structure and Chemistry, Not Monotonically by Hydrophobicity. *Angew. Chemie* **2018**, *130* (37), 12079–12084.

- (82) Liu, J.; Cui, X.; Xie, L.; Huang, J.; Zhang, L.; Liu, J.; Wang, X.; Wang, J.; Zeng, H. Probing Effects of Molecular-Level Heterogeneity of Surface Hydrophobicity on Hydrophobic Interactions in Air/Water/Solid Systems. *J. Colloid Interface Sci.* **2019**, *557*, 438–449.
- (83) Meyer, E. E.; Lin, Q.; Hassenkam, T.; Oroudjev, E.; Israelachvili, J. N. Origin of the Long-Range Attraction between Surfactant-Coated Surfaces. *Proc. Natl. Acad. Sci. U. S. A.* **2005**, *102* (19), 6839–6842.
- (84) Tsao, Y. H.; Yang, S. X.; Evans, D. F.; Wennerström, H. Interactions between Hydrophobic Surfaces. Dependence on Temperature and Alkyl Chain Length. *Langmuir* **1991**, *7* (12), 3154–3159.
- (85) Christenson, H. K.; Claesson, P. M. Cavitation and the Interaction between Macroscopic Hydrophobic Surfaces. *Science (80-.)*. **1988**, *239* (4838), 390–392.
- (86) Palmer, L. A.; Cookson, D.; Lamb, R. N. The Relationship between Nanobubbles and the Hydrophobic Force. *Langmuir* **2011**, *27* (1), 144–147.
- (87) Wang, J.; Yoon, R. H.; Eriksson, J. C. Excess Thermodynamic Properties of Thin Water Films Confined between Hydrophobized Gold Surfaces. *J. Colloid Interface Sci.* **2011**, *364* (1), 257–263.
- (88) Pan, L.; Jung, S.; Yoon, R. H. Effect of Hydrophobicity on the Stability of the Wetting Films of Water Formed on Gold Surfaces. *J. Colloid Interface Sci.* **2011**, *361* (1), 321–330.
- (89) Lin, F.; Esmacili, P.; Long, J.; Bara, B.; Yeung, A. Random Charge Variations at the

- Bitumen-Water Interface: Characterization by Autocorrelation. *Colloids Surfaces A Physicochem. Eng. Asp.* **2014**, *451* (1), 144–150.
- (90) Drelich, J.; Long, J.; Yeung, A. Determining Surface Potential of the Bitumen-Water Interface at Nanoscale Resolution Using Atomic Force Microscopy. *Can. J. Chem. Eng.* **2008**, *85* (5), 625–634.
- (91) Freer, E. M.; Wong, H.; Radke, C. J. Oscillating Drop/Bubble Tensiometry: Effect of Viscous Forces on the Measurement of Interfacial Tension. *J. Colloid Interface Sci.* **2005**, *282* (1), 128–132.
- (92) Song, S.; Zhang, X.; Yang, B.; Lopez-Mendoza, A. Flotation of Molybdenite Fines as Hydrophobic Agglomerates. *Sep. Purif. Technol.* **2012**, *98*, 451–455.
- (93) Mao, L.; Yoon, R. H. Predicting Flotation Rates Using a Rate Equation Derived from First Principles. *Int. J. Miner. Process.* **1997**, *51* (1–4), 171–181.
- (94) Derjaguin, B.; Landau, L. Theory of the Stability of Strongly Charged Lyophobic Sols and of the Adhesion of Strongly Charged Particles in Solutions of Electrolytes. *Prog. Surf. Sci.* **1993**, *43* (1–4), 30–59.
- (95) Israelachvili, J. N. Intermolecular and Surface Forces. *Intermol. Surf. Forces* **2011**, iii.
- (96) Sanford, E. C.; Seyer, F. A. Processibility of Athabasca Tar Sand Using a Batch Extraction Unit: The Role of NaOH. *CIM Bull* **1979**, *72* (803), 164–169.
- (97) Takamura, K.; Chow, R. S. The Electric Properties of the Bitumen/Water Interface Part II. Application of the Ionizable Surface-Group Model. *Colloids and Surfaces* **1985**, *15* (C), 35–48.

- (98) Li, H.; Long, J.; Xu, Z.; Masliyah, J. H. Synergetic Role of Polymer Flocculant in Low-Temperature Bitumen Extraction and Tailings Treatment. *Energy and Fuels* **2005**, *19* (3), 936–943.
- (99) Klaseboer, E.; Chan, D. Y. C. On the Derivation of the Smoluchowski Result of Electrophoretic Mobility. *J. Colloid Interface Sci.* **2020**, *568*, 176–184.
- (100) Gustafsson, J. P. Visual MINTEQ, 3.1. *KTH Stock. Sweden* **2019**.
- (101) Jacobs, F. S.; Filby, R. H. Solvent Extraction of Oil-Sand Components for Determination of Trace Elements by Neutron Activation Analysis. *Anal. Chem.* **1983**, *55* (1), 74–77.
- (102) Laredo, G. C.; López, C. R.; Álvarez, R. E.; Cano, J. L. Naphthenic Acids, Total Acid Number and Sulfur Content Profile Characterization in Isthmus and Maya Crude Oils. *Fuel* **2004**, *83* (11–12), 1689–1695.
- (103) Ballard, D. A.; Qiao, P.; Cattoz, B.; Dowding, P. J.; Prevost, S.; Alshamsi, M.; Charpentier, T.; Roberts, K. J.; Xu, Z.; Harbottle, D. Aggregation Behavior of E-SARA Asphaltene Fractions Studied by Small-Angle Neutron Scattering. *Energy and Fuels* **2020**, *34* (6), 6894–6903.
- (104) Nivitha, M. R.; Prasad, E.; Krishnan, J. M. Ageing in Modified Bitumen Using FTIR Spectroscopy. *Int. J. Pavement Eng.* **2016**, *17* (7), 565–577.
- (105) Hennig, A.; Hoffmann, A.; Borcherding, H.; Thiele, T.; Schedler, U.; Resch-Genger, U. Simple Colorimetric Method for Quantification of Surface Carboxy Groups on Polymer Particles. *Anal. Chem.* **2011**, *83* (12), 4970–4974.
- (106) Butt, H. J.; Graf, K.; Kappl, M. *Physics and Chemistry of Interfaces*, 3rd ed.; John Wiley

& Sons: New York, 2013.

- (107) Chow, R. S.; Takamura, K. Electrophoretic Mobilities of Bitumen and Conventional Crude-in-Water Emulsions Using the Laser Doppler Apparatus in the Presence of Multivalent Cations. *J. Colloid Interface Sci.* **1988**, *125* (1), 212–225.
- (108) Zhou, J. Z.; Li, H.; Chow, R. S.; Liu, Q.; Xu, Z.; Masliyah, J. Role of Mineral Flotation Technology in Improving Bitumen Extraction from Mined Athabasca Oil Sands—II. Flotation Hydrodynamics of Water-Based Oil Sand Extraction. *Can. J. Chem. Eng.* **2020**, *98* (1), 330–352.
- (109) Ng, S.; Warszynski, P.; Zembala, M.; Malysa, K. Bitumen-Air Aggregates Flow to Froth Layer: I. Method of Analysis. *Miner. Eng.* **2000**, *13* (14–15), 1505–1517.
- (110) Ciavatta, L.; De Tommaso, G.; Iuliano, M. The Solubility of Calcium Citrate Hydrate in Sodium Perchlorate Solutions. *Anal. Lett.* **2001**, *34* (6), 1053–1062.
- (111) Vavrusova, M.; Skibsted, L. H. Aqueous Solubility of Calcium Citrate and Interconversion between the Tetrahydrate and the Hexahydrate as a Balance between Endothermic Dissolution and Exothermic Complex Formation. *Int. Dairy J.* **2016**, *57*, 20–28.
- (112) Dai, Q.; Chung, K. H. Bitumen-Sand Interaction in Oil Sand Processing. *Fuel* **1995**, *74* (12), 1858–1864.
- (113) Ma, J. Bitumen Spreading over an Air Bubble in Water. *Fuel* **2021**, *288* (November 2020), 119671.
- (114) Jada, A.; Salou, M. Effects of the Asphaltene and Resin Contents of the Bitumens on the

- Water-Bitumen Interface Properties. *J. Pet. Sci. Eng.* **2002**, *33* (1–3), 185–193.
- (115) Long, J.; Gu, Y. J. Sodium Citrate and Caustic as Process Aids for the Extraction of Bitumen from Mined Oil Sands. Google Patents October 2016.
- (116) Prado, G. H. C.; De Klerk, A. Metals Removal from Metal-Bridged Molecules by Acid Treatment of Oilsands Bitumen and Subfractions. *Energy and Fuels* **2016**, *30* (1), 20–30.
- (117) Francis, A. J.; Dodge, C. J.; Gillow, J. B. Biodegradation of Metal Citrate Complexes and Implications for Toxic-Metal Mobility. *Nature* **1992**, *356* (6365), 140–142.
- (118) Zhang, Y.; Cremer, P. S. Interactions between Macromolecules and Ions: The Hofmeister Series. *Curr. Opin. Chem. Biol.* **2006**, *10* (6), 658–663.
- (119) Salgin, S.; Salgin, U.; Bahadir, S. Zeta Potentials and Isoelectric Points of Biomolecules: The Effects of Ion Types and Ionic Strengths. *Int. J. Electrochem. Sci.* **2012**, *7* (12), 12404–12414.
- (120) Collins, K. D.; Washabaugh, M. W. The Hofmeister Effect and the Behaviour of Water at Interfaces. *Q. Rev. Biophys.* **1985**, *18* (4), 323–422.
- (121) Li, X.; Zhai, J.; Xie, X. The Hofmeister Anion Effect on Ionophore-Based Ion-Selective Nanospheres Containing Solvatochromic Dyes. *Electroanalysis* **2020**, *32* (4), 749–754.
- (122) Federation, W. E.; Association, A. P. H. Standard Methods for the Examination of Water and Wastewater. *Am. Public Heal. Assoc. Washington, DC, USA* **2005**.
- (123) Xiang, B.; Liu, Q.; Long, J. Probing Bitumen Liberation by a Quartz Crystal Microbalance with Dissipation. *Energy & fuels* **2018**, *32* (7), 7451–7457.

- (124) Yang, Q.; Ke, D.; Yang, M.; Hong, J.; Ran, Q.; Wang, X. Effect of Salt Concentration on the Phase Separation of Bitumen Emulsions. *Colloids Surfaces A Physicochem. Eng. Asp.* **2013**, *425*, 1–5.
- (125) Bonto, M.; Eftekhari, A. A.; Nick, H. M. An Overview of the Oil-Brine Interfacial Behavior and a New Surface Complexation Model. *Sci. Rep.* **2019**, *9* (1), 1–16.
- (126) Parra-Barraza, H.; Hernández-Montiel, D.; Lizardi, J.; Hernández, J.; Urbina, R. H.; Valdez, M. A. The Zeta Potential and Surface Properties of Asphaltenes Obtained with Different Crude Oil/n-Heptane Proportions. *Fuel* **2003**, *82* (8), 869–874.
- (127) Weigel, S.; Stephan, D. The Prediction of Bitumen Properties Based on FTIR and Multivariate Analysis Methods. *Fuel* **2017**, *208*, 655–661.
- (128) Lackovic, K.; Johnson, B. B.; Angove, M. J.; Wells, J. D. Modeling the Adsorption of Citric Acid onto Muloorina Illite and Related Clay Minerals. *J. Colloid Interface Sci.* **2003**, *267* (1), 49–59.
- (129) Kang, S.; Xing, B. Adsorption of Dicarboxylic Acids by Clay Minerals as Examined by in Situ ATR-FTIR and Ex Situ DRIFT. *Langmuir* **2007**, *23* (13), 7024–7031.
- (130) Lanigan, K. C.; Pidosny, K. Reflectance FTIR Spectroscopic Analysis of Metal Complexation to EDTA and EDDS. *Vib. Spectrosc.* **2007**, *45* (1), 2–9.
- (131) Arai, Y.; Sparks, D. L. ATR-FTIR Spectroscopic Investigation on Phosphate Adsorption Mechanisms at the Ferrihydrite-Water Interface. *J. Colloid Interface Sci.* **2001**, *241* (2), 317–326.
- (132) Elzinga, E. J.; Sparks, D. L. Phosphate Adsorption onto Hematite: An in Situ ATR-FTIR

- Investigation of the Effects of PH and Loading Level on the Mode of Phosphate Surface Complexation. *J. Colloid Interface Sci.* **2007**, *308* (1), 53–70.
- (133) Strausz, O. P.; Lown, E. M. *The Chemistry of Alberta Oil Sands, Bitumens and Heavy Oils*; Alberta Energy Research Institute Calgary, Alberta, Canada, 2003.
- (134) Hidber, P. C.; Graule, T. J.; Gauckler, L. J. Influence of the Dispersant Structure on Properties of Electrostatically Stabilized Aqueous Alumina Suspensions. *J. Eur. Ceram. Soc.* **1997**, *17* (2–3), 239–249.
- (135) Desset-Brèthes, S.; Cabane, B.; Spalla, O. Competition between Ligands for Al₂O₃ in Aqueous Solution. *J. Phys. Chem. A* **2012**, *116* (25), 6511–6518.
- (136) Granholm, K.; Harju, L.; Ivaska, A. Desorption of Metal Ions from Kraft Pulps. Part 2. Chelation of Kraft Pulps with Different Complexing Agents and with Edta in a Reducing Environment. *BioResources* **2010**, *5*.
- (137) Markich, S. J.; Brown, P. L.; Jeffree, R. A. Divalent Metal Accumulation in Freshwater Bivalves: An Inverse Relationship with Metal Phosphate Solubility. *Sci. Total Environ.* **2001**, *275* (1–3), 27–41.
- (138) Hupka, J.; Drelich, J.; Oblad, A. G.; White, R. I. Impact of Water Recycle on Water-Based Processing of Whiterocks Tar Sand. **1991**, *70*, 1313–1316.
- (139) Drelich, J.; Miller, J. D. Surface and Interfacial Tension of the Whiterocks Bitumen and Its Relationship to Bitumen Release from Tar Sands during Hot Water Processing. *Fuel* **1994**, *73* (9), 1504–1510.
- (140) Situm, A.; Rahman, M. A.; Goldberg, S.; Al-Abadleh, H. A. Spectral Characterization and

- Surface Complexation Modeling of Low Molecular Weight Organics on Hematite Nanoparticles: Role of Electrolytes in the Binding Mechanism. *Environ. Sci. Nano* **2016**, *3* (4), 910–926.
- (141) Federal, S. Adsorption of EDTA and Metal – EDTA Complexes onto Goethite. **1996**, *121* (0011), 106–121.
- (142) Wojciechowski, K.; Bitner, A.; Warszyński, P.; Żubrowska, M. The Hofmeister Effect in Zeta Potentials of CTAB-Stabilised Toluene-in-Water Emulsions. *Colloids Surfaces A Physicochem. Eng. Asp.* **2011**, *376* (1–3), 122–126.
- (143) Dos Santos, A. P.; Levin, Y. Effective Charges and Zeta Potentials of Oil in Water Microemulsions in the Presence of Hofmeister Salts. *J. Chem. Phys.* **2018**, *148* (22).
- (144) Allan, R. S.; Charles, G. E.; Mason, S. G. The Approach of Gas Bubbles to a Gas/Liquid Interface. *J. Colloid Sci.* **1961**, *16* (2), 150–165.
- (145) Thoroddsen, S. T.; Etoh, T. G.; Takehara, K.; Ootsuka, N.; Hatsuki, Y. The Air Bubble Entrapped under a Drop Impacting on a Solid Surface. *J. Fluid Mech.* **2005**, *545*, 203–212.
- (146) Gordeev, E. G.; Galushko, A. S.; Ananikov, V. P. Improvement of Quality of 3D Printed Objects by Elimination of Microscopic Structural Defects in Fused Deposition Modeling. *PLoS One* **2018**, *13* (6).
- (147) Manica, R.; Hendrix, M. H. W.; Gupta, R.; Klaseboer, E.; Ohl, C. D.; Chan, D. Y. C. Effects of Hydrodynamic Film Boundary Conditions on Bubble-Wall Impact. *Soft Matter* **2013**, *9* (41), 9755–9758.

- (148) Langley, K.; Li, E. Q.; Thoroddsen, S. T. Impact of Ultra-Viscous Drops: Air-Film Gliding and Extreme Wetting. *J. Fluid Mech.* **2017**, *813*, 647–666.
- (149) Langley, K. R.; Thoroddsen, S. T. Gliding on a Layer of Air: Impact of a Large-Viscosity Drop on a Liquid Film. *J. Fluid Mech.* **2019**, *878*, R2.
- (150) Yiantsios, S. G.; Davis, R. H. On the Buoyancy-Driven Motion of a Drop towards a Rigid Surface or a Deformable Interface. *J. Fluid Mech.* **1990**, *217* (91), 547–573.
- (151) Bazhlekov, I. B.; Chesters, A. K.; Van De Vosse, F. N. The Effect of the Dispersed to Continuous-Phase Viscosity Ratio on Film Drainage between Interacting Drops. *Int. J. Multiph. Flow* **2000**, *26* (3), 445–466.
- (152) Davis, R. H.; Schonberg, J. A.; Rallison, J. M. The Lubrication Force between Two Viscous Drops. *Phys. Fluids A* **1989**, *1* (1), 77–81.
- (153) El-Hamouz, A. Effect of Surfactant Concentration and Operating Temperature on the Drop Size Distribution of Silicon Oil Water Dispersion. *J. Dispers. Sci. Technol.* **2007**, *28* (5), 797–804.
- (154) Gu, Y.; Li, D. Electric Charge on Small Silicone Oil Droplets Dispersed in Ionic Surfactant Solutions. *Colloids Surfaces A Physicochem. Eng. Asp.* **1998**, *139* (2), 213–225.
- (155) Nishimura, S.; Tateyama, H.; Tsunematsu, K.; Jinnai, K. Zeta Potential Measurement of Muscovite Mica Basal Plane-Aqueous Solution Interface by Means of Plane Interface Technique. *J. Colloid Interface Sci.* **1992**, *152* (2), 359–367.
- (156) Verwey E. J. W.; Overbeek J. T. G.; and Van Nes K. *Theory of the Stability of Lyophobic*

- Colloids: The Interaction of Sol Particles Having an Electric Double Layer*; Elsevier Publishing Company,; New York, 1948.
- (157) Batchelor C. K. and Batchelor G. *An Introduction to Fluid Dynamics*; Cambridge University Press: Cambridge, England, 2000.
- (158) Wang, Y.; Dhong, C.; Frechette, J. Out-of-Contact Elastohydrodynamic Deformation Due to Lubrication Forces. *Phys. Rev. Lett.* **2015**, *115* (24), 1–5.
- (159) Klaseboer, E.; Chevaillier, J. P.; Mate, A.; Masbernat, O.; Gourdon, C. Model and Experiments of a Drop Impinging on an Immersed Wall. *Phys. Fluids* **2001**, *13* (1), 45–57.
- (160) Shahalami, M.; Wang, L.; Wu, C.; Masliyah, J. H.; Xu, Z.; Chan, D. Y. C. Measurement and Modeling on Hydrodynamic Forces and Deformation of an Air Bubble Approaching a Solid Sphere in Liquids. *Adv. Colloid Interface Sci.* **2015**, *217*, 31–42.
- (161) Harjai, S. K.; Flury, C.; Masliyah, J.; Drelich, J.; Xu, Z. Robust Aqueous-Nonaqueous Hybrid Process for Bitumen Extraction from Mineable Athabasca Oil Sands. In *Energy and Fuels*; 2012; Vol. 26, pp 2920–2927.
- (162) Li, R.; Manica, R.; Yeung, A.; Xu, Z. Spontaneous Displacement of High Viscosity Micrometer Size Oil Droplets from a Curved Solid in Aqueous Solutions. *Langmuir* **2019**, *35* (3), 615–627.
- (163) Scheludko, A.; Platikanov, D. Untersuchung dünner flüssiger Schichten auf Quecksilber. *Kolloid-Zeitschrift und Zeitschrift für Polymere.* **1961**, *175*, 150.

- (164) Schramm, L. L.; Stasiuk, E. N.; Turner, D. The Influence of Interfacial Tension in the Recovery of Bitumen by Water-Based Conditioning and Flotation of Athabasca Oil Sands. *Fuel Process. Technol.* **2003**, *80* (2), 101–118.
- (165) Stasiuk, E. N.; Schramm, L. L. An Absolute Droplet Pressure Interfacial Tensiometer and Its Application to Bituminous Systems of Vanishing Density Contrast. *Colloid Polym. Sci.* **2000**, *278* (12), 1172–1179.
- (166) Drelich, J. The Role of Wetting Phenomena in the Hot Water Process for Bitumen Recovery from Tar Sand, University of Utah, 1993.
- (167) Vakarelski, I. U.; Manica, R.; Li, E. Q.; Basheva, E. S.; Chan, D. Y. C.; Thoroddsen, S. T. Coalescence Dynamics of Mobile and Immobile Fluid Interfaces. *Langmuir* **2018**, *34* (5), 2096–2108.

Appendix A

Comparison between constant potential and constant charge models

The calculated electrostatic double layer (EDL) disjoining pressures in 3 mM CaCl₂ at pH 8.5 using the numerical solution of the nonlinear Poisson-Boltzmann equation with constant potential and constant charge boundary conditions are shown in Figure A1. The results show that the difference between the EDL pressures is small when the separation distance between the air bubble and the bitumen surface was larger than 10 nm. In addition, the two curves intersect with the Laplace pressure roughly at the same point.

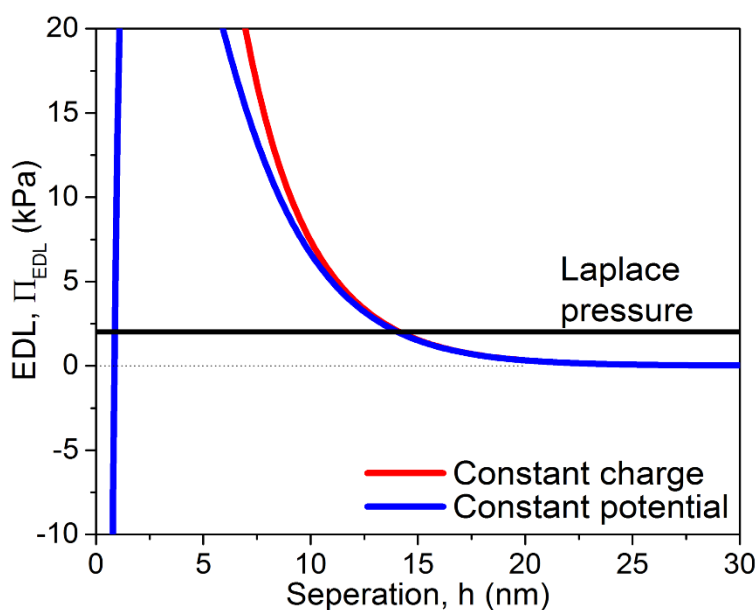


Figure A1 Comparison between the numerical solutions of the nonlinear Poisson-Boltzmann equations under constant potential and constant charge boundary conditions.

Charge at the Stern plane per unit area of bitumen droplet

The charge at the Stern plane per unit area of bitumen droplet is calculated using the zeta potentials and the Grahame equation:¹

$$\sigma = \sqrt{8c_0 \epsilon \epsilon_0 k_B T} \sinh\left(\frac{e\Psi_0}{2k_B T}\right) \quad (\text{A1})$$

where σ is the charge at the Stern plane per unit area, c_0 is the bulk concentration of electrolyte, Ψ_0 is the surface potential. It is worth noting that the surface charge is often an order of magnitude higher than that calculated from the Graham equation and the zeta potentials. The charge at the Stern plane per unit area of bitumen under difference conditions is shown in Figure A2.

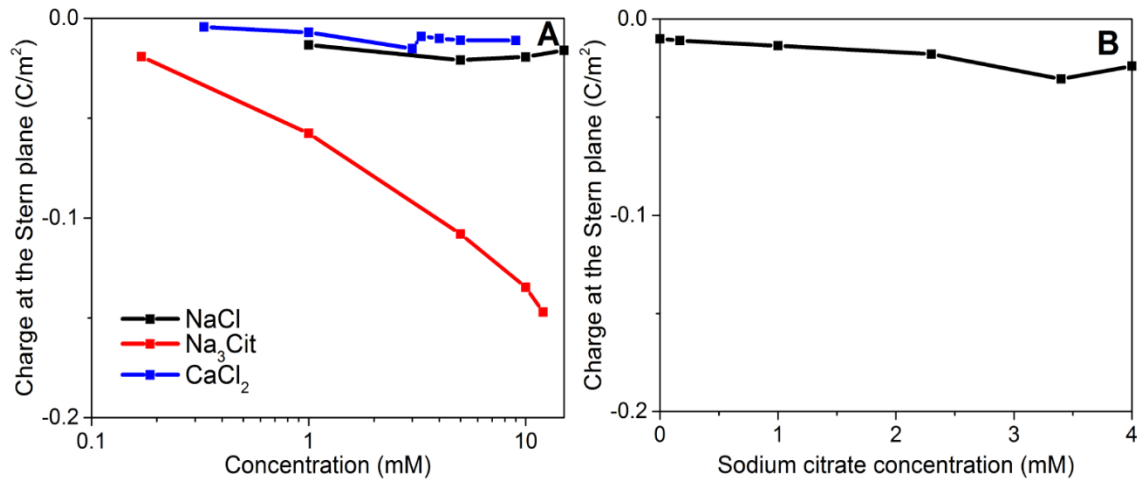


Figure A2 Charge at the Stern plane per unit area of bitumen droplets at pH 8.5 in (A) pure electrolyte solution with different concentration and (B) 4 mM CaCl₂ with different concentrations of Na₃Cit. The lines between dots are a guide to the eye.

Air/water interfacial tension and bitumen surface contact angle

The dynamic air/water interfacial tension, γ , was measured using the pendent drop method at room temperature with a Theta Optical Tensiometer T200 (Biolin Scientific, Stockholm, Sweden). The bitumen surface was immersed in the solution and the interfacial tension was monitored for 1 h. The air/water interfacial tension remained around 72.5 ± 0.6 mN/m under all experimental

conditions and did not change over time, as shown in Figure A3, which indicated no interfacial active components leached out and accumulated at the air/water interface during the experiments.

The dynamic water contact angle on a bitumen surface, θ , was measured using the captive bubble method with a Theta Optical Tensiometer T200 (Biolin Scientific, Stockholm, Sweden) for 1 h. The water contact angle on the bitumen surface was around $92 \pm 1^\circ$ and did not change over time, as shown in Figure A4. This indicated the bitumen surface was stable and would not liberate from the silica wafer during the experiments. Based on the air/water interfacial tension and the contact angle, the constant $C = \gamma(1 - \cos \theta)$ for the calculation of the HB force was determined to be 0.076 ± 0.001 N/m.

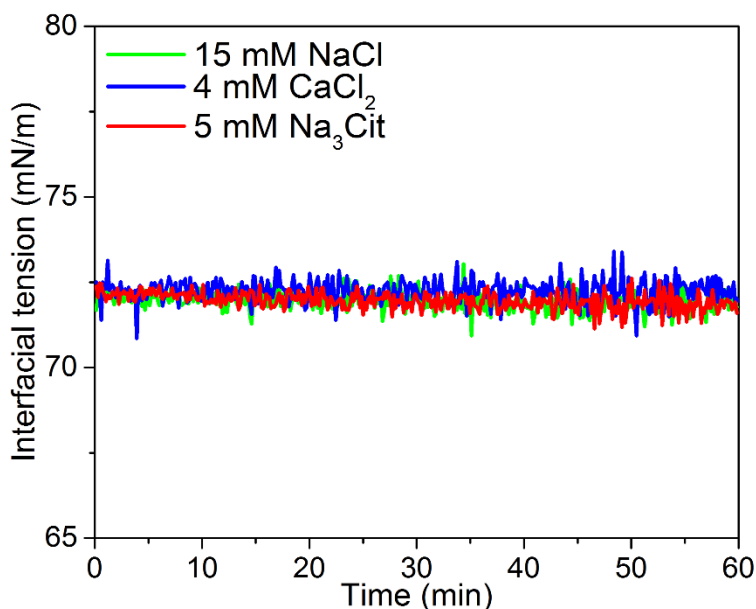


Figure A3 Air/water interfacial tension as a function of time in the presence of bitumen surface.

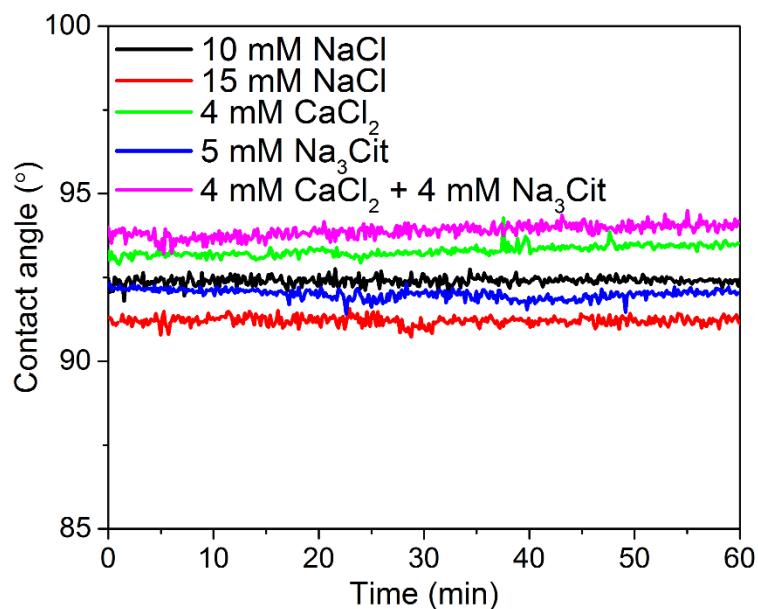


Figure A4 Water contact angle on bitumen surface as a function of time.

Reproducibility of force curves

The interaction force curves between one air bubble and bitumen surface at different positions in 5 mM Na₃Cit at pH 8.5 is shown in Figure A5. The force curves were not significantly different during the experimental time period, indicating that the experiment was reproducible and any small changes of the bubble size over time would not affect the result.

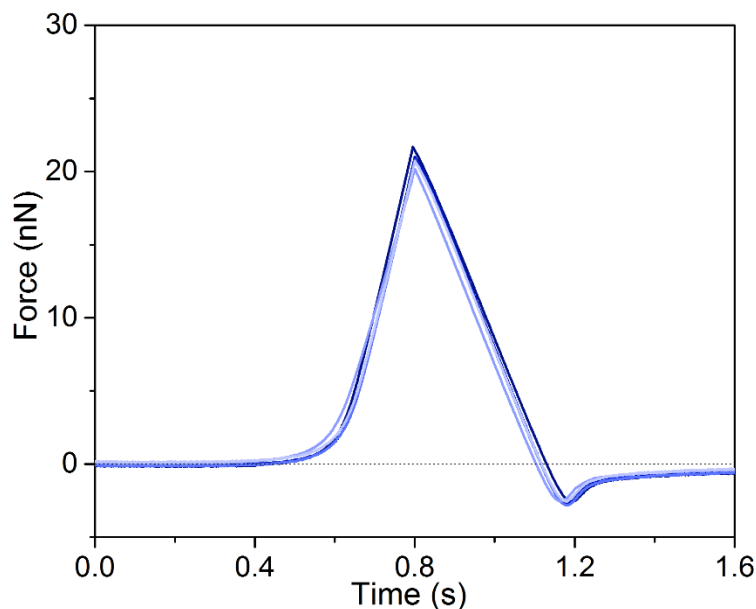


Figure A5 Interaction force between one air bubble and different positions on the bitumen surface over 30 min in 5 mM Na₃Cit at pH 8.5.

Comparison between theoretically-fitted Stern potential and measured zeta potential values of the air bubble in different electrolyte solutions

The bubble zeta potentials were measured using a Brookhaven ZetaPALS in selected solution conditions. Figure A6 shows the schematic of the experimental setup for generating nanobubble suspensions. The target solution was mixed with the injected air and entered the top of the chamber under high pressure. The air was injected at a low rate of 20 sccm/min so that all the injected air was trapped at the top of the pressurized chamber without leaving the bottom exit in the form of large bubbles. The air-saturated target solution left the chamber and passed through a Venturi tube where both the flow pressure and air-saturation level re-released, resulting in the nucleation of nano- and micro-bubbles. The bubble suspension was stabilized with 5 ppm MIBC, and MIBC was considered to have negligible influence on the bubble zeta potential.² The bubble size was measured to be around 100 nm (Measured through Malvern Zetasizer Nano ZS). A comparison of

theoretically-fitted surface potential from the SRYL model and measured zeta potential values of the air bubble in different electrolyte solutions is shown in Table A1.

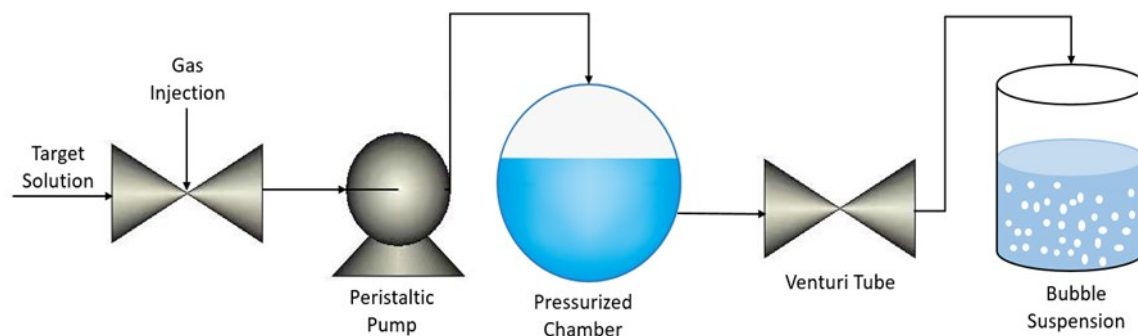


Figure A6 Schematic diagram of experimental set up of generating nanobubble suspension.

Table A1 Measured and fitted zeta potentials of the bubble. Theoretical values within the specified range provided results that were in agreement with the experiment

Electrolyte	Concentration (mM)	SRYL fitted value (mV)	Measured zeta potential (mV)	Charge at the Stern plane (C/m ²)	Literature (mV)
NaCl	10	-45 ± 2	-45 ± 5	-0.0118	-50^3 -35^4
CaCl ₂	3	-30 ± 5	---	-0.007	-20^4 -15 ± 5^5 (For 1 mM CaCl ₂)
Na ₃ Cit	5	-65 ± 10	-60 ± 5	-0.0327	---

Air bubble was negatively charge under all tested conditions. The source of negative zeta potentials on hydrophobic surfaces, such as air/water interface, is continuously debated, many researchers believe that the OH⁻ group adsorbs at the air/water interface to result in a negative charge.⁶ Others believe the negative charge of the air/water interface originates from the interfacial water dipole moment.⁷ It is worth noting that previous research found that increasing CaCl₂ concentration had minor effect on the bubble zeta potential.^{5, 8} Stern potentials experimentally measured in this work were consistent with the literature and experimental value. These values

were used in the SYRL model and provide good agreement between experimental and theoretical interaction forces.

Contributions of different surface forces in NaCl solution

Figure A7. shows the calculated components of the disjoining pressure, the overall disjoining pressure and the Laplace pressure as a function of separation between the air bubble and the bitumen surface in 10 mM NaCl and 15 mM NaCl. Results show that the EDL and vdW pressures are repulsive while the hydrophobic pressure is attractive in these cases. In 10 mM NaCl, the EDL repulsion was strong enough, as shown in Figure A7A, and the overall disjoining pressure balanced the Laplace pressure, $\frac{2\gamma}{R}$, inside the air bubble before the hydrophobic attraction became significant. As shown in Figure A7B, the EDL repulsion decreased in 15 mM NaCl compared with that in 10 mM NaCl. When the separation between air bubble and bitumen surface was around 10 nm, the hydrophobic attraction was strong enough to compensate for the repulsive of EDL and vdW pressures. This resulted in the overall disjoining pressure never exceeding the Laplace pressure inside the air bubble and induced bubble-bitumen attachment.

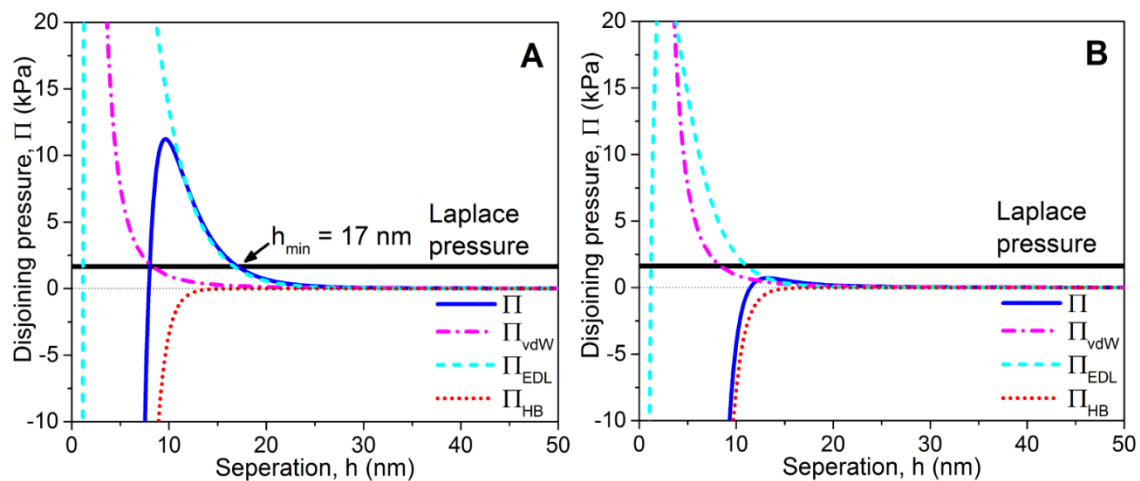


Figure A7 Contributions of disjoining pressure in (A) 10 mM NaCl and (B) 15 mM NaCl.

Contributions of different surface forces in CaCl₂ solution

The calculated components of the disjoining pressure, the overall disjoining pressure and the Laplace pressure in 3 mM CaCl₂ and 4 mM CaCl₂ are shown in Figure A8. Similarly, in 3 mM CaCl₂, the strong EDL repulsion resulted in the overall disjoining pressure exceeding the Laplace pressure, as shown in Figure A8A. The hydrophobic attraction become dominant in 4 mM CaCl₂ due to the decreased EDL repulsion, as shown in Figure A8B.

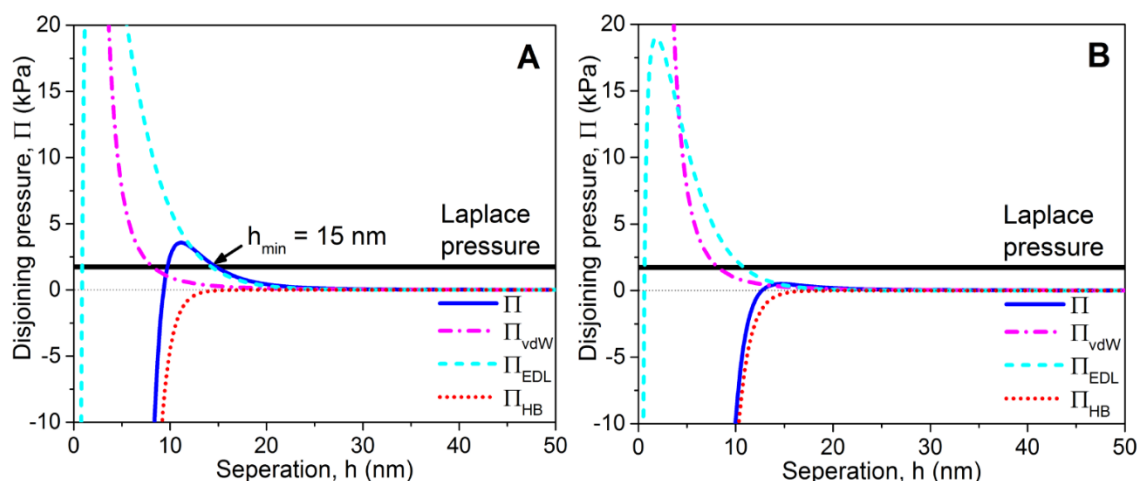


Figure A8 Contributions of disjoining pressures in (A) 3 mM CaCl₂ and (B) 4 mM CaCl₂.

Adding citrate after adsorption of Ca²⁺ to the bitumen surface

The experimental interaction force between an air bubble and a bitumen surface after initial equilibration in 4 mM CaCl₂ followed by addition of 2.3 mM Na₃Cit is shown in Figure A9. The curve shows that no bubble-bitumen attachment happens when the maximum loading force was set to 20 nN.

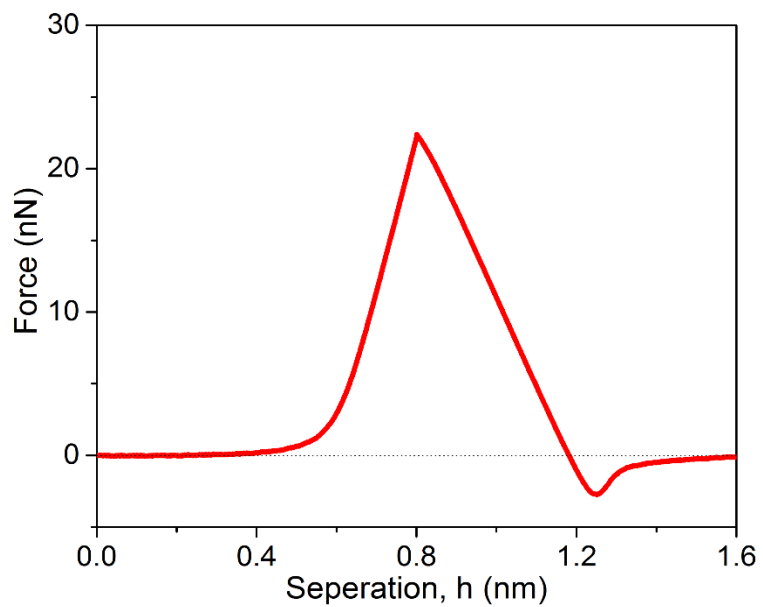


Figure A9 Interaction between air bubble and bitumen surface after initial equilibration in 4 mM

CaCl₂ solution followed by the addition of 2.3 mM Na₃Cit.

References

- (1) Butt, H. J.; Graf, K.; Kappl, M. Chapter 4. The Electrical Double Layer. *Physics and Chemistry of Interfaces*. Third, Revised and Enlarged Edition. John Wiley & Sons, 2013.
- (2) Elmahdy, A. M.; Mirnezami, M.; Finch, J. A. Zeta Potential of Air Bubbles in Presence of Frother. *Int. J. Miner. Process* **2008**, *89*, 40-43.
- (3) Li, C.; Somasundaran, P. Reversal of Bubble Charge in Multivalent Inorganic Salt Solutions-Effect of Aluminum. *J. Colloid Interface Sci.* **1992**, *148*, 587 - 591.
- (4) Yang, C.; Dabros, T.; Li, D.; Czarnecki, J.; Masliyah, J. H. Measurement of the Zeta Potential of Gas Bubbles in Aqueous Solutions by Microelectrophoresis Method. *J. Colloid Interface Sci.* **2001**, *243*, 128-135.
- (5) Wu, C.; Nasset, K.; Masliyah, J. H.; Xu, Z. Generation and Characterization of Submicron Size Bubbles. *Adv. Colloid Interface Sci.* **2012**, *179-182*, 123-132.
- (6) Yoon, R. H.; Yordan, J. L. Zeta Potential Measurements on Microbubbles Generated Using Various Surfactants. *J. Colloid Interface Sci.* **1986**, *113*, 430-438.
- (7) Vassilev, P.; Hartnig, C.; Koper, M. T. M.; Frechard, F.; van Santen, R. A. Ab initio Molecular Dynamics Simulation of Liquid Water and Water-Vapor Interface. *J. Chem. Phys.* **2001**, *115*, 9815-9820.
- (8) Han, M. Y.; Ahn, H. J.; Shin, M. S.; Kim, S. R. The Effect of Divalent Metal Ions on the Zeta Potentials of Bubbles. *Water Sci. Technol.* **2004**, *50*, 49-56.

Appendix B

Concentration of metal ions released from bitumen

Table A2 Concentration of metal ions released from bitumen

pH	Electrolyte	Concentration (mM)	Released metal ion concentration (µg/L)								
			Ba	Co	Cr	Mo	Ni	Pb	Sr	Ti	Tl
8.5	Milli-Q	-	<DL	0.6	0.6	1.5	1.2	1.4	0.5	31.8	4.8
	NaCl	10	2.9	<DL	<DL	1.1	<DL	<DL	5.4	9.4	3.1
	Na ₃ Cit	5	3.4	1.1	0.6	1.7	2.2	1.9	5.9	65.4	2.2
	EDTA	5	11.9	0.9	1.0	1.7	2.8	5.5	7.6	32.6	1.7
	Na ₂ HPO ₄	5	1.0	0.2	0.5	3.4	<DL	0.7	3.7	32.4	1.1
10.5	Milli-Q	-	<DL	<DL	0.3	6.3	<DL	<DL	<DL	8.2	0.6
	NaCl	10	2.0	<DL	0.5	6.2	<DL	<DL	7.2	1.4	0.2
	Na ₃ Cit	5	7.3	3.3	0.7	6.6	6.7	1.8	16.5	26.9	1.4
	EDTA	5	102.1	13.8	2.8	18.9	17.4	23.2	106.9	78.6	1.4
	Na ₂ HPO ₄	5	3.4	3.0	0.6	10.1	2.8	2.9	5.1	12.9	1.2

ATR-FTIR

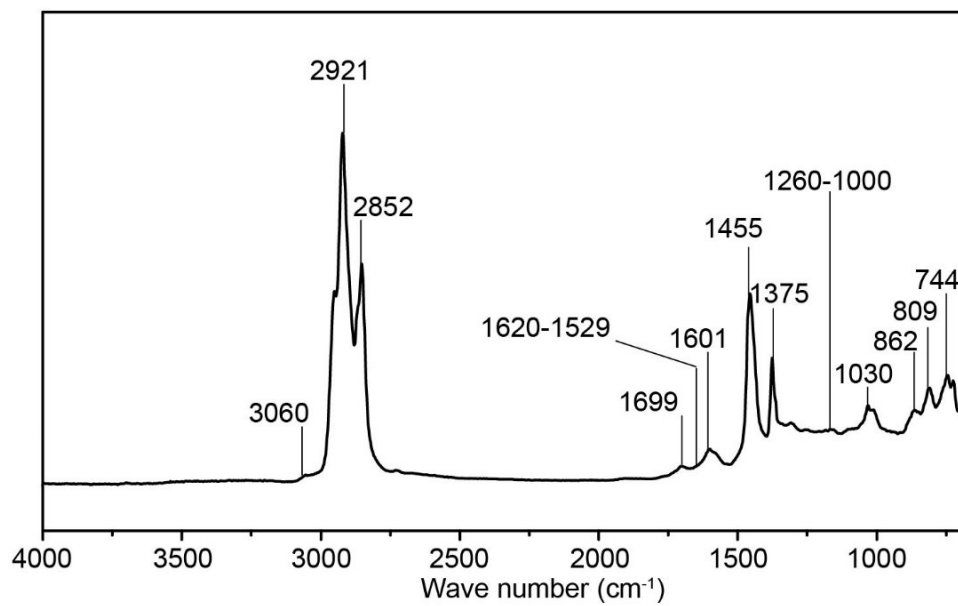


Figure A10 ATR-FTIR spectra of bitumen.

Table A3 Assignments of vibration bands of bitumen from ATR-FTIR

Wave Number (cm⁻¹)	Functional group
3060	Aromatic C-H stretching
2700-2920 (2921, 2852)	Aliphatic C-H stretching
1710-1630 (1699, 1601)	Carbonyl C=O stretching
1620-1529 (weak)	Aromatic C=C stretching
1455, 1375	Aliphatic C-H bending
1260-1000 (weak)	C-O stretching
1030	S=O stretching
862, 809, 744	Aromatic C-H stretching

Table A4 Assignments of vibration bands of EDTA solution at pH 8.5 from ATR-FTIR

Wave Number (cm⁻¹)	Functional group
1576	Asymmetric COO-
1401	Symmetric COO-
1320	COO-
1133	C-N stretching
1092	C-N stretching
977	C-C (CH ₂ COO-)
917	C-C (CH ₂ COO-)

Appendix C

The height of dimple formation

The videos were recorded at 3000, 5000 and 8000 fps for three conditions ($V = 0.1$ mm/s in 0.1 mM SDS; $V = 1.06$ mm/s in 0.1 mM SDS; $V = 1.06$ mm/s in 1 mM SDS) in order to have a more detailed analysis. A mercury light enabled the light intensity extraction for three channels (green, red and blue) which the characteristic wavelength is 546 nm, 579 nm and 436 nm. The snapshots of the interference fringes in a time sequence obtained between a mica surface and an oil drop with viscosity 68.2 Pa·s in green channel is shown in Figure A11a. The light intensity at the center point of the fringes, as shown as the red points on Figure A11a, was converted to intensity value as a function of time, shown in Figure A11b. The points which correspond to the snapshots in Figure A1a were marked as the same number. It is obvious that the light intensity evolved quickly at the very beginning and gradually slowed down from frames number 3 to 4. In addition, a flat surface was also formed at the bottom of the oil drop within the same time range and the barrier rim appears right after frame No. 4, as shown in Figure A11a. The height of dimple formation was defined as the average of the film thickness from frames 3 to 4.

The film thickness of the red point can be calculated through the light intensity by the following Eqs.¹

$$h(r, t) = \frac{\lambda}{2\pi n_2} \left(m\pi \pm \arcsin \sqrt{\frac{\Delta}{1 + 4(1 - \Delta) \frac{\sqrt{R_{12}R_{13}}}{(1 - \sqrt{R_{12}R_{23}})^2}}} \right) \quad (A2)$$

$$\Delta = \frac{I(r, t) - I_{min}}{I_{max} - I_{min}} \quad (A3)$$

$$R_{12} = \frac{(n_1 - n_2)^2}{(n_1 + n_2)^2}, R_{23} = \frac{(n_2 - n_3)^2}{(n_2 + n_3)^2} \quad (\text{A4})$$

where I is the light intensity, λ is the light wavelength and m is the interference fringe order. The refractive indices of the oil drops, aqueous solution and mica are n_1 , n_2 and n_3 , respectively. Eq. (A2) can also be simplified to:²

$$\Delta = \sin^2 \left(\frac{2\pi n_2 h(t)}{\lambda} \right) \quad (\text{A5})$$

The corresponding evolution of the film thickness at the center of symmetry is shown in Figure A11c. The green dots and the red dots represent the film thickness from green and red channels, respectively. It is worth noting that because the refractive indices of the oil drop and water are very similar, the fringes from the blue channel are hard to identify. The center heights analyzed from green and red channels agreed well with each other within the experimental error. The dimple height was obtained by taking an average of the film thickness in the shaded area and the zero time was defined as the time when dimple occurred throughout the experiments.

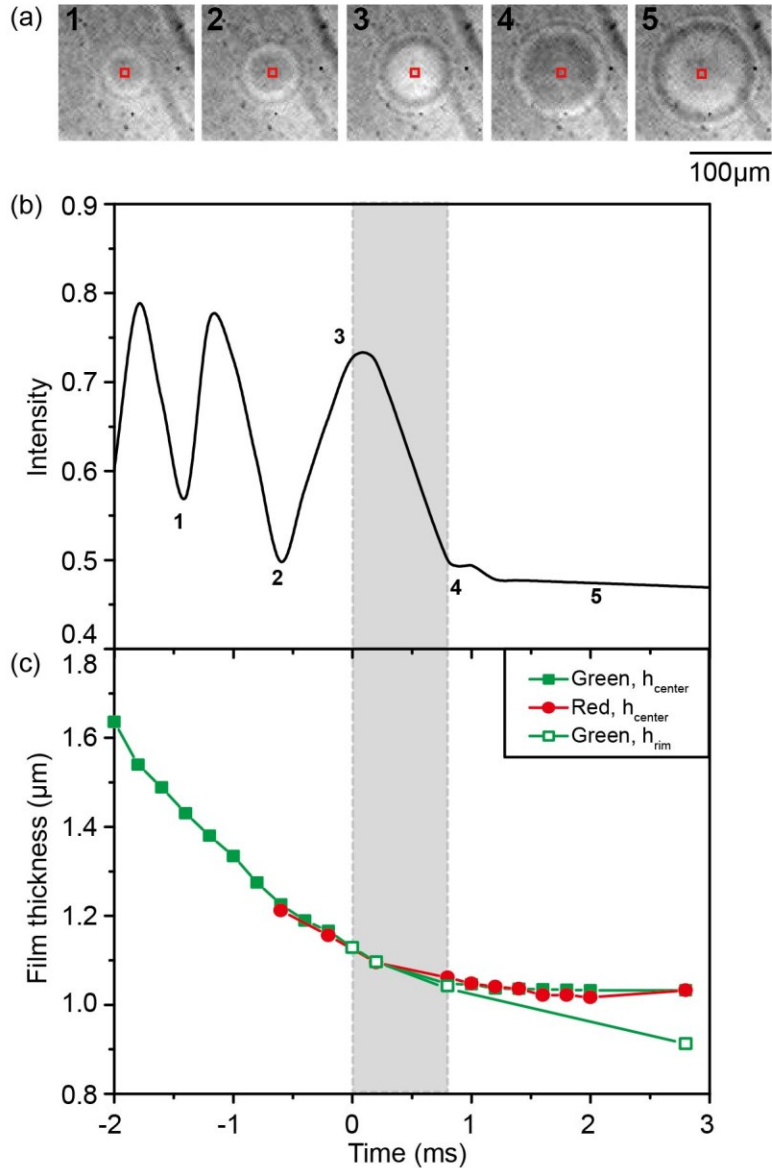


Figure A11 (a) Snapshots of the interference fringes of green channel in a time sequence obtained between an oil drop and a mica surface. ($\mu_o = 68.2 \text{ Pa}\cdot\text{s}$, $V = 1.06 \text{ mm/s}$, 0.1 mM SDS , frame rate 5000 fps) (b) Evolution of the light intensity at the film center in (a). (c) Film thickness as a function of time between the oil drop and the mica surface transferred from (b). The dimple height of this condition was obtained by taking an average of the film thickness in the shaded area.

Drive function

The displacement and velocity can be controlled by the motorized actuator (THORLABH, Z825B), which has been described in detail elsewhere.³ The actuator can provide a precise and slow displacement. The displacement of the droplet can be obtained through the side-view camera. Other than that, the displacement of the droplet can also be obtained through a laser sensor with a sensitivity of 5 μm . The displacement and the drive function of the droplet at 1.06 mm/s are shown in Figure A12.

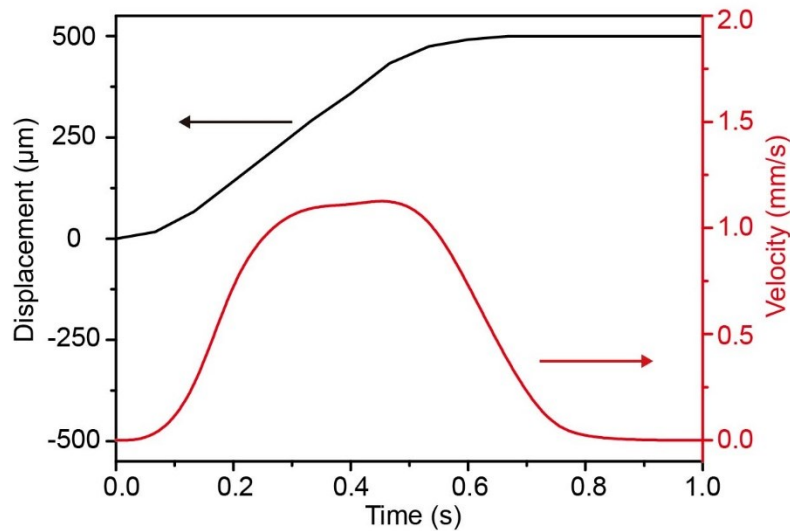


Figure A12 Displacement controlled by the motorized actuator and the real-time velocity of the oil droplet approaching the mica surface with the approach velocity of 1.06 mm/s.

Dimple height

Figure A13 shows the film thickness at the center as a function of time for oil drops with different viscosity interacting with the mica surface at various approach velocities in various solutions. It is worth noting that the definition of the dimple follows the method in section 1. It shows that the dimple height decreases with the increasing oil viscosity for both conditions.

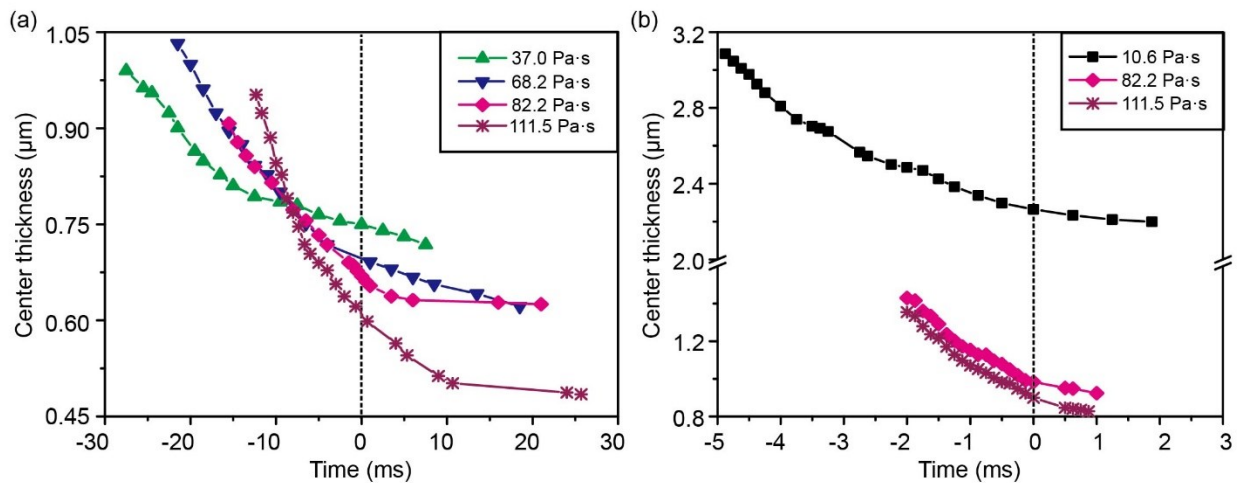


Figure A13 Film thickness at the center $h(0,t)$ as a function of time of oil drops with different viscosity for: (a) $V = 0.1$ mm/s in 0.1 mM SDS solution; (b) $V = 1.06$ mm/s in 1 mM SDS solution.

Film drainage process of selected conditions

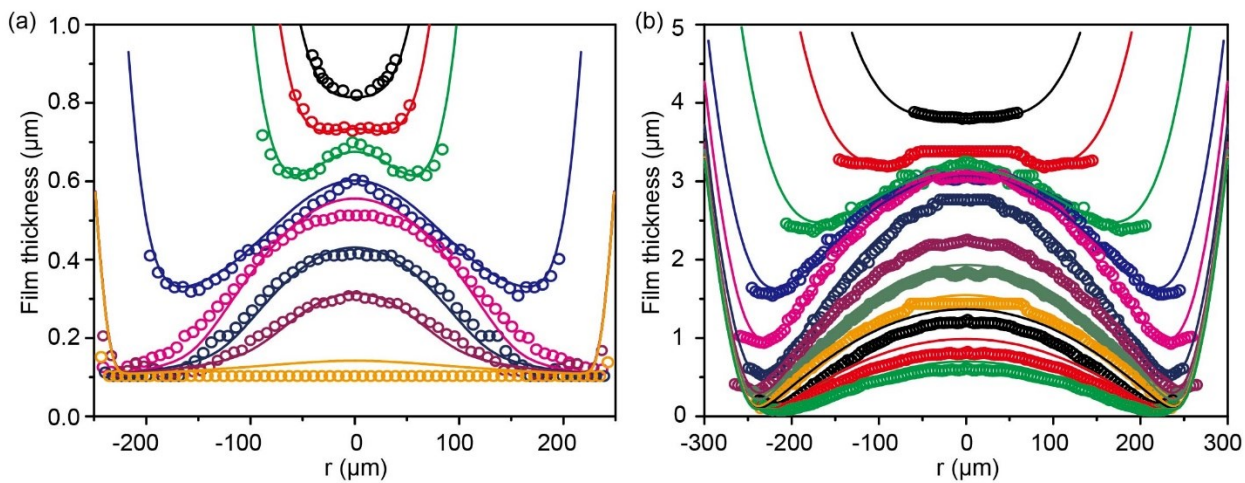


Figure A14 Comparison between theoretical (lines) and experimental (dots) film drainage process between oil with a viscosity of 0.001 Pa·s and a mica surface in: (a) $V = 0.1$ mm/s in 0.1 mM SDS solution. The measured time of profiles from top to bottom is -0.025 , 0.025 , 0.125 , 0.225 , 0.325 , 0.425 , and 0.525 ms.

1.025, 46.692, 88.275, 124.809, and 171.042 s. (b) $V = 1.06$ mm/s in 1 mM SDS solution. The measured time of profiles from top to bottom is -0.035 , -0.001 , 0.066 , 0.182 , 0.466 , 1.866 , 7.316 , 15.826 , 45.332 , 81.649 , 266.349 , and 581.649 s.

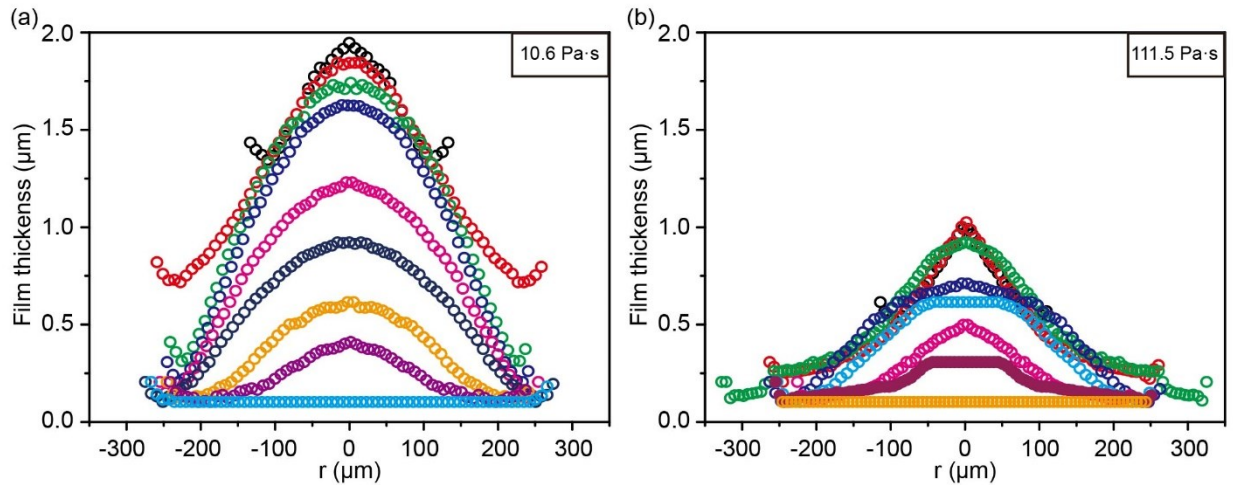


Figure A15 Film drainage process between oil drops with different viscosity and a solid surface in 0.1 mM SDS solution at $V = 1.06$ mm/s. (a) $\mu_o = 10.6$ Pa · s. The measured time of the profiles from top to bottom is: 0.020, 0.136, 1.420, 6.253, 33.836, 81.753, 161.536, 242.720, and 321.453 s. (b) $\mu_o = 111.5$ Pa · s. The measured time of the profiles from top to bottom is: 0.019, 0.069, 0.352, 2.102, 13.852, 81.769, 126.119, 177.802, and 235.469 s.

Properties of oils used in the manuscript

The refractive index and interfacial tension of different types of oil are given in Table A5. The refractive index of the silicone oil was taken from the supplier's data sheet (Sigma Aldrich). The oil/water interfacial tension was measured using the pendant drop method at room temperature (22.5 °C) and lasted for 30 min with a Theta Optical Tensiometer T200 (Biolin Scientific, Stockholm, Sweden)

Table A5 Physical properties of different oils.

		Interfacial tension (mN/m)			
Oil Type	Refractive index	0.1 mM SDS		1 mM SDS	
		Measured/Literature	Theoretical	Measured/Literature	Theoretical
Dodecane	1.421	42	42	22	22
		Measured		Measured	
		35 (0.01 Pa·s)		25 (0.01 Pa·s)	
Silicone oil	1.403	35.1 (12.5 Pa·s)	35	30	25
		34.4 (1 Pa·s) ¹		(0.001-0.005 Pa·s) ²	
		38 (0.001-0.005 Pa·s) ²		25 (1 Pa·s) ³	

Derivation of the modified SRYL model

Stokes-Reynolds-Young-Laplace (SRYL) model

The film drainage process can be characterised by the film Reynolds number $Re_f = \rho h_f V_f / \mu_w$ with $h_f \ll R$ and $Re_f \ll 1$. Lubrication theory can be applied to describe the evolution of the water film thickness $h(r,t)$ trapped between the oil drops and the solid surface.

$$\frac{\partial h}{\partial t} = \frac{m}{12\mu r} \frac{\partial}{\partial r} \left(r h^3 \frac{\partial p}{\partial r} \right) \quad (A6)$$

Because the viscosity of the oil drop is very large and the water environment contains certain amount of surfactant, the immobile oil/water and solid/water boundary was applied in this study, by using the parameter $m = 1$ in Eq. (A6).^{7,8}

The curvature of the oil drop can be described by the augmented Young-Laplace equation:

$$\gamma \left(\frac{1}{R_1} + \frac{1}{R_2} \right) = \frac{\gamma}{r} \frac{\partial}{\partial r} \left(r \frac{\partial h}{\partial r} \right) = p_{in} - p_{out} \quad (A7)$$

We apply the normal stress balance at the bottom of the drop when the drop interacts with the solid surface. The pressure inside the drop is defined as p_{oil} . The pressure in the bulk solution is set as the reference with $p_{\infty} = 0$. The pressure inside the water film has contributions from the hydrodynamic pressure p_f and the disjoining pressure $\Pi(h)$. Thus, Eq. (A7) can be expressed as:

$$\frac{\gamma}{r} \frac{\partial}{\partial r} \left(r \frac{\partial h}{\partial r} \right) = p_{oil} - p_f - \Pi(h) \quad (A8)$$

In our system, according to the DLVO theory, the disjoining pressure is comprised of van der Waals interaction Π_{vdW} and electrical double-layer interaction Π_{EDL} :

$$\Pi_{vdW}(h) = -\frac{A}{6\pi h^3} \quad (A9)$$

$$\Pi_{EDL}(h) = 64nkT \tanh\left(\frac{ze\varphi_s}{4kT}\right) \tanh\left(\frac{ze\varphi_o}{4kT}\right) \exp(-\kappa h) \quad (A10)$$

Here, the Hamaker constant A is 0.97×10^{-20} J according to the literature,⁹ k is the Boltzmann constant and T is the absolute temperature. φ_s and φ_o are the Stern potentials of oil/water and solid/water interface, respectively. The Stern potentials of oil/water and solid/water interface are taken from the literature¹⁰⁻¹² as -80 mV and -70 mV, respectively.

Initial and boundary conditions

The system of equations can be solved numerically with suitable initial and boundary conditions. The initial condition needs to be consistent with negligible pressure when the drop and surface are far apart. The initial condition is given as $h(0, r) = H_0 + \frac{r^2}{2R}$, where H_0 is the initial separation between drop and surface at the axis of symmetry.

The boundary conditions assume symmetry at the center, that means $\frac{\partial p}{\partial r} = \frac{\partial h}{\partial r} = 0$ at $r = 0$. At some distance $r = r_{max}$, where r_{max} is the boundary of the computational domain outside of the film region, we assume the pressure becomes negligibly small, that means $p \sim 0$. We also need a boundary condition that drives the system, which is given by $\frac{dh}{dt} = -V$ at $r = r_{max}$.

Model for high viscosity drop

During interaction of the high viscosity oil drop with the solid surface, the order of magnitude of the oil velocity inside the drop is $\sim 10^{-5}$ to 10^{-2} m/s. The Reynolds number inside the oil drop is within the range of 10^{-6} to 10^{-1} . The viscosity of the oil drop was ranged from 0.1 Pa·s to 100 Pa·s in our experiments. The flow inside the oil drop can be described by the Stokes equation.

$$\nabla p = \mu_o \nabla^2 \vec{u} \quad (A11)$$

Considering the pressure on the z -direction and the flow in the z, r -direction, Eq. (A11) becomes:

$$\frac{\partial p}{\partial z} = \mu_o \left(\frac{1}{r} \frac{\partial}{\partial r} \left(r \frac{\partial v}{\partial r} \right) + \frac{\partial^2 v}{\partial z^2} \right) \quad (A12)$$

Inside the oil drop, we apply the following scaling: $v \sim V$, $z, r \sim R$ so that the viscous normal stress can be expressed as:

$$\tau_v \simeq \frac{2\mu_o V}{R} \quad (A13)$$

By approximating the normal stress inside the drop with the contribution from both viscosity and surface tension, that gives:

$$p_{oil} \simeq 2 \left(\frac{\gamma}{R} + \frac{2\mu_o V}{R} \right) \quad (A14)$$

Modified SRYL model

Considering the contribution from viscosity to the pressure inside the oil drop and surface tension, we have the modified Young-Laplace equation:

$$\frac{(\gamma + 2\mu_o V)}{r} \frac{\partial}{\partial r} \left(r \frac{\partial h}{\partial r} \right) = \frac{2\gamma}{R} + \frac{4\mu_o V}{R} - p - \Pi(h) \quad (A15)$$

The $\gamma_e = \gamma + 2\mu_o V$ can be defined as the effective oil/water interfacial tension.¹³

Nondimensional modified Young-Laplace Eq. (A15) and drainage Eq. (A6) to achieve:

Scaled Stokes-Reynolds equation:

$$\frac{\partial h'}{\partial t'} = \frac{1}{12r'} \frac{\partial}{\partial r'} \left(r' (h')^3 \frac{\partial p'}{\partial r'} \right) \quad (A16)$$

Scaled Young-Laplace equation:

$$\frac{1}{r'} \frac{\partial}{\partial r'} \left(r' \frac{\partial h'}{\partial r'} \right) = 2 - p' - \Pi'(h) \quad (A17)$$

with scaling parameters:

$$h \sim h_0 h'$$

$$r \sim r_0 r'$$

$$p \sim p_0 p'$$

$$t \sim t_0 t'$$

Eq. (A16) and (A17) are the universal governing equations for drop-solid interactions.

Characteristic scales

Eliminating the variables h , r , p and t in the drainage and modified Young-Laplace equation with scaled characters h_0 , r_0 , p_0 and t_0 , we have:

Drainage equation:

$$\frac{h_0}{t_0} \frac{\partial h'}{\partial t'} = \frac{h_0^3 p_0}{\mu_w r_0^2} \frac{1}{12 r'} \frac{\partial}{\partial r'} \left(r' (h')^3 \frac{\partial p'}{\partial r'} \right) \quad (\text{A18})$$

Modified Young-Laplace equation:

$$\frac{(\gamma + 2\mu_o V) h_0}{r_0^2} \frac{1}{r'} \frac{\partial}{\partial r'} \left(r' \frac{\partial h'}{\partial r'} \right) = -p_0 (p' + \Pi') + \frac{2\gamma}{R} + \frac{4\mu_o V}{R} \quad (\text{A19})$$

In order to have nondimensionalized equations, all the physical parameters inside Eqs. (A18) and (A19) can be eliminated. Therefore, we have:

$$\frac{h_0^3 p_0}{\mu_w r_0^2 V} = 1 \quad (\text{A20})$$

with the boundary condition far away from the film $\frac{dh}{dt} = \frac{h_0}{t_0} \frac{\partial h'}{\partial t'} = V$

$$\frac{(\gamma + 2\mu_o V) h_0}{r_0^2 \left(\frac{\gamma}{R} + \frac{2\mu_o V}{R} \right)} = 1 \quad (\text{A21})$$

$$p_0 = \frac{\gamma}{R} + \frac{2\mu_o V}{R} \quad (\text{A22})$$

Rearranging Eqs. (A21) and (A22) by defining the capillary number inside the oil drop $Ca_d = \frac{\mu_o V}{\gamma}$,

we have:

$$r_0^2 = R h_0 \quad (\text{A23})$$

and

$$p_0 = \frac{\gamma}{R} (1 + 2Ca_d) \quad (A24)$$

Substituting Eq. (A23) and (A24) into Eq. (A20), we get the characteristic length scale:

$$h_0 = R \sqrt{\frac{Ca_f}{1 + 2Ca_d}} \quad (A25)$$

where $Ca_f = \frac{\mu_w V}{\gamma}$ is the capillary number of the water film. Similarly, we have:

$$r_0 = R \left(\frac{Ca_f}{1 + 2Ca_d} \right)^{\frac{1}{4}} \quad (A26)$$

and

$$t_0 = \frac{R}{V} \sqrt{\frac{Ca_f}{1 + 2Ca_d}} \quad (A27)$$

Scaling of h_d

Considering an oil drop with immobile boundary conditions, the height of the first occurrence of dimple h_d can be expressed as:

$$h_d = ch_0 \quad (A28)$$

For a capillary oil drop with the angle formed at the end of the capillary of around 140° , c was found to be around 0.5. Therefore, we have:

$$h_d = 0.5R \sqrt{\frac{Ca_f}{1 + 2Ca_d}} \quad (A29)$$

Comparison between theoretical and experimental film drainage process between high-viscosity oil and a mica surface

The current model (Eqs. (A8) and (A15)) by considering the viscous normal stress as $\tau_v = 2\mu_o V/R$ can capture the height of dimple occurrence very well. However, the film drainage process completely missed as the viscous normal stress disappears after the drop stops moving.

In order to capture the changing viscous normal stress over time, $\tau_v = 2\mu_o V_{center}/R$ is used instead in the Young-Laplace equation. V_{center} is the velocity at the center of the water film. It is at its maximum value at the approaching stage and decreased to almost zero after the drop stop moving, leading to a zero viscous normal stress. The comparison between theoretical and experimental film drainage process between silicone oil with viscosity of 37.0 Pa·s and 68.2 Pa·s and mica surface are shown in Figure A16a and b, respectively. This model could qualitatively predict most of the features of the film profile. It clearly shows that a pointy-shaped dimple was formed initially, followed by a film shape of a changing curvature and a pointy center formed after the drop stopped. Finally, the pointy center gradually disappeared, and the water drained out under the Laplace pressure. However, this model would predict a much higher height of dimple formation. This is because the pressure is added from the center of the drop to infinity instead of the interaction area. In spite of this, the model can still predict that the height of dimple formation decreases with the increasing oil viscosity. This version of the model cannot quantitatively provide a good agreement. This is because the viscous normal stress is still based on a scaling argument, how and when the viscous normal stress would disappear are not included at this stage. The model needs further refining to improve the comparison with experimental data. However, it clearly shows that the viscous normal stress would play a role initially and disappear after the drop stop moving.

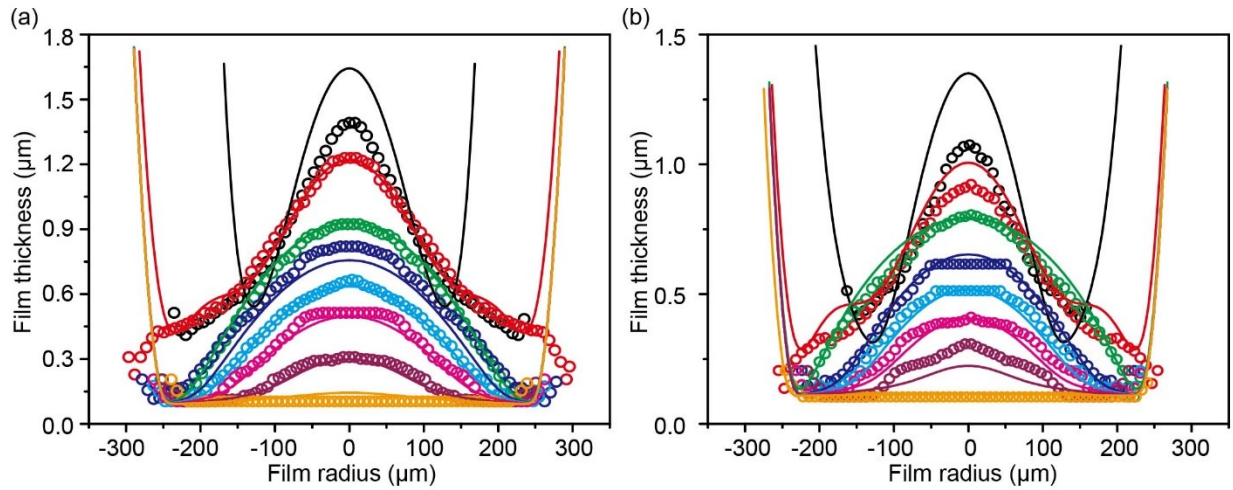


Figure A16 Comparison between theoretical (lines) and experimental (dots) film drainage process between oil with different viscosity in 0.1 mM SDS solution at $V = 1.06 \text{ mm/s}$. (a) $\mu_o = 37.0 \text{ Pa} \cdot \text{s}$. The measured time of the profiles from top to bottom is: 0.067, 0.618, 19.7, 97.1, 144.5, 211.0, 318.1, and 391.6 s. Drop stopped moving at 0.26 s. (b) $\mu_o = 68.2 \text{ Pa} \cdot \text{s}$. The measured time of the profiles from top to bottom is: 0.025, 0.743, 3.42, 62.69, 101.6, 137.0, 189.0, 243.9 s. Drop stopped moving at 0.072 s.

References

- (1) Scheludko, A.; Platikanov, D. Untersuchung dünner flüssiger Schichten auf Quecksilber. *Kolloid-Zeitschrift und Zeitschrift für Polymere*, **1961**, *175*, 150.
- (2) Parkinson, L.; Ralston, J. The interaction between a very small rising bubble and a hydrophilic titania surface. *The Journal of Physical Chemistry C* 2010, *114*, 2273_2281.
- (3) Zhang, X.; Tchoukov, P.; Manica, R.; Wang, L.; Liu, Q.; Xu, Z. Simultaneous measurement of dynamic force and spatial thin film thickness between deformable and solid surfaces by integrated thin liquid film force apparatus. *Soft Matter* 2016, *12*, 9105-9114.
- (4) Peters, F.; Arabali, D. Interfacial tension between oil and water measured with a modified contour method. *Colloids and Surfaces A: Physicochemical and Engineering Aspects* 2013, *426*, 1-5.
- (5) Kanellopoulos, A.; Owen, M. Adsorption of sodium dodecyl sulphate at the silicone fluid/water interface. *Transactions of the Faraday Society* 1971, *67*, 3127-3138.
- (6) White, A. R.; Ward, T. Surface remobilization of buoyancy-driven surfactant-laden drops at low reynolds and capillary numbers. *AIChE Journal* 2019, *65*, 294-304.
- (7) Yiantsios, S. G.; Davis, R. H. On the buoyancy-driven motion of a drop towards a rigid surface or a deformable interface. *Journal of Fluid Mechanics* 1990, *217*, 547-573.
- (8) Liu, B.; Manica, R.; Liu, Q.; Klaseboer, E.; Xu, Z.; Xie, G. Coalescence of bubbles with mobile interfaces in water. *Physical review letters* 2019, *122*, 194501.
- (9) Israelachvili, J. N. *Intermolecular and surface forces*; Academic press, 2011.
- (10) Nishimura, S.; Tateyama, H.; Tsunematsu, K.; Jinnai, K. Zeta potential measurement of muscovite mica basal plane-aqueous solution interface by means of plane interface technique. *Journal of colloid and interface science* 1992, *152*, 359-367.

- (11) Zaucha, M.; Adamczyk, Z.; Barbasz, J. Zeta potential of particle bilayers on mica: a streaming potential study. *Journal of colloid and interface science* 2011, 360, 195-203.
- (12) Djerdjev, A. M.; Beattie, J. K. Electroacoustic and ultrasonic attenuation measurements of droplet size and ξ -potential of alkane-in-water emulsions: effects of oil solubility and composition. *Physical Chemistry Chemical Physics* 2008, 10, 4843-4852.
- (13) Freer, E.; Wong, H.; Radke, C. Oscillating drop/bubble tensiometry: effect of viscous forces on the measurement of interfacial tension. *Journal of colloid and interface science* 2005, 282, 128-132.

Appendix D

Film drainage process of bitumen at high temperature at $V=0.1$ mm/s

Figure A17 shows the film drainage process between bitumen and a hydrophobic silica wafer at 40 and 45 °C when the approach velocity was 0.1 mm/s. It is worth noting that only the initial stage of the film drainage process was recorded and non-attachment happened within the experimental shooting time (1 min). The height of the dimple formation was measured to be 573 ± 40 nm and 773 ± 39 nm for temperature of 40 and 45 °C, respectively.

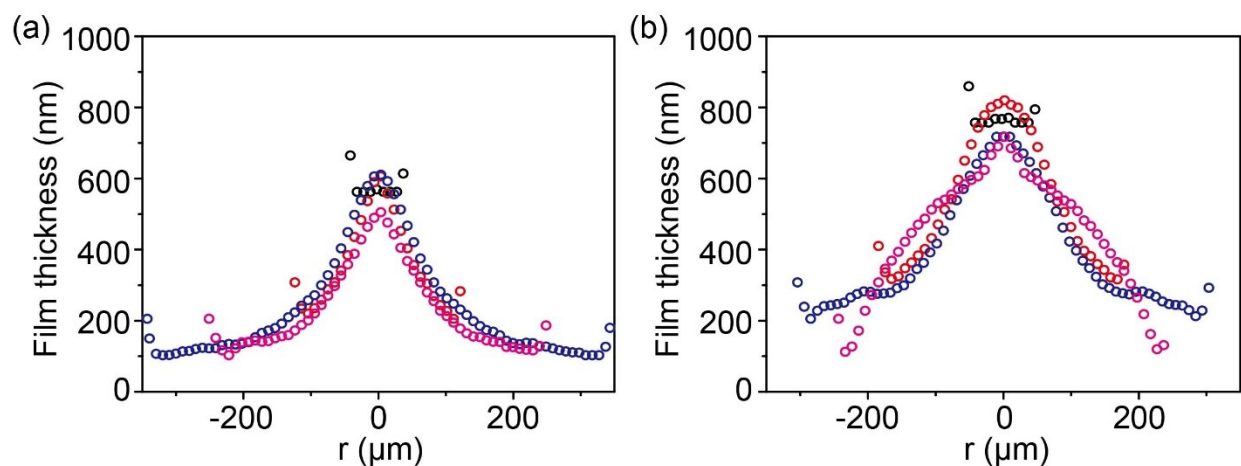


Figure A17 Film drainage process between bitumen drop at high temperature and a hydrophobic silica wafer in 10 mM NaCl solution at $V = 0.1$ mm/s. (a) 40 °C. The measured time from top to bottom are: 0, 0.352, 2.44, 14.408 s. (b) 45 °C. The measured time from top to bottom are: 0, 0.28, 1.28, 12.664 s.